UNIVERSITEIT VAN PRETORIA
UNIVERSITY OF PRETORIA
YUNIBESITHI YA PRETORIA

Nested Climate Modelling over Southern Africa with a Semi-Lagrangian Limited Area Model

by

Francois Alwyn Engelbrecht

Submitted in partial fulfilment of the requirements

for the degree of

MASTER OF SCIENCE

in the

Faculty of Natural and Agricultural Sciences

University of Pretoria

October 2000

© University of Pretoria

UNIVERSITEIT VAN PRETORIA
UNIVERSITY OF PRETORIA
YUNIBESITHI YA PRETORIA

Nested Climate Modelling over Southern Africa with a Semi-Lagrangian Limited Area Model

Francois Alwyn Engelbrecht

Promoter:	Dr. CJ deW Rautenbach
Department:	Department of Earth Sciences
Faculty:	Faculty of Natural and Agricultural Sciences
University:	University of Pretoria
Degree:	Master of Science

Summary

Atmospheric general circulation model (AGCM) simulations of southern African climate on a regional scale are unsatisfactory. The main reason for this result is that computational requirements determine that AGCMs are run at coarse horizontal resolutions. The impact of local forcing such as complex topography, and important small-scale circulation systems cannot be resolved properly at typical AGCM resolutions. However, mesoscale forcing and circulation systems have an important modifying influence on the southern African climate. The technique of nested climate modelling can be used to obtain detailed climate simulations over limited areas of the earth. Nested climate modelling involves the nesting of a high grid-resolution limited-area model (LAM) within an AGCM (or observational analyses) over an area of interest. The AGCM provides the LAM with boundary conditions during an extended integration period. With a grid resolution of 10-100 km, the LAM model is able to simulate some of the mesoscale features of the circulation.

The limited-area model DARLAM has been developed to meet the requirements of both climate simulation experiments and shorter-term mesoscale studies. The dynamical formulation of DARLAM is characterised by the semi-Lagrangian method used to simulate advection. The essential feature of the scheme is that the total or material derivatives in the equations of motion are treated directly by calculating the departure points of fluid parcels. The semi-Lagrangian approach allows the use of large time steps during the model integration. Numerical experiments performed in the study indicate that the particular semi-Lagrangian method used in DARLAM is highly accurate and has excellent conservation and stability properties.

The results of climate simulations over the SADC region with DARLAM are described. The model is one-way nested within simulations of selected months from a long seasonal varying simulation of the CSIRO9 AGCM. The relatively coarse resolution AGCM is used to provide boundary conditions to DARLAM, which is run at a horizontal grid resolution of 60 km with 18 levels in the vertical. The higher resolution adds significant smaller-scale detail to the coarser simulation of the AGCM. The additional detail provides improved simulation results, when compared to AGCM results over most regions of the LAM domain.

Genestelde Klimaatmodellering oor Suidelike Afrika met 'n Semi-Lagrange Beperkte-Area-Model

Francois Alwyn Engelbrecht

Promotor:	Dr. CJ deW Rautenbach
Departement:	Department Aardwetenskappe
Fakulteit:	Fakulteit Natuur- en Landbouwetenskappe
Universiteit:	Universiteit van Pretoria
Graad:	Meester in die Wetenskap

Samevatting

Atmosferiese algemene sirkulasie model (AASM) simulasies van suider Afrikaanse klimaat op streekskaal is onbevredigend. Die hoofrede hiervoor is dat berekeningsvereistes bepaal dat AASMe geloop word met ruwe horisontale resolusie. Die impak van lokale forsering soos komplekse topografie en kleinskaalse sirkulasiesisteme kan nie vasgevang word met tipiese AASM-resolusie nie. Mesoskaalforsering- en sirkulasiesisteme het egter `n belangrike modifiserende invloed op suider Afrikaanse klimaat. Die tegniek van genestelde klimaatmodellering kan gebruik word om gedetaileerde klimaatsimulasies oor beperkte dele van die aarde te verkry. Die tegniek behels die nes van `n hoë roosterresolusie beperkte- area-model (BAM) binne `n AASM (of waargenome data) oor die area wat van belang is. Die AASM verskaf die BAM met randwaardes gedurende `n verlengde integrasie periode. Met `n roosterresolusie van 10-100 km is kan die BAM sommige mesoskaaleienskappe van die sirkulasie simuleer.

Die beperkte-area-model DARLAM is ontwikkel om te voldoen aan die vereistes van sowel klimaatsimulasie-eksperimente en korter tydskaal mesoskaalstudies. Kenmerkend van die modelformulasie is die semi-Lagrange metode wat gebruik word vir adveksie-simulasie. Die essensiële kenmerk van die skema is dat die totale afgeleides in die bewegings-vergelykings direk hanteer word deurdat vertrekpunte van vloeistofdeeltjies bereken word. Die semi-Lagrange benadering bied die gebruik van groot tydstappe gedurende die modelintegrasie. Numeriese eksperimente uitgevoer dui aan dat die semi-Lagrange metode wat in DARLAM gebruik word hoogs akkuraat is en uitstekende behouds- en stabiliteitseienskappe besit.

Die resultate van klimaatsimulasies oor die SADC gebied met DARLAM word beskryf. Die model is een-rigting genestel binne simulasies van uitgesoektee maande van `n lang, seisonaal variërende simulasie van die CSIRO9 AASM. Die relatief lae resolusie AASM is gebruik om randwaardes aan DARLAM te verskaf, wat geloop is met `n horisontale roosterresolusie van 60 km met 18 vlakke in die vertikaal. Die hoër resolusie voeg betekenisvolle kleiner skaal detail by die ruwer simulasie van die AASM. Die bykomende besonderhede verskaf verbeterde simulasie resultate in vergelyking met die AASM oor die meeste areas binne die BAM gebied.

ACKNOWLEDGEMENTS

The author wishes to express his appreciation to the following persons and organisations for their assistance and contribution to make this dissertation possible:

- *Dr. CJ deW Rautenbach* (Head, Meteorology, UP). I am extremely grateful to Dr. Rautenbach for his inspiration of my interests in numerical modelling, and for all his advice and support during the course of this study.

- *Dr. JL McGregor* (Specialist Scientist) from the CSIRO (Atmospheric Research), Australia, for his supervision while I was visiting the CSIRO, as well as his continuous guidance during the course of the study.

- *Dr. JJ Katzfey* (Specialist Scientist) from the CSIRO (Atmospheric Research), Australia, for his supervision while I was visiting the CSIRO, but especially for his guidance afterwards via the Internet, during the implementation of DARLAM on a local computer.

- *Dr. G Green* (Director, Water Research Commission) for all his encouragement.

- *Prof G Djolov* (Dean of Science, University of Venda) and *Mr R Sewel* (SAWB) for encouraging my interest in the advection problem.

- The *Commonwealth Scientific and Industrial Research Organisation (CSIRO)* in Australia for inviting me to attend a workshop on regional climate modelling held in Melbourne in January 2000.

- The *Water Research Commission* for financially supporting the research, by means of a post-graduate study bursary awarded to me.

- Dr. S Wilson and his wife Denise for providing me with accommodation during my visit to the CSIRO in Melbourne.

- My dear friends in the Forecasting Office of the SAWB. Most of the research was performed on a part-time basis while I was working as an operational weather forecaster in the Central Forecasting Office of the SAWB. I would like to thank Evert, Philip, Michael, Steve, Kevin, Chris, DeBroy, Stephan, Jannie, Bheki, Christien, Elizma, Melton, Esther, Roland, Henning, Dan and Solly for all their support during this exciting period in my life.

- The friendly librarians of the SAWB, Karin and Elda, for helping me to find the hundreds of references listed at the end of this thesis.

- My parents and sister for all their support and encouragement during the course of the study.

- Most of all, I thank the Lord for giving me the strength to undertake this study, and for the privilege of being able to study the atmosphere.

TABLE OF CONTENTS

CHAPTER 1 Introduction

CHAPTER 2 Perspective for nested climate modelling over southern Africa

CHAPTER 3 **Simulating climate with the limited area model DARLAM**

CHAPTER 4 **The multiply-upstream semi-Lagrangian method of simulating advection**

CHAPTER 5 January and July climate simulations over southern Africa using DARLAM

LIST OF SYMBOLS

$\frac{d}{dt}$: Time derivative that follows the motion of a parcel
k : Wave number in the x direction (m^{-1})
l : Wave number in the y direction (m^{-1})
n : number of time steps
u : Velocity component in the x direction (ms^{-1})
v : Velocity component in the y direction (ms^{-1})
t : Time (s)
L_x : Wave length in the x direction (m)
L_y : Wave length in the y direction (m)
R : Relative phase change in time of the numerical solution
$\overline{v}$: Velocity ($ms^{-1)}$
$\hat{v}$: Approximated velocity (ms^{-1})
(x_*, y_*): Departure point of a particle
$\overline{\nabla}$: Spatial gradient operator
ψ : Dependent variable in the advection equation (scalar quantity)
α : Non dimensional advection velocity
α_1 : Non dimensional advection velocity component in the x direction
α_2 : Non dimensional advection velocity component in the y direction
ϕ : Stream function
λ : Amplification factor
λ_{re} : Real component of the amplification factor
λ_{im} : Imaginary component of the amplification factor
θ : Phase change in time of the numerical solution
ω : Phase change in time of the true solution
Λ : x or y amplification factor
Δx : Spatial increment in the x direction (m)
Δt : Time interval (s)
Δy : Spatial increment in the y direction (m)
Ψ : Wave amplitude of scalar quantity
Ω : Angular velocity ($rads^{-1}$)

LIST OF FIGURES

LIST OF TABLES

LIST OF ABBREVIATIONS

AGCM	Atmospheric general circulation model
BMRC	Bureau of Meteorology Research Centre
CFL	Courant-Friedrichs-Lewy
CSIRO	Commonwealth Scientific and Industrial Research Organisation
DARLAM	Division of Atmospheric Research Limited Area Model
ECMWF	European Centre for Medium-range Weather Forecasting
GFDL	Geophysical Fluid Dynamics Laboratory
LAM	Limited-area model
LBC	Lateral boundary conditions
NCAR	National Centre for Atmospheric Research
NCEP	National Centre for Environmental Prediction
NCM	Nested climate model
RCM	Regional climate model
R21	Rhomboidal truncation at wave number 21
SADC	Southern African Developing Countries
SAWB	South African Weather Bureau
SST	Sea surface temperature
T63	Triangular truncation at wave number 63
UP	University of Pretoria

CHAPTER 1

INTRODUCTION

1.1 BACKGROUND

Enhanced levels of greenhouse gasses of direct or indirect anthropogenic origin might substantially change the climate of planet Earth. Changes in global climate have the potential to severely affect the climate of different regions of the world. Shifting climatic zones, higher sea levels and more frequent storms, droughts, floods and heat waves could generate a range of social, economical and political disruptions (Rowlands, 1998). Understandably, there is an increasing demand by the scientific community, policy makers, and the public for realistic future scenarios of the possible impact of climate change. There is also a need to understand the complex behaviour of the present climate and general circulation of the atmosphere. Shorter-term climate variability, such as the occurrence of floods and droughts, might severely affect the environment. These aspects have rendered the issue of regional climate simulation critically important.

Atmospheric general circulation models (AGCMs) are the primary tools available for climate simulation. Current AGCMs have reached a high level of sophistication, and provide a full three-dimensional representation of the atmosphere. Mathematical equations for the conservation of momentum, mass and energy are numerically solved in these models. Also included are parameterisation schemes for the main physical atmospheric processes such as radiative transfer, cloud formation with precipitation, boundary layer and surface physics. On different levels in the vertical AGCMs are integrated forward in time over the entire globe and are often coupled with other models resembling the earth-atmosphere system to form coupled atmosphere-ocean-sea-ice-snow-cover models.

Coupled models are essential to generate relatively stable projections of paleo, present or future global climate. Here, a model needs to run for long simulation periods to allow for the various components in the atmospheric system to reach equilibrium. Limitations of present day computer resources are of such a nature that a relatively coarse horizontal resolution is used in AGCM runs (nothing finer than 1° longitude and latitude). Another limitation in high-resolution AGCM development is that the physical parameterisation schemes used in the models have specifically been developed and tuned for coarser horizontal resolutions. These schemes may not be suitable for higher resolution models.

Despite the limitations on resolution, AGCM simulations adequately capture the main features of the atmospheric general circulation since large scale forcing such as the Earth's orbital characteristics, radiation budget and global greenhouse gas abundance are included in the code formulation. Large scale forcing modulates the succession of weather events that characterise the climate regime of a given area. Capturing of the large-scale forcing by an AGCM will therefore ensure that the climate is adequately simulated.

However, important smaller-scale (also known as regional or mesoscale) meteorological forcing and circulation systems are not resolved (or adequately parameterised) at typical AGCM resolutions. Mesoscale forcing, such as those induced by complex topographical features and surface characteristics, may modify the structure of weather events. This often initiates additional mesoscale circulation systems that are not detected in larger-scale AGCM results. Embedded in the large-scale atmospheric systems, these smaller circulation systems contribute to regulate the regional (local) distribution of atmospheric variables within a given region.

The main challenge in regional climate modelling is to include forcing on the mesoscale and to capture the associated mesoscale circulation systems and their modifying effect on the regional atmospheric circulation. There are three main approaches to the simulation of regional climate change (Giorgi and Mearns, 1991):

1) *Purely empirical approaches* in which forcing is not explicitly accounted for, but regional climate scenarios are constructed from instrumental data records or paleoclimatic analogues.

2) *Semi-empirical approaches* in which AGCMs are used to describe the atmospheric response to large-scale forcing of relevance to climate change, but empirical techniques account for the impact of mesoscale forcing.

3) *Modelling approaches* in which mesoscale forcing is described by increasing model resolution only over areas of interest.

Their own empiricism and the availability of data sets of adequate quality, limit the empirical and semi-empirical approaches. During the last decade a nested limited-area model (LAM)–AGCM methodology for regional atmospheric simulation has become popular. The technique is physically rather than empirically based and has a wide range of applications.

More recently, a variable resolution (stretched grid) AGCM methodology for regional climate simulation has been developed, with encouraging preliminary results. In this study, however, the focus will be on the nested LAM-AGCM methodology.

1.2 NESTED CLIMATE MODELLING

Detailed climate simulations for restricted areas of the globe by a high-resolution LAM provide a computationally feasible alternative to relatively course resolution AGCM simulations. Here the LAM (a primitive equation model) is nested within a global AGCM, or within a global observational analysis. This implies that the AGCM (or observed analysis) provides the LAM with information at the lateral boundaries of its domain during the integration. Therefore, nested climate modelling is in essence a boundary value problem. LAMs operating in this framework are known as nested climate models (NCMs) or regional climate models (RCMs).

AGCM simulations should produce realistic intensities and frequencies of the major synoptic systems during a climate simulation. The LAM, with a horizontal grid resolution finer than 100 km (100 km x 100 km), may capture some of the mesoscale forcing and circulation features. Generally it is found that the higher grid resolution of the nested simulations results in a more accurate, detailed and realistic depiction of the climate over a selected region. Nested climate modelling is becoming increasingly popular to produce more detailed atmospheric circulation patterns for selected regions.

1.3 REGIONAL CLIMATE MODELLING AT THE CSIRO

For some years the CSIRO (Commonwealth Scientific and Industrial Research Organisation) in Australia has been involved in an active programme aiming to simulate regional climate using the Division of Atmospheric Research Limited Area Model (DARLAM). DARLAM has been nested within the coarser resolution CSIRO9 (9 levels in the vertical) R21 (rhomboidal truncation at wave number 21) spectral AGCM, or alternatively, within observational analysis. DARLAM is a two-time-level, semi-Lagrangian LAM with physics similar to that of the AGCM (McGregor et al., 1993a; McGregor, 1997a). Generally the higher horizontal resolution of the DARLAM simulations provides significantly improved climate simulations (compared to the AGCM) near distinctive topographical features, in particular for precipitation and near-surface atmospheric variables.

The earliest DARLAM simulations were performed with perpetual January conditions. Subsequently, multiple January and July simulations have been performed followed by full seasonal cycle simulations up to 20 years in duration. During these simulations DARLAM was nested in the CSIRO slab-ocean (fixed observed ocean climatology as lower boundary input) AGCM. Most of the simulations over Australia with both 1 x CO_2 and 2 x CO_2 conditions have been performed at a grid resolution of 125 km. In addition, selected doubly-nested simulations have been performed at 50 km and 60 km grid resolutions.

Previously DARLAM has successfully been applied over New Zealand and South Africa. Output results compared well with the associated observed patterns. However, an important aspect that still needs to be improved is the fact that DARLAM tends to simulate excessive precipitation over regions with steep terrain.

New developments at the CSIRO involve the use of variable resolution AGCMs in order to simulate regional climate. For this purpose a new two-time-level AGCM has been designed on a conformal-cubic grid (Rancic et al., 1996). The model utilises a semi-Lagrangian advection scheme. A major advantage of this approach is that the model can be used in stand-alone mode without the limitations imposed by a nesting procedure. Encouraging preliminary results have been obtained.

1.4 ATMOSPHERIC MODELLING AT UP

Atmospheric modelling at the University of Pretoria (UP) was initiated in the early 1990's when the CSIRO4 (4-levels in the vertical) AGCM was obtained through a licence agreement between the University of Pretoria and the CSIRO. The model was installed on a local super computer (CONVEX C-120). A number of model simulations were performed, which included a 20-year control run, as well as selected experiments outlining the interaction between the ocean surface and atmosphere over the Indian and Pacific Oceans (Van Heerden et al., 1995).

In 1995, with the assistance of CSIRO researchers, Dr. CJdeW Rautenbach (staff member in Meteorology at UP) installed the CSIRO9 Mark II AGCM with R21 spectral resolution on a CRAY-EL94 super computer located at the South African Weather Bureau (SAWB). A number of unpublished experiments were performed in order to investigate global ocean-atmosphere interaction. The model's ability to simulate present day climate over southern Africa was also emphasised (Rautenbach and Engelbrecht, 2001). During the last three years the AGCM became a useful tool to produce experimental seasonal forecasts of rainfall over the southern African region. In his PhD-thesis Dr. Rautenbach, with the assistance of Dr. HB Gordon from the CSIRO, introduced a hybrid (sigma/pressure) vertical co-ordinate to the dynamics of the CSIRO9 Mark II AGCM (Rautenbach, 1999). In this study it was indicated that the hybrid vertical co-ordinate system contributes to improved climate simulations in the upper levels of the atmosphere.

During 1997 Dr. Rautenbach and CSIRO researchers installed the CSIRO9 (Mark II) AGCM with a T63 (triangular truncation at wave number 63) spectral resolution on the CRAY-EL94 super computer located at the SAWB. The model has been used in a study to investigate the influence of extra-tropical Sea Surface Temperature (SST) fluctuations on the rainfall over South Africa (Rautenbach, 1998; Engelbrecht and Rautenbach, 2001).

Regional climate modelling has numerous applications in the southern African region (Engelbrecht and Rautenbach, 2000). Seen against this background an agreement was reached in 1999 between UP and the CSIRO to install DARLAM on a suitable computer at UP. With this prospect in mind the author visited the CSIRO (Atmospheric Research) during January 2000. During the visit the flow structure of DARLAM was studied in detail. With hard work and additional assistance from CSIRO scientists (Drs. JL McGregor and JJ Katzfey) via the Internet, DARLAM was eventually installed on a powerful workstation at UP. The first LAM simulations locally performed with DARLAM are described in Chapter 5.

1.5 OBJECTIVES OF THE RESEARCH

The research detailed in this thesis has three main objectives:

1.5.1 *To investigate the potential applications and theoretical limitations of the nested climate modelling methodology in the southern African region.*

This was attained through a thorough literature study of the nested climate modelling approach as well as the theoretical aspects of the technique. The investigation focused on how the unique land/sea/atmosphere features of southern Africa might influence the applicability of various theoretical aspects to the region.

1.5.2 *To study the structure and formulation of DARLAM, in particular the semi-Lagrangian scheme utilised to simulate advection.*

The properties of the semi-Lagrangian scheme used in DARLAM were analysed according to the work of Dr. JL McGregor who first proposed the scheme. Numerical approximations by the semi-Lagrangian scheme to the solution of the linear advection equation are examined and compared to approximations by well-known finite difference schemes. Numerical experiments were performed to investigate the properties of the semi-Lagrangian scheme in non-linear velocity fields.

1.5.3 *To implement DARLAM over an extended southern African domain, and to perform and verify preliminary atmospheric simulations over the region.*

In order to do this it was essential to become familiar with the flow structure and code of DARLAM. The interpolation algorithms, required to provide the nested model with initial and boundary conditions as supplied by the CSIRO9 (Mark II) AGCM, were obtained and studied. The DARLAM code was successfully installed on a powerful workstation with a Linux operating system. Multiple January and July atmospheric simulations, nested within a long seasonal cycle simulation with the AGCM, were performed over an extended southern African domain. The entire Southern African Developing Countries (SADC) region has been included in the domain. This achievement opens doors for further collaboration with our neighbouring countries.

1.6 ORGANISATION OF THE REPORT

In Chapter 2 the modifying effect of mesoscale forcing on the climate of southern Africa is discussed and the need for high-resolution climate simulations over the region is highlighted. The concept of nested climate modelling is defined and the philosophy behind the methodology is explained. This is followed by a detailed discussion of the theoretical aspects of nested climate modelling such as nesting strategies, domain size and lateral boundaries, model resolution, spin-up time and initialisation. Emphasis is placed upon the applicability of each aspect in the southern African region. The chapter concludes with a discussion of some of the unresolved theoretical issues in the field of nested climate modelling. Perspective is provided concerning the potential applications and theoretical limitations of the nested climate modelling methodology over southern Africa.

The nested model DARLAM is the only state of the art LAM developed in the Southern Hemisphere. Chapter 3 provides a general discussion of the most important features of DARLAM. The chapter includes a discussion of the strategy adopted to nest DARLAM within the CSIRO9 (Mark II) AGCM. The formulation of the AGCM itself is described briefly, followed by a description of the surface characteristics, dynamical formulation and parameterisation schemes of DARLAM. Previous experiments conducted with DARLAM over Australia, New Zealand and Asia are examined. Two experiments performed at a relatively coarse resolution over southern Africa with an earlier version of DARLAM are put in the spotlight. Regional climate modelling groups world wide are experiencing difficulties with the simulation of rainfall in regions of steep topography. DARLAM is no exception and therefore Chapter 3 concludes with a discussion of the impact of topography on DARLAM simulations.

DARLAM makes use of a unique semi-Lagrangian advection scheme. Various forms of the advection equation, that describes transport by the wind of a dependant variable, are considered in Chapter 4. In general, it is regarded as impossible (or at least very cumbersome) to obtain the exact solution of the non-linear advection equation. For this reason, numerous numerical methods have been developed to approximate the true solution of the advection equation. This chapter is primarily concerned with the multiply-upstream semi-Lagrangian method of approximating the true solution of the advection equation. The semi-Lagrangian scheme used in DARLAM in particular is put under the magnifying glass. The scheme is compared to well-known finite difference schemes, namely the Leapfrog scheme and Lax-Wendroff schemes, in order to evaluate their relative merits with regard to stability and accuracy. The investigation commences with a comparison between the different numerical solutions of the linear advection equation to its exact solution (which is known). Von Neuman's method is used to determine the stability properties of the various schemes. This is followed by an examination of the ability of the various schemes to represent the phase properties of the exact solution. Two-dimensional numerical tests are performed to investigate the behaviour of the schemes in events where the velocity field is non-linear. These tests include Crowley's test for uniform solid body rotation as well as Smolarkiwiecz's test for strong deformational flow. It is shown that the semi-Lagrangian scheme used in DARLAM is superior to the finite difference schemes with respect to phase, stability and conservation properties.

January and July climate simulations over an extended southern African domain (complete SADC region) have been performed using DARLAM. The model was one-way nested within output fields for selected months from a long seasonal cycle simulation with the CSIRO9 Mark II AGCM. Nine separate simulations (ensemble members) have been generated for both January (austral summer) and July (austral winter). Results from these simulations constitute the model climatology for the two months. Chapter 5 commences with a discussion concerning the design of the nested climate modelling experiment over southern Africa. The selection of observational data fields used for qualitative model verification is motivated. The chapter concludes with a discussion of DARLAM output results (mean sea-level pressure, winds, temperature and rainfall). The results are compared to the associated AGCM simulations and to observations. It is indicated that the DARLAM results are significantly better than those obtained from the AGCM. This is particularly true for near-surface variables close to topographic features. It is also shown that DARLAM severely overestimates rainfall over South Africa, particularly over regions of steep topography.

Some conclusions are made in Chapter 6 with respect to the applicability of the nested climate modelling methodology over southern Africa. The advantages of using a semi-Lagrangian limited-area model are highlighted. Potential applications of DARLAM over southern Africa are outlined and a view of the future role of nested climate modelling over southern Africa is presented.

Appendix A contains the VISUAL BASIC code developed to perform Crowley's Cone test with the semi-Lagrangian D3 scheme. Output is in MATLAB format for displaying purposes.

Appendix B contains the FORTRAN code developed to perform Smolarkiewicz's test of strong deformational flow with the semi-Lagrangian D3 scheme. Results can be displayed using PGPLOT software.

CHAPTER 2

PERSPECTIVE FOR NESTED CLIMATE MODELLING OVER SOUTHERN AFRICA

2.1 INTRODUCTION

The challenge of simulating regional climate is in essence one of representation of climate forcing on two different spatial scales. These scales are the large-scale (defined as the range of approximately 1000 km to global) and the mesoscale (defined as the range of a few kilometres to several hundred kilometres) (Giorgi and Mearns, 1991). For example, large-scale forcing induced by the Earth's orbital characteristics, radiation budget and the abundance of greenhouse gasses, modulates the atmospheric general circulation. This in turn determines the succession of weather events that characterise the climate regime of a given area. Mesoscale forcing such as forcing induced by complex topographical features and surface characteristics modifies the structure of weather events and initiates mesoscale atmospheric circulation systems. Embedded in the large-scale atmospheric systems, the mesoscale circulation systems contribute to modulate the regional distribution of climate variables (Giorgi and Mearns, 1991).

AGCMs are the primary tools available for atmospheric simulation (climate and shorter-term variability). Current AGCMs have reached a high level of sophistication and provide a full three-dimensional representation of the atmosphere. These models intend to solve the equations for conservation of momentum, mass and energy and include parameterisation schemes for the main physical processes in the atmosphere such as radiative transfer, cloud formation and precipitation and boundary layer and surface physics. The applications of AGCMs over southern Africa include simulations of present day climate (Joubert, 1997; Rautenbach and Engelbrecht, 2001), simulations of climate variability (Joubert, 1997; Engelbrecht and Rautenbach, 2001) and experiments describing possible links between droughts/floods over the sub-continent and global sea surface temperature (SST) variations (Mason et al., 1994; Jury and Pathack, 1996).

Although AGCMs adequately reflect the main characteristics of the general circulation over southern Africa (Joubert, 1997; Rautenbach and Engelbrecht, 2001; Engelbrecht and Rautenbach, 2001), their performance in reproducing regional climate detail is rather poor (Joubert et al., 1999; Engelbrecht and Rautenbach, 2000). A major problem in AGCMs when trying to simulate the regional climate has to do with horizontal resolution. AGCMs used for simulating present climate conditions over southern Africa have been run at resolutions of approximately 2.5° for both latitude and longitude (Joubert, 1997; Rautenbach and Engelbrecht, 2000; Engelbrecht and Rautenbach, 2001). This relatively course resolution is a result of the computational requirements set by the global climate modelling system which rapidly become prohibitive as the resolution increases (MgGregor et al., 1993b; Giorgi and Mearns, 1991). At these resolutions the effect of large-scale forcing on the general atmospheric circulation can be successfully captured. The impact of local forcing, which acts on scales as small as a few kilometres and strongly influence the detailed distribution of atmospheric variables over many parts of southern Africa, is however lost. For example, the small-scale atmospheric circulation induced by detailed topography can not be presented at typical AGCM resolutions (McGregor, 1997a). In addition there are important small-scale meteorological phenomena such as tropical cyclones that are not adequately parameterised as sub-grid scale processes at typical AGCM resolutions. These phenomena are vital in their own right and also significantly affect the mean climatology of a specific region (McGregor et al., 1993b).

As a computationally feasible alternative, it is possible to produce detailed climate simulations for restricted areas on the globe by nesting a high-resolution LAM within a global AGCM, or within an observational analysis. Such nested models (which are primitive equation models) are also known as RCMs, although the term could also encompass variable resolution global AGCMs (McGregor, 1997a). A selected domain is modelled in a stand-alone fashion with a high-resolution LAM, noting that for climate modelling purposes it is necessary to include a representative range of synoptic weather patterns in the simulations. One means of providing an appropriate range of synoptic situations is to first run a larger scale AGCM and to interpolate the output to LAM resolution at the boundaries of the nested model. These interpolated fields are then used to force the LAM at its lateral boundaries (McGregor et al., 1993b). The AGCM simulation should produce realistic intensities and frequencies of the various types of major synoptic systems. The LAM, with a horizontal grid resolution of approximately 100 km, may simulate some of the mesoscale features leading to a more accurate, detailed and realistic depiction of a region's climate. This is at least possible in mid-latitude domains where the boundary forcing usually determines the broader behaviour of LAM systems (Vucicevic and Paegle, 1989). The climatology of a LAM is determined by the succession of weather events simulated from the contribution of lateral boundary conditions and the internal characteristics of the model. This implies that nested climate modelling is in essence a boundary value problem.

Research groups are increasingly constructing LAMs for climate modelling applications. The main advantage of these models is that they provide a high-resolution climate simulation over a limited domain, whilst remaining much more economical to run than a global model of similar grid resolution. Although LAMs are restricted to a specific domain, they often employ more detailed physical parameterisation schemes than their global counterparts. They also allow for a more accurate representation of topography which is, for example, crucial for the simulation of regional precipitation. If the LAM has a dynamical formulation and physical parameterisation similar to that of the AGCM but a much higher resolution, it adds significant smaller-scale detail to the coarser simulation of the AGCM (Walsh and McGregor, 1995). In general the additional detail results in an improved simulation compared to that of the AGCM. Unlike interpolation methods and statistical techniques (downscaling), the nested AGCM-LAM methodology is a physically based procedure (McGregor et al., 1993b). Note again that the successful application of the nested modelling approach requires that the AGCM provides adequate broad-scale simulations.

While theoretical and scientific problems remain to be solved in the use of nested LAMs, the potential applications are numerous. It is anticipated that LAMs will be coupled on a more regular basis to other components of the earth-atmosphere system such as ocean, sea-ice, biosphere and hydrology models. Lynch et al. (1995) have performed Arctic experiments with an LAM coupled to a dynamic sea-ice model, while Leung et al. (1996) have coupled a LAM to a surface hydrology scheme. There is potential for greatly improved projections of the possible impact of climate change. These projections could take the form of improved estimates of rainfall changes in mountainous catchment areas and better estimates of soil moisture changes in agricultural regions (McGregor et al., 1993b). Further afield there is also a possibility that the impact of future climate change on the accumulation of snow over the Antarctic continent could be better predicted, which would lead to an improved estimate of possible changes in sea level (McGregor et al., 1993b). Provided that suitable sea-surface temperature forecasts are available, there is also a possibility that predictions of the regional effects of El Niño, namely droughts and floods, could be enhanced and made considerably more detailed (McGregor et al., 1993b).

In the next section examples of important mesoscale forcing over southern Africa are presented. Theoretical aspects concerning nested climate modelling are discussed in the remainder of the chapter, with the emphasis on the application of the nested AGCM-LAM methodology on the southern African sub-region.

2.2 MESOSCALE FORCING OVER SOUTHERN AFRICA

Mesoscale atmospheric forcing is primarily induced by complex distributions of surface characteristics such as topography, coastlines, inland water masses and vegetation characteristics. These vary on a scale of 10-100 km. Precipitation is also strongly affected topographically by means of condensation due to topographic upliftment and enhanced convection during summertime. An example that clearly illustrates the impact of topographic forcing on regional scale precipitation is the Klein area of South Africa. Figure 2.1 shows the observed average annual precipitation over this region. Dry conditions normally prevail over the Klein Karoo, which lies in the rain-shadow of the Lange and Outeniekwa Mountains. As a result of the mountains wetter conditions are recorded over and up-wind of the mountain ranges.

Mesoscale forcing can also be of thermal origin, as induced by diverse radiative properties of land and ocean (water) masses. This results in the development land-sea breeze circulation, which significantly influences the local climate of southern African coastal regions. Along the north-west coast of Madagascar, land-sea breeze circulation systems are responsible for the dominant winds

(Jackson, 1954). The strongest sea breezes in southern Africa occur along the Namibian coastline where winds blow in the afternoons from the south or south-west after calm and overcast mornings (Jackson, 1954).

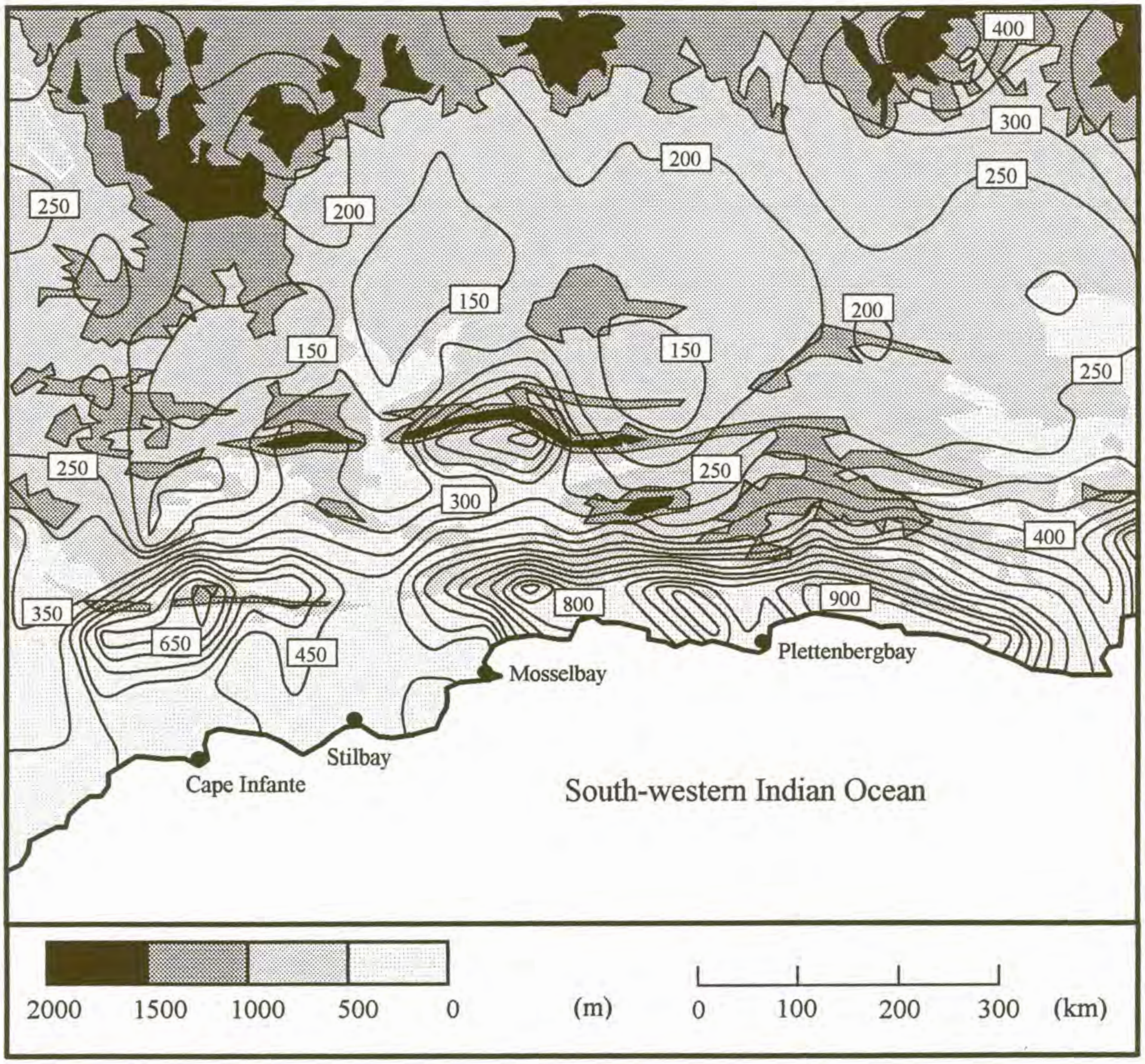

Figure 2.1 Topography (shaded with 500 meter intervals) over the Klein Karoo, Groot Karoo and south coast (20° to 25° east and 32° to 35° south) with isohyets indicating the average annual rainfall measured in millimetres. Note the increase in local rainfall totals against steep slopes of and over higher surface altitudes.

On a daily basis, during summertime, humid and relatively cool air moves over the Natal coast as a result of see breezes. From time to time these circulation patterns intrude as far as 60 km into the interior (Preston-Whyte, 1969). See breeze circulation is normally influenced by the gradient winds of larger scale (synoptic) pressure systems over the ocean (figure 2.2). The combined effect of meso and synoptic scale winds determines how far see breeze flow will intrude into the Natal interior (Preston-Whyte, 1969). The strong gradient in topography also results in the development of mountain-plain winds during the night and valley winds during the day. These circulation systems are present over the entire KwaZulu-Natal (from the Drakensberg to the coastline) (Tyson, 1966; 1968). Interaction between the gradient winds, land-sea breeze circulation and slope-induced circulation may result in complex mesoscale flow.

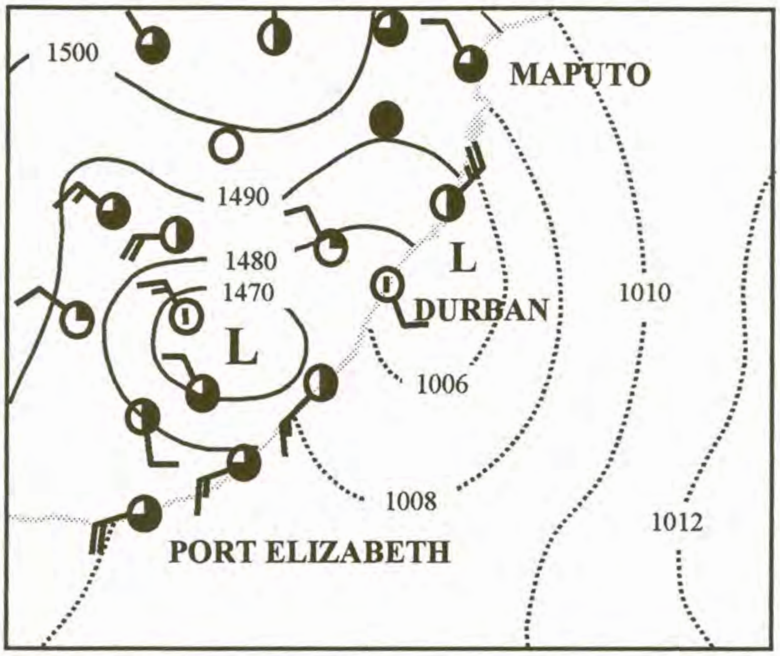

Figure 2.2 Gradient winds induced by a coastal low over the Indian Ocean may deepen the penetration of the sea breeze over the interior of KwaZulu-Natal. Geopotential heights (gpm) of the 850 hPa pressure level over the country (solid lines) and isobars of mean sea level pressure over the ocean (dotted lines) are shown for 14 January 1968 at 14:00 SAST.

Interaction between meso and synoptic scale circulation systems significantly influences the climate of certain parts of southern Africa. An example is the occurrence of heavy local storms over the escarpment of Mpumalanga and the Northern Province in South Africa. These storms are often the product of atmospheric motion on three different scales as indicated in figure 2.3 (Garstang et al., 1987):

- On the synoptic scale a westward moving trough is produced on or above the 850 hPa pressure level, which induces westerly to north-westerly flow over the north-eastern escarpment.

- On the mesoscale a lid inversion develops over the escarpment through either advection or by subsidence of Highveld air. This is normally associated with a low-level easterly flow.

- Local effects amplify both the 850 mb westerly flow over the escarpment and the surface easterly flow of moist Lowveld air.

The surface easterly flow that undercuts the 850 mb westerly flow is probably a product of both the synoptic and mesoscales of motion, with the latter in the form of escarpment heating (Garstang et al., 1987). If the intrusion of moist Lowveld air along the escarpment takes place early and far enough to the west, heavy convective storms occur at the places where no damping inversion has developed through either advection or subsidence.

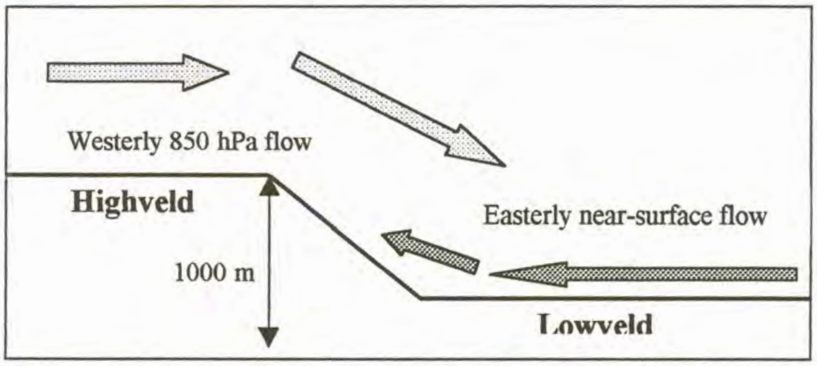

Figure 2.3 Circulation characteristics favourable for the development of heavy convective storms over the eastern escarpment of South Africa (After Garstang et al., 1987).

These examples emphasise the need for high-resolution information in order to characterise the climate of areas in southern Africa where mesoscale atmospheric circulation is important. AGCMs with horizontal grid resolutions in the order of 100 to 500 km are capable of providing information regarding the response of large-scale atmospheric circulation over southern Africa as a result of large-scale forcing. From the discussion in this section however, it is clear that AGCMs are not suitable to simulate detailed atmospheric circulation that results from mesoscale boundary forcing.

2.3 NESTING TECHNIQUES

2.3.1 ONE-WAY NESTING

Nested modelling requires that boundary information to propagate freely into the nested domain and that the nested model does not suffer excessive reflection of its generated flows. The most popular nesting strategy adopted so far is the technique of one-way nesting (figure 2.4). Here the flow of information occurs only from the AGCM towards the LAM. Most NCMs developed to date employ the so-called "relaxation" method to generate meteorological lateral boundary conditions (LBC). The purpose is to force nested model solutions toward the large-scale circulation fields over a lateral boundary zone.

A commonly used scheme is that of Davies (1976). In this scheme several (typically five) boundary rows provide a buffer zone at each time step with full incorporation of the outer solution at the outermost rows, tapering off over the inner rows to the inner solution of the LAM. Different functions can be used as the weighting function. Davies (1976) has carried out one-dimensional wave equation calculations to obtain weights for the tapering, which minimise reflections. Giorgi et al. (1994) and Walsh and McGregor (1995) have adopted exponentially decreasing weights. The functions are chosen to minimise noise in areas adjacent to the buffer zone (Giorgi et al., 1993c). This approach has proven to be effective to ensure a smooth transition between driving condition-dominated and NCM-dominated regimes and to reduce noise (Giorgi and Mearns, 1999). A slightly different one-way nesting scheme (used in the National Centre for Atmospheric Research (NCAR) MM4 model) is that of Perkey and Kreitzberg (1976). This scheme has 4 buffer rows over which tendencies of the variables are weighted.

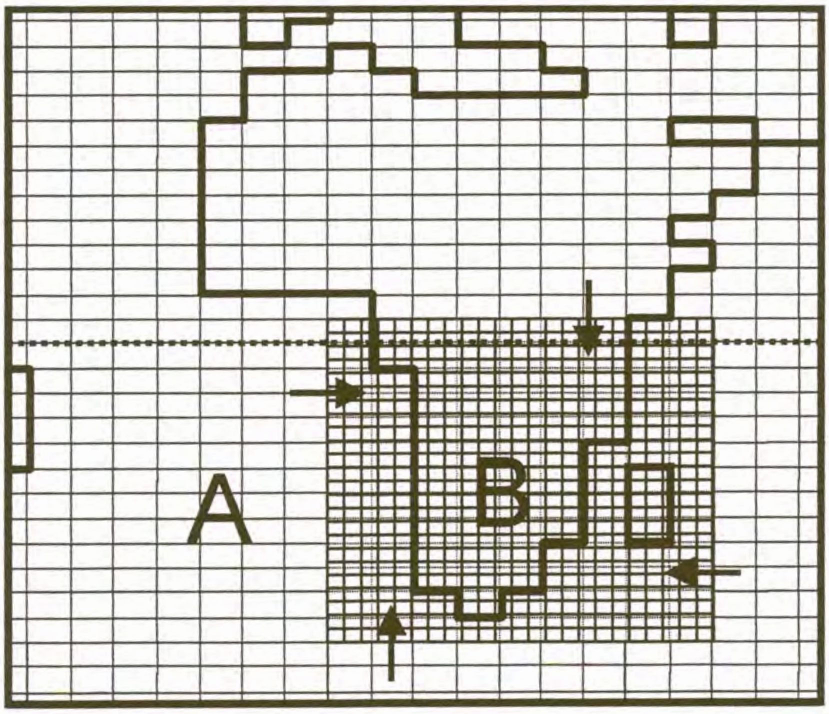

Figure 2.4 One-way nesting over a southern African domain. Information is allowed to flow from the relatively coarse resolution AGCM to the higher resolution nested model. Flow in the opposite direction is not allowed.

The size of the buffer zone varies depending on the model domain. A configuration of buffer zones with only a few boundary points and a linear weighting function tends to produce an unrealistic sharp transition from model solution to driving boundary values (Giorgi et al. 1993c). This results in noise generation near the boundaries that can be substantially reduced by using broader buffer zones and an exponentially varying function allowing for a smoother transition from model solution to driving fields (Giorgi et al., 1993c). For typical continental scale domains most current regional models use buffer zones of 10 grid point width or more. This is usually sufficient to provide a smooth lateral forcing (Giorgi and Mearns, 1999).

Giorgi et al. (1993c) proposed a modification to the standard relaxation technique where a wider buffer zone is adopted in the upper troposphere compared to that of the middle and lower troposphere. The rationale behind this approach is that the large-scale wave patterns and circulation fields in a nested LAM are essentially determined by the driving LBC. Therefore, a relatively wider zone aloft increases the consistency between the nested model and the driving large-scale circulation pattern, in both magnitude and phase. However, the high-resolution forcing resolved by a nested LAM originates primarily at the surface due to topography and coastlines. For this reason the LAM should develop its own internal mesoscale circulation in the middle and lower troposphere, which is achieved by reducing the size of the buffer zone and thus the direct boundary forcing (Giorgi and Mearns, 1999).

Overall the simple standard relaxation technique, if carefully designed, has proven to be adequate for most LAM applications and is therefore widely used. The main problem encountered with this technique is the occurrence of spurious precipitation near the downwind domain boundaries (Giorgi and Mearns, 1999). In a three-dimensional atmospheric model, the disturbances have complicated structures and travel from many directions. This implies that full attenuation of the reflections is not achieved. The residual reflections are primarily manifested near the horizontal boundaries in the divergence field, which may lead to some noise in the vertical velocity and related precipitation patterns (McGregor et al., 1993b). Although precipitation patterns may appear somewhat noisy near the boundaries, it should be noted that this noise does not normaly lead to contamination of the interior fields. This is because the AGCM moisture and temperature fields strongly override the modifications made to the heating and drying of the LAM in this boundary zone (McGregor et al., 1993b). At the surface however, the water budget and surface energy may be negatively affected (Giorgi and Mearns, 1999). Problems related to sharp transitions at the lateral boundaries can be improved by using multiple nesting or variable resolution configurations (Giorgi and Mearns, 1999, also see section 2.11).

The possible interpolation errors and the generation of noise implies that the abrupt change in model and driving data resolution at the lateral boundaries should be minimised. One way to decrease the driving model's resolution mismatch is to use a multiple nested mesh (Giorgi and Mearns, 1999). Multiple nesting can be done using either one-way or two-way (see section 2.3.3) nesting. An alternate technique is to use the variable resolution approach proposed by Qian et al. (1999). In this approach the grid resolution of the LAM should match that of the driving model in the lateral boundary zone but should gradually increase towards the interior of the domain, where a uniform fine resolution grid is placed. In both the multiple nested and variable resolution approaches the mismatch between the large-scale driving fields and LAM simulated fields are minimised. The model's computational efficiency could improve significantly since fewer grid points may be used in the buffer zone (Giorgi and Mearns, 1999).

A LAM may be nested in either objective analysis provided by forecast centres or in output provided by global AGCMs. Multiple nesting down to finer scales has also been performed, within an AGCM by McGregor and Walsh (1994) and within observed analysis by Leung et al. (1996).

An important issue concerning LBC provision is the interval of updates of the large-scale fields. Nested model LBC are needed at each time step and are usually linearly interpolated (in time) from two adjacent large-scale field updates (Giorgi and Mearns, 1999). Typically the analysis or AGCM output is available every 3 to 12 hours and these are interpolated in time and space to lateral boundary points as required during the simulation. At each time step the outermost boundary points of the nested LAM are relaxed toward the interpolated values. In general it is preferable not to select update intervals greater than 12 hours as this might cause the model to misrepresent systems rapidly moving across the lateral boundaries (Giorgi and Mearns, 1999).

For summertime simulations over southern Africa it would be preferable that the LBC updates occur at least every 6 hours to represent the diurnal cycle. This is necessary because differential heating associated with the diurnal cycle may cause local overturning of mesoscale circulation overland (Giorgi and Mearns, 1999). Experiments by Dickenson et al. (1989) showed that during winter, when the diurnal cycle is not pronounced, the model sensitivity to LBC update intervals from 3 to 12 hours is small. Likely, the importance of the frequency of LBC updates depends on domain and season, so it is always advisable to assess the model sensitivity to the update frequency and to use the highest frequency available (Giorgi and Mearns, 1999).

When applying one-way nested models to regional climate simulation, it is assumed that the development of systems within the model domain is constrained by the forcing from the AGCM provided boundary conditions. The boundary conditions provide means of removing flow inconsistencies, at least in regions where weather systems regularly sweep through the domain (Errico and Baumhefner, 1987). It might be expected that the one-way nesting technique would perform better in mid-latitude regions than in the tropics. In equatorial or tropical latitudes, where weather patterns move more slowly than in mid-latitude regions, it may happen that quasi-stationary systems develop within the nested domain. These have a life somewhat independent of the AGCM forcing (Walsh and McGregor, 1995). Thus, the one-way nesting approach has some theoretical limitations especially in the tropics where the "stationary problem" restricts the applicability of the technique. Nevertheless, Walsh and McGregor (1995) performed successful climate simulations over the Australian region. Included in their LAM domain were extended tropical regions both north and south of the equator.

2.3.2 SPECTRAL NESTING

A different one-way nesting technique has been proposed by Kida et al. (1991) and Juang and Kanamitsu (1994). It was previously believed that difficulty in prescribing the lateral boundaries would make spectral techniques inappropriate for nested limited-area modelling. Despite this Tatsumi (1986) developed a spectral LAM. His spectral model uses a Fourier expansion in the horizontal, with the lowest order coefficients provided from the large-scale fields. This results in a unique nesting technique.

The outer model (eg. AGCM) provides an average forcing over the whole domain, rather than just over the boundaries (McGregor et al., 1993b). The regional model solves the high wave-number component. This strategy ensures full consistency between the nested model and large-scale driving fields and presents a different philosophy concerning the role of the nested LAM (McGregor, 1997a). Spectral nesting avoids any necessity to match the LAM and AGCM topography and parameterisations (McGregor, 1997a; also see section 2.5). The technique has the disadvantage of preventing the formation of surface-forced secondary systems in the regional model that are not present in the driving fields (Giorgi and Mearns, 1999). It has yet to be demonstrated whether the extra constraints of the technique lead to a generally better or worse simulated climatology (McGregor, 1997a).

More recently Sasaki et al. (1995) modified the spectral nesting technique to allow full spectral nesting above 500 hPa only, and conventional LBC nesting at lower levels. This approach was followed in order to provide improved results with respect to the full spectral nesting, primarily because of the difficulty to nest the water vapour fields in the lower troposphere by means of spectral nesting (Giorgi and Mearns, 1999). This modified spectral method is conceptually similar to the modified conventional method of Giorgi et al. (1993c) and both methods appear to converge toward a criterion of stronger forcing in the upper, and weaker forcing in the middle and lower-tropospheric layers (Giorgi and Mearns, 1999).

2.3.3 TWO-WAY NESTING

In the one-way nesting approach the circulation produced by the nested LAM does not feed back into the global model. Ideally, there should be a two-way flow of information, which implies that flow inside and outside the LAM domain should interact in a single dynamic system. The latter approach is very attractive for specific locations and some difficulties experienced in the tropics with the one-way nesting approach are avoided (McGregor, 1997a). Improved simulations should be expected from the two-way nested technique (McGregor, 1997a).

Two-way interacting nested climate modelling experiments between AGCMs and LAMs have however not been attempted to date. One reason for this is the technical difficulty involved in fully coupling two complex model systems when the inner and outer models have different formulations, e.g. grid versus spectral. It is even more difficult when the outer model is a climate model as arbitrary modification of the outer model solution can act as an artificial source or sink of energy that can upset its conservation properties (McGregor et al., 1993b). Two-way nesting also presents the need to perform separate climate runs for each geographic configuration, which implies a lack of flexibility especially for long simulations. The model may also need to be re-tuned before every new configuration (McGregor, 1997a).

One way to facilitate coupling of global and LAM is to modify the spatial grid resolution of the LAM from a fine resolution over the area of interest to a coarser resolution over the rest of the globe. By matching grid resolutions from the two models at the lateral boundary area where the exchange of information takes place, inconsistencies associated with sharp contrasts in model resolution are minimised (Qian et al., 1999).

2.4 DOMAIN SIZE, RESOLUTION AND LATERAL BOUNDARIES

Experiments have been performed over Europe to study the effect of domain size on LAM simulations. Jones et al. (1995) concluded that the LAM domain should be sufficiently small in order to prevent simulated atmospheric circulation of the nested model departing from that of the driving AGCM on the synoptic scale. The domain also needs to be large enough, however, to prevent the coarse scale lateral boundary conditions from dominating the solution over the area of interest. More detailed simulations of atmospheric features representing a finer scale than those skilfully resolved by the AGCM should be achieved by the LAM (Giorgi and Mearns, 1991; Jones et al., 1995; Podzun et al., 1995). The horizontal resolution of the nested model therefore has to be fine enough to capture forcing and atmospheric circulation on the mesoscale.

The selection of domain size and horizontal resolution is generally determined by a compromise between meteorological and computational considerations. An increase in model domain size and a refinement in resolution are achieved at the cost of increased computation time. Stability considerations yield that the model time step has to decrease with the grid point spacing. As stronger vertical velocities are produced with a refinement in horizontal grid resolution, it is recommended that the vertical resolution is increased to maintain stability (Giorgi and Mearns, 1999). This implies that the relationship between computation time and model resolution is stronger than linear.

The model domain should encompass, to the extent feasible, all regions of forcing and atmospheric circulation that directly influence the climate and climate variability over the area of interest. For example, a domain over southern Africa should include the Agulhas retroflection region in the south-western Indian Ocean (Engelbrecht and Rautenbach, 2001) and Madagascar to the east (Joubert, 1998). Such a domain also needs to extend far enough over the Atlantic Ocean to adequately capture the development and propagation of mid-latitude cyclones (frontal troughs) and far enough to the north to capture tropical features such as the semi-stationary tropical surface trough.

It is also recommended that the model resolution should be fine enough to capture the forcing and atmospheric circulation of interest. For example, a study focussing on the eastern part of South Africa needs to employ a resolution capable of capturing the eastern escarpment at the atmospheric circulation scale of interest. A study focussing on equatorial Africa needs to employ a resolution capable of capturing mesoscale forcing and circulation induced by Lake Victoria. Studies focussing on agriculture in the Vaal River catchment area in South Africa may require information from the scale of a few tens of kilometres, while studies concerning the advection of trace gasses over the SADC region may require information at sub-continental scale. Thus, the model resolution must be of such a nature that useful information for specific applications is produced.

Another factor that influences the selection of model resolution is the suitability of physical parameterisation schemes and approximations of dynamical processes in the atmosphere. The validity of the hydrostatic assumption decreases significantly for horizontal scales smaller than approximately 10 kilometres. The same principle applies for the assumption of scale separation inherent in most cumulus parameterisation schemes (Giorgi and Mearns, 1999). In addition to this, different cumulus parameterisation schemes are often developed for specific spatial scales. Examples include the scheme of Anthes (1977), that has been developed for scales between 60 and 120 km, as well as that of Fritsch and Chappel (1980) who focus on scales of a few tens of kilometres.

Some care is also needed when locating the boundary zone. It is recommended that the occurrence of land-sea interfaces in the boundary zone is minimised to avoid problems of matching coastal outlines and attendant sensitivity of surface physical routines (McGregor et al., 1993b). In general it is preferable to place the lateral boundaries over the ocean rather than over land to avoid possible effects of unrealistic surface energy budget calculations near the boundaries (Giorgi and Mearns, 1999). Another reason for placing the boundaries over the ocean is the increased possibility of the formation of spurious precipitation near the lateral boundaries if placed over land and steep topography (Giorgi and Mearns, 1999).

It is also particularly advisable to avoid placing the domain boundaries over areas of complex topography. The mismatch between the coarse resolution (AGCM) driving data and fine resolution model topography may not only produce significant noise but often requires an extrapolation of variables below the surface level of the driving fields (Giorgi and Mearns, 1999). McGregor et al. (1993b) suggested the use of the smoothed AGCM terrain in the boundary zone of the LAM to avoid problems arising from vertical interpolation. In the nested model DARLAM, boundary fields are altered to compensate for any differences in altitude between the AGCM and LAM that may occur in the interpolated topography (McGregor, 1997a).

Finally, it is useful to select a domain where the area under investigation is located as far as possible from the lateral boundary zone. This prevents boundary region noise generated from excessively contaminating the solution over the area of interest. It also minimises the influence of the coarse resolution lateral forcing on the internal model physics of the LAM (Giorgi and Mearns, 1999).

2.5 PARAMETERISATION SCHEMES

Both AGCMs and LAMs require a comprehensive set of physical parameterisation schemes for processes that occur on sub-grid scales. Examples of physical processes include radiation, cloud formation, latent heating (especially in cumulus convection), vertical transfer in the lower boundary layer (the lowest 1 km of the atmosphere) and atmosphere-surface interactions (including ocean-atmosphere and ocean-biosphere interaction). Some of these processes are described in McGregor et al. (1993a). With finer resolutions, LAMs require particularly careful treatment of surface, soil and vegetation interactions (McGregor, 1997a). Wherever possible the parameterisation schemes are based on observations.

Parameterisation of cumulus convection and cloud estimation proved to be the most difficult since the parameterisation formulation strongly depends upon grid spacing. Cumulus convection parameterisation also needs to handle a wide range of conditions. For example, in the tropics there is abundant moisture and weak winds, whereas convection associated with mid-latitude systems typically occurs in a drier environment with stronger winds. The simulated precipitation patterns and the corresponding heating rates in the tropics are extremely sensitive according to the selection of a cumulus parameterisation scheme (Krishnamurti et al., 1980; Horel et al., 1994). Other tests indicated that tropical nested simulations are sensitive to the numerical formulation of vertical advection (Walsh and McGregor, 1995) as well as to the radiation scheme decided upon. If the LAM develops a cool bias in the tropics compared to the AGCM or observed analysis, spurious boundary inflow or outflow may be generated resembling a large-scale sea breeze (McGregor, 1997a). Therefore, the generality and suitability of a specific parameterisation scheme has to be investigated before it is used by means of sensitivity experiments in regional model simulations (McGregor et al., 1993b). These issues are important for LAM experiments over the SADC region, which includes extended areas located in both the tropics and mid-latitudes. Although a parameterisation scheme formulation is supposed to cope with a wide range of environmental conditions, it is advisable to apply diverse parameterisation schemes over regions with diverse weather phenomena (McGregor et al., 1993b).

McGregor (1997a) states that in general, physical parameterisation schemes in a LAM should be compatible to those in the driving AGCM. In particular, experiments with DARLAM indicated that the LAM and AGCM should use similar cumulus parameterisation schemes over the tropics (McGregor, 1997a). This ensures that maximum compatibility between the models is achieved (Giorgi and Mearns, 1999). LAM simulations may be used to investigate and test the high-resolution performance of parameterisation schemes of AGCMs (McGregor, 1997a). An important disadvantage when using the same parameterisation schemes in LAMs and AGCMs, is that physical schemes developed for course resolution AGCMs may not always be adequate for application in the finer resolution LAMs. Parameterisation schemes show significant sensitivity to horizontal resolution and thus can result in different behaviours in the nested and driving models (Giorgi and Mearns, 1999).

An alternative approach is to use different physical parameterisation schemes in the nested and driving models, where the schemes for each model are specifically developed and optimised for the respective model resolutions. A disadvantage of this approach is that it is often difficult to interpret differences in results since these are affected by not only diverse resolution forcing but also by differences in the physics schemes used (Giorgi and Mearns, 1999). Another potential disadvantage is that the parameterisation schemes may cause different forcing leading to spurious circulation in the interior of the domain (Giorgi and Mearns, 1999).

Giorgi and Mearns (1999) indicated that a LAM “sees” two important aspects namely initial and lateral boundary fields. The use of similar or different physics when driving LAMs can both lead to good quality simulations in the presence of good quality driving fields. LAM simulations are continuously improving as better parameterisation schemes are developed and as model resolution is further refined (McGregor, 1997a).

2.6 ATMOSPHERIC MODEL FORMULATIONS

The following discussion is based on that of McGregor et al. (1993b). As far as atmospheric science is concerned, there has been considerable development in numerical techniques during the past few decades. This includes the implementation of both spectral and grid-point representations, implicit and explicit time differencing schemes as well as the more recent semi-Lagrangian schemes. Atmospheric models may be integrated for several days to generate medium-range weather predictions or for extended periods for climate simulations. Models used for both applications are similar, although for climate simulations there is a strong emphasis on the overall conservation of physical quantities to reproduce the long-term behaviour of the atmospheric circulation. Several aspects concerning the dynamical and numerical formulation in AGCMs and LAMs are discussed in the following sections.

2.6.1 SPECTRAL MODELS

Most present day AGCMs are formulated in terms of an expansion in spherical harmonics. Examples include the spectral models of the Australian Bureau of Meteorology Research Centre (BMRC), the Canadian Climate Centre, the CSIRO in Australia, the European Centre for Medium-range Weather Forecasting (ECMWF), the Geophysical Fluid Dynamics Laboratory (GFDL) and NCAR. As an alternative finite difference methods on a grid, as employed in the United Kingdom Meteorological Office and Goddard Institute for Space Studies models,

i 15779373
b15231562

are also used in the so called "grid models". Spectral models can be designed to have highly self-consistent numerical formulation and accurate advection properties. Disadvantages include a tendency to smear out sharp gradients that may, in particular, affect moisture as well as the spectral smoothing of topography near coastlines. This complicates the specification of appropriate sea-surface temperatures.

It was previously considered that difficulties in prescribing the lateral boundaries would make spectral techniques inappropriate for limited-area modelling. However, a spectral LAM has been developed recently by Tatsumi (1986) (See section 2.3.2 for more details).

2.6.2 THE HYDROSTATIC APPROXIMATION

All climate models and most weather prediction models employ the hydrostatic approximation. The hydrostatic approximation embedded in the equations of motion assumes that vertical acceleration in the atmosphere is negligible compared to the other terms in the vertical momentum equation. The assumption allows for sound waves to be filtered out from the solutions, implying that relative large time steps may be achieved during model integrations. The vertical equation of motion reduces to an expression giving the height of a column of air as an integral of temperature with respect to the logarithm of pressure (hypsometric equation). The hydrostatic approximation is found to be valid for grid resolutions courser than 10 to 20 km (McGregor et al.,1993b; Giorgi and Mearns, 1999). For smaller grid lengths, inaccuracies may arise over steep terrain or during deep convection. The approximation's validity is consistent with the intuitive expectation that sound waves are considered as unimportant for the scale of atmospheric circulation considered in climate modelling.

2.6.3 CONSERVATION PROPERTIES

With the exception of the CSIRO model, all the spectral and grid point AGCMs listed in section 2.6.1 are formulated using the advective formulation of the equations of motion. The advective formulation attempts to achieve accurate horizontal transport and is written in terms of the basic wind components, temperature, surface-pressure and mixing ratio of water vapour. As an alternative the equations of motion may also be written in flux form (CSIRO model) using the original variables weighted by mass. In this form it is fairly straightforward for a grid point AGCM to guarantee conservation of mass and energy. It is more difficult to prove conservation of mass and energy in spectral models and many of these models just rely on the inherent accuracy of the spectral technique. LAMs may use either the advective or flux formulation. However, for a limited domain, conservation behaviour is dominated by fluxes across the lateral boundaries, which are supplied periodically by the outer AGCM (see section 2.3). Because of the sampling and interpolation considerations at the lateral boundaries, the conservation properties of the original equations provide little guidance for selecting the appropriate formulation for a LAM. The continual boundary forcing is, however, designed to keep the large-scale circulation features in the LAM similar to those of the driving AGCM. For this reason, conservation is not such an important issue in LAMs (McGregor, 1997a).

2.6.4 STAGGERED GRIDS

The majority of modern grid-point models employ grids in which the wind components are staggered horizontally with respect to the other variables. This staggering improves the accuracy of the pressure gradient terms in the momentum equations and leads to improved dispersion characteristics for gravity wave response (Schoenstadt, 1980). It also avoids spurious noise caused by solution decoupling over the grid (McGregor and Leslie, 1977). The Australian Bureau of Meteorology (McGregor et al., 1978; Leslie et al., 1985) and the CSIRO (McGregor, 1987) use LAMs with grids where the wind components are staggered half a grid length in their respective direction of motion. Purser and Leslie (1988) have found that non-staggered grids may be successfully used provided that high-order horizontal differencing and judicious filtering are employed.

2.6.5 HORIZONTAL ADVECTION

The selection of horizontal advection (i.e. transport) scheme can affect the degree of noise of the solution and the model's ability to maintain sharp gradients. Many grid-point models have used centred finite differencing of second or fourth order, or Lax-Wendroff schemes (Gadd, 1978b; Haltiner and Williams, 1980). In the last 15 years semi-Lagrangian techniques have been adopted for both LAMs and global weather prediction models, including the ECMWF model (Ritchie, 1991). The technique is based on finding an upwind departure point for each grid point (McDonald and Bates, 1987; McGregor, 1993), after which higher-order interpolation is used to obtain appropriate model variables at the departure point. The advection of water vapour improved significantly when using the semi-Lagrangian technique. Another important feature of semi-Lagrangian schemes is that significantly larger time steps can be achieved relative to other schemes. These aspects are discussed in more detail in Chapter 4.

2.6.6 TIME DIFFERENCING

Although the hydrostatic approximation removes fast travelling sound waves, the equations of motion still permit horizontally propagating gravity waves with phase speeds up to 300 ms^{-1}. Explicit models such as the NCAR MM4 model (Anthes et al., 1987) are constrained by these large phase speeds and require a very small time step to meet numerical stability criteria. With the split-explicit method, the gravity wave generating terms are split apart and solved with a small sub-time step embedded in each main time step (Gadd, 1978a). However, the most common treatment is to group the linear components of the terms contributing to gravity waves, and solve those implicitly. Robert et al. (1972) describes this technique in more detail. The semi-implicit method leads to a Helmholtz equation. This equation may be solved by using either iterative or direct methods, or analytically in the case of a spectral model, where it enables the use of a larger time step to be used.

2.7 SPIN-UP TIME AND INITIALISATION

Initial conditions for a LAM are supplied by observation analysis, or by forcing from an AGCM. Variables such as temperature, sub-soil temperature and moisture, and surface albedo may exhibit discontinuities at topographic interfaces, for example land-sea boundaries, or boundaries of different vegetation or soil types. Special interpolation methods need to be employed to initialise these variables near these interfaces (McGregor, 1997a).

Another consideration during initialisation is the vertical interpolation of AGCM atmospheric fields (especially temperature) to pressure levels as defined for the LAM, and to adjust the surface pressure to the new altitudes resulting from the more detailed finer resolution of the LAM's topography. Vertical compensation is also required near the boundary rows whilst nesting, if the topography of the AGCM and LAM differ (McGregor, 1997a).

Atmospheric spin-up time can be defined as the time taken by the LBC to pervade the nested model domain and generate a dynamical equilibrium between the LBC information and the internal model physics and dynamics. The spin-up time varies depending on the domain size, season and circulation intensity, but is typically in the order of a few days (Errico and Baumhefner, 1987; Anthes et al., 1989). In a LAM simulation the deviation of the model solution from the larger scale driving fields will tend to increase for the first few days of spin-up, where after it will oscillates around an asymptotic stage (Giorgi and Mearns, 1999). When the asymptotic stage (which depends on domain, season and location) is reached, the model simulates weather events that either enter the domain from the lateral boundaries or are generated in the interior of the domain with a relatively constant level of skill (Giorgi and Mearns, 1999).

A factor that contributes to complications of the spin-up procedure and model climatology is soil moisture and soil temperature initialisation. Soil water content and temperature affect weather and climate, especially during the summer, since it modulates surface and latent heat fluxes (Giorgi and Mearns, 1999). The temperature and water content of a surface soil layer of say, 10cm depth, equilibrate with the overlying climate relatively quickly (in the order of a few weeks). For a root zone of 1m depth, the equilibrium may be in the order of several seasons, while for deeper soil, it may be in the order of several years (Giorgi and Mearns, 1999). This problem is further complicated by the fact that reliable information for soil moisture and temperature initialisation is not available. Thus, if a nested model includes a soil module of several meters in depth, strict equilibrium occurs only after years of simulation. However, since the most hydrological active region is the rooting zone (order of 1m or less), for most practical purposes the soil spin-up can be considered as of the order of a few seasons to a year. This estimate depends on the sensitivity of individual models to soil moisture conditions (Giorgi and Mearns, 1999).

2.8 MODEL INTEGRATION PERIODS

As indicated, the atmospheric circulation properties of a LAM are dictated by the succession of weather events as simulated from the contribution of LBC and internal model physics after an atmospheric spin-up of several days. In LAM simulations the first days of spin-up are usually neglected in the analysis of results (Giorgi and Mearns, 1999).

A major aspect when performing climate simulation experiments has to do with the length of integration period required for producing a stable climatology. For example, observed average rainfall at a fixed location over a period of 10-years will, in the absence of climate change, only differ slightly from the average rainfall over a 20-year period. An average from a 1-year period will, however, differ significantly from a 10-year average, especially if a flood or a drought occured in the 1-year epoch. Climate models exhibit analogous patterns of internal variability (McGregor et al., 1993b). They are also sensitive to the prescribed SSTs, and would exhibit increased variability in the event where El Niño events are captured in model simulations. In order to obtain a stable average climate from a model, it is recommended that a simulation of at least 10-years is performed (Miyakoda et al., 1972). However, Walsh and McGregor (1995) point out that some differences between long-term monthly averages could still be expected due to sampling errors that is caused by the fact that climatological averages are produced by averaging relative small groups (for example 10-years) of ensemble members.

A popular strategy to produce a model simulated climatology for a specific month is to nest separate simulations for that month rather than to perform seasonal cycle runs. Here, a model simulation is constructed by running multiple 30-day simulations of a particular month for successive years and then averaging the results to obtain a climatology for that month. Model simulations of at least 10 to 20 individual months in this mode is required in order to provide a stable climatology (McGregor, 1997a). This methodology has been followed in several studies using the NCAR MM4 mesoscale model and DARLAM. The LAMs may also be nested within observed analysis, (Giorgi and Morinucci, 1991; Giorgi et al., 1993a, b; Walsh and McGregor, 1996) or within AGCM simulations (Giorgi, 1990; McGregor and Walsh, 1994; Marinucci et al., 1995; Walsh and McGregor, 1995). See McGregor (1997a) and Chapter 3 for more examples.

A less versatile approach with respect to the duration of the simulations is to perform a perpetual run for a particular month, say January, nested within a perpetual January GCM (McGregor and Walsh, 1993). It is, however, necessary to prescribe the deep soil moisture temperatures for perpetual runs, which normally restricts their applicability to present day conditions (McGregor, 1997a). However, Hostetler et al. (1994) were able to use 90-day perpetual January and

July simulations to study the role of lake-atmosphere feedbacks in sustaining paleolakes 18 000 years ago.

More recently, with the improvement in computer capacity, multi-year seasonal cycle simulations have been performed (McGregor, 1997a; Chapter 3). These seasonal-varying simulations are slightly more accurate than those run in individual-month mode. The reason for this is that these runs allow for soil moisture and temperature to evolve realistically over longer time scales (McGregor, 1997a). In this manner most problems associated with atmospheric spin-up time are avoided. The model is also allowed to develop its own internal atmospheric circulation (Giorgi and Mearns, 1999). In addition, along term simulation allows for an improved equilibrium between the model climate and surface hydrological cycle as well as a improved detection of systematic deficiencies in the internal model physics (Giorgi and Mearns, 1999).

Another possible way to produce simulated climatologies for the entire annual cycle is to force both the AGCM and LAM with observed climatological SSTs (model SST climatology). Multiple seasonal cycle simulations might be obtained when starting each simulation with slightly different initial conditions. This procedure is followed because of the non-linear nature of the atmospheric equations and internal chaos. A multiple-member ensemble mean of output variables constitutes the model climate. About five realisations of each model are necessary in order to reduce the effect of internal variability. This approach was used by Engelbrecht and Rautenbach (2001) to obtain a model climatology from the T63 version of the CSIRO9 Mark II AGCM. It may also be required that a short spin-up period of approximately a month precedes the model simulation. This will allow for physical processes, like the moisture cycle, to reach equilibrium (McGregor, 1997a).

2.9 VERIFICATION OF NESTED MODELS

According to McGregor et al. (1993b), the ultimate verification of a nested climate model is to compare a sufficiently long simulation with the current climate. This should include climate verification of aspects such as storm statistics and frontal intensities. Simulations of the order of a month or longer pose additional requirements to the models if compared to the more conventional short-term simulations. This is because most parameterisation schemes have a long time scale (such as the effect of radiation on the flow). These simulations may be verified against the observed mean climatology for the period under consideration. It is vital to make sure that long-term biases are not accumulating in the interior of the domain. This is more likely to happen in the tropics. For control experiments, one has to keep in mind that the veracity of nested LAM simulations greatly depends upon the veracity of the broad-scale aspects of the AGCM simulation (McGregor, 1997a).

A measure of the minimum error one might expect from the LAM may be obtained from nesting the model within observed analyses. This mode of verification may also provide a way to verify LAM parameterisation schemes (McGregor et al, 1993). Recently, many meteorological centres have routinely run their limited-area weather prediction models for one-month simulations in order to determine model biases and reveal deficiencies in model parameterisation schemes. This contributes to model development (D. Majewski; personal communication to J.L. McGregor) and led to improvements in the various regional data assimilation systems (McGregor, 1997a).

Since a major objective of nested LAM runs is to simulate mesoscale features that affect a specific region, it needs to be verified that the LAM realistically simulates those features. (McGregor et al., 1993b). For example, the ability of a LAM to reproduce weather systems can be verified by performing case studies of significant meteorological events and to compare the results with observations. Boundary conditions for the LAM may be specified from operational grid-point analyses (also regarded as observations), and the LAM simulation compared to the subsequent analyses and observations.

Verification of LAM simulations can be problematic since a LAM might generate output on a higher spatial resolution than available from the upper atmosphere observational network. At the same time the model may not have enough resolution to simulate the surface observed fields (30 to 150 km nested model grid box averages versus denser point observation fields). One approach is to verify model simulations against the track and intensity of weather phenomena and observed accumulated precipitation, at least over land (McGregor et al., 1993b). Occasionally there are special observation programmes that provide higher spatial and temporal data to initialise models and to verify the simulations. McGregor et al. (1993b) provide some examples. In South Africa, a high-resolution rain gauge and radar rainfall observation network over the Vaaldam catchment area may prove to be ideal for LAM rainfall verification.

2.10 OTHER APPLICATIONS FOR NESTED MODELLING

LAMs have recently been employed for climate modelling. Here, simulations that extend over long periods are required. During the last twenty-five years LAMs have widely been used to make significant improvements in short-range weather forecasting, while case and mechanistic studies utilising LAMs furthered the understanding of mesoscale weather phenomena. Keyser and Uccellini (1987) discuss the use of regional models as an aid to explain and understand mesoscale weather events. They note that these models have become sufficiently accurate and have enough temporal and spatial resolution to provide a better understanding of atmospheric dynamics than possible with observed analyses.

In recent years LAMs have been used to investigate Australian weather systems such as east coast lows, tropical southerly busters affecting Sydney, the pollution-inducing Melbourne eddy and dispersion of pollutants (McGregor et al., 1993b). In South Africa recent applications of LAMs include investigations of air mass transport and associated moisture sources during cyclone Demoina (Crimp et al, 2000) as well as an investigations concerning the extreme precipitation events during 11 to 16 February 1996 (Crimp and Mason, 2000). The latter investigation utilised the Colorado State University Regional Atmospheric Modelling System (RAMS). The sensitivity of a tropical-temperate troughs to sea-surface temperature anomalies in the Agulhas retroflection region has also been investigated, again using RAMS, by Crimp et al. (1998).

The generality and suitability of the parameterisation experiments for different weather phenomena may be investigated by sensitivity experiments in LAM simulations. Furthermore, since the same physical parameterisation schemes are often used in both LAMs and AGCMs, LAMs may be used to provide a framework for testing the high-resolution performance of these parameterisations (McGregor, 1997a).

The relative importance of a given process in a weather event can also be investigated using a LAM, where the process can be altered or even eliminated. A comparison of the full model simulation with the altered simulation can give an indication of the importance of such a process. It must be kept in mind however, that non-linear interactions and feedbacks between various physical processes may prevent a clear determination of the importance of a process. The development of a weather system depends on the interaction of many of the various processes and not on a simple addition of the effect of a specific process (McGregor et al., 1993b).

Detailed simulations produced by LAMs make it possible to construct geographically detailed scenarios of climate change (Walsh and McGregor, 1995). For most simulations performed to date (some of these are discussed in Chapter 3) the overall climate change scenarios produced by the LAMs are similar to those provided by the AGCMs. There are, however, significant differences in finer detail, particularly for precipitation (McGregor, 1997a). The impact of a changing climate on local weather systems can also be examined through sensitivity experiments with a LAM. For example, it is likely that SSTs will increase with an increase in atmospheric CO_2 concentrations (Houghton et al., 1990). Typical weather systems may be simulated by LAMs with an enhanced SST to determine the possible effect of ocean heating (McGregor et al., 1993b).

2.11 ALTERNATIVES TO NESTED CLIMATE MODELLING

A new approach that may prove to be a suitable alternative to two-way nesting is that of running a global model with highly variable resolution (Courtier and Geleyn, 1988). The model horizontal grid point spacing is gradually refined toward the area of interest. This approach is very appropriate for specific locations on the planet. Difficulties experienced in the tropics with the one-way nesting approach can be avoided (McGregor, 1997a). Déqué and Piedelievre (1995) have successfully developed a variable resolution spectral model and grid point variable resolution global climate models are under development at the CSIRO (McGregor, 1996, 1997b).

Variable resolution global models may also have some disadvantages. The relative course resolution far from the area of interest may negatively influence the simulation and parameterisation schemes may not be adequate for use on a wide range of spatial scales (Giorgi and Mearns, 1999). Another disadvantage is that the time step needs to be shorter in a variable resolution domain than required without the local mesh refinement (Giorgi and Mearns, 1999). As in the two-way nesting technique, there is a lack of flexibility since the model has to be modified and independently run for each new geographic configuration (McGregor, 1997a).

2.12 UNCERTAINTIES AND A VIEW OF THE FUTURE

Despite the considerable potential of nested climate modelling there remain several unresolved issues which indicate that we are dealing with a relative new science. Presently all LAMs experience difficulties in regions of high and steep topography where long-term average precipitation is often over-estimated. At present the reasons for this overestimation are uncertain but possibilities include precipitation errors associated with the calculation of pressure gradients in terrain-following co-ordinates. This problem is discussed in more detail in Chapter 3. As previously discussed, there are uncertainties regarding the applicability of LAMs in tropical regions, where there is minimal synoptic forcing supplied by the appropriate AGCM to the LAM.

Results from NCAR depict substantial sensitivity to the initial specification of soil moisture (Giorgi and Marinucci, 1991), although this behaviour may be related to the exclusion of an adequate parameterisation for non-precipitating cumulus clouds. Data for initialisation of soil moisture remains sparse. It is known that present AGCM simulations of soil moisture are inadequate (Vinnikov and Yeserkepova, 1991), either as a result of deficiencies in the representation of hydrological processes or errors in the atmospheric fields. Improvements are anticipated when using LAMs because of their potential to achieve more accurate and detailed precipitation simulations (McGregor et al., 1993b).

Successful LAM simulation experiments have been performed by various groups for periods ranging from 1 month to several years (see Chapter 3). Consistent success has been demonstrated for NCMs in mid-latitudes where improved climatological patterns of precipitation and screen temperature (which is particularly related to topographic and coastal effects) have been simulated. Significant improvements are also detected in the details provided in nested LAM climatologies when compared to those of the associated AGCMs, especially for coastal and mountainous regions. Nested climate modelling has become popular, not only for producing detailed simulations of climate and climate variability but also as a tool for the improvement of LAMs and their internal parameterisation schemes (McGregor, 1997a).

With the inclusion of trace gas transport schemes and middle atmospheric chemistry in AGCMs (Rasch et al., 1985) the advection of trace gasses can also be incorporated in LAM experiments. Simple parameterisation of the surface sources and sinks of CO_2, SO_2 and radon have been incorporated in DARLAM (McGregor, 1997a).

There are several ways for future development in this challenging research field. According to McGregor (1993), improved physical parameterisation schemes for physical processes, cloud simulation and radiation properties are required, both for LAMs and AGCMs. Some of these improvements will follow from analysis of the new global data sets being acquired from remote sensing. Simulation of present-day climate will also be enhanced by the availability of improved SSTs, surface albedo, surface roughness and vegetation characteristics. NCM simulations will continue to improve with further refinement of model resolution. As further improvements are made to the climatology of AGCMs, benefits will also follow in the driven LAMs. Increased computer power and capacity, which may probably include massive parallel computers, will make longer model simulations with finer grid resolutions a reality. In the near future it may even be possible to perform two-way nested or variable resolution climate simulations over the entire globe.

CHAPTER 3

SIMULATING CLIMATE WITH THE LIMITED AREA MODEL DARLAM

3.1 INTRODUCTION

The nested model DARLAM has been developed to meet the requirements of both climate simulation experiments and shorter-term mesoscale studies (Walsh and McGregor, 1995). The LAM has evolved during the last decade from the 2-time level semi-Lagrangian model proposed by McGregor (1987). A full set of climate model parameterisations have since been added (McGregor et al., 1993b). DARLAM has been used over many locations with a variety of horizontal and vertical resolutions. The major applications focused on regional climate simulations nested within output fields saved 8-hourly or 12-hourly from the CSIRO9 AGCM.

Many simulations have been performed by nesting DARLAM either within the CSIRO9 AGCM or observational analyses. A one-way nesting technique was employed in all simulations. The earliest simulations were for perpetual January conditions. Subsequently, multiple January and July simulations have been performed followed more recently by full seasonally varying simulations of up to 20 years in duration. The latest regional climate simulations were nested for 140 years within the CSIRO9 AGCM transient simulation. In these simulations the atmospheric equations were integrated forward in time over nine levels in the vertical at both 125 km and 60 km horizontal grid resolutions (McGregor, 1999). The latest version of the model has 18 levels in the vertical with the lowest level at 40 m (McGregor, 1999).

Model simulations for both 1xCO_2 and 2xCO_2 conditions over the Australian and south-east Asian region have been performed at a grid resolution of 125 km. Selected doubly-nested simulations have then been performed at 50 km and 60 km resolution. In most of the experiments the focus was to determine the skill of the model with respect to the simulation of the seasonal cycle of surface air temperature and precipitation. Daily maxima and minima of model simulated surface air temperature have been studied and the simulated representation of the daily range examined.

Prior to the present study, DARLAM has also been successfully applied over New Zealand and South Africa. Good agreement was generally obtained between DARLAM simulations and observed climatologies. These studies revealed that an important aspect that still needs to be addressed is excessive precipitation simulated by DARLAM over regions of steep topography (McGregor, 1999; Joubert et al., 1999).

Tropical domains pose additional difficulties for the one-way nested modelling approach. These difficulties are related to the weaker boundary forcing in such domains and the greater necessity for compatible physical parameterisation schemes (see section 2.3.1). Most climate simulations performed with DARLAM over tropical regions produced acceptable climatologies with somewhat unrealistic annual variability in precipitation patterns (McGregor, 1999).

This chapter commences with a description of both the CSIRO9 AGCM and DARLAM. It is followed by a discussion of nested climate modelling experiments performed with DARLAM over various regions in the world. Emphasis is placed upon the two previous simulations performed over southern Africa. Finally, the crucial role of topography in the DARLAM simulations is discussed.

3.2 THE CSIRO9 AGCM (MARK II VERSION)

The CSIRO9 Mark II AGCM is a 9-level climate model with R21 spectral resolution that utilises an equally spaced east-west grid of 64 and a pole to equator grid of 28 unevenly spaced latitudes per hemisphere. A T63 version of the model is also available. The model utilises a sigma co-ordinate system (σ-system) in the vertical. The model integrates the flux formulation of the primitive equations (Gordon, 1981) forward in time. Unlike the advective formulation (Bourke, 1974) the flux formulation ensures that both energy and mass are conserved during the model integration. These conservation properties are vital when an AGCM is used for the multi-annual integration required for climate simulations. Gordon (1981, 1993) and Rautenbach (1999) provide details concerning the derivation of the model's dynamical equations.

The main prognostic variables are surface-pressure, surface-pressure weighted divergence, surface-pressure weighted vorticity, temperature and moisture. Apart from the moisture, which is a grid variable formulated in terms of a semi-Lagrangian moisture transport scheme (McGregor, 1993), the remaining variables are all spectrally analysed. The main prognostic variables are calculated at full σ-levels in the vertical, while the diagnostics of vertical velocity and geopotential height are derived at half levels.

Time integration is performed by using a semi-implicit Leapfrog scheme where linearised fast moving gravity wave generating terms are used to link the divergence, thermodynamic and surface-pressure equations (Hoskins and Simmons, 1975; Simmons and Hoskins, 1978; McGregor et al., 1993a). This implies that the time step is no longer restricted by gravity wave generating terms and that longer time steps can be used.

The CSIRO9 AGCM simulates a comprehensive range of physical processes including radiation and precipitation, which act as forcing of the dynamical equations. The model is intended for general climate simulation and thus represents full annual and diurnal cycles. The physical parameterisation schemes of the CSIRO9 AGCM include a modified version of the Arakawa (1972) cumulus convection scheme, the Deardorff (1977) soil moisture scheme and the GFDL diurnally-varying parameterisation for longwave and shortwave radiation (Fels and Schwarzkopf, 1975; Schwarzkopf and Fels, 1991). The model also includes a stability-dependent boundary layer based on Monin-Obukhov similarity theory (Louis, 1979). Soil temperatures are calculated using a three-layer model with a zero-flux condition at the bottom. A diagnostic cloud scheme is also included, as well as parameterisation of gravity wave drag (Chouinard et al., 1986).

3.3 DARLAM

DARLAM is a full primitive equations model that uses a Lambert conformal projection. In most experiments with DARLAM, simulations have been performed using the same 9-level vertical structure used for the CSIRO9 AGCM. In the present experiments (discussed in Chapter 5) the nested model uses 18 σ-levels in the vertical. Horizontal grid resolutions in previous experiments performed with DARLAM varied between 15 km and 125 km. In the present experiments a horizontal grid resolution of 60 km is used. The dynamical formulation and current parameterisation schemes of DARLAM are outlined in the following section (obtained from McGregor, 1999).

3.3.1 Dynamical formulation

- DARLAM is a 2-time-level, semi-implicit, hydrostatic primitive equations model.
- DARLAM uses semi-Lagrangian horizontal advection with bi-cubic spatial interpolaton (see Chapter 4 for more details).
- Departure points are derived using the procedure proposed by McGregor (1993). See Chapter 4 for more details.
- Vertical eigenvector decomposition is used, with an isothermal reference profile.
- Helmholtz equations are solved by successive over-relaxation.
- Total variation diminishing (TVD) vertical advection is applied (Thuburn, 1993).
- Winds are staggered on an Arakawa C-grid.
- Treatment of the pressure gradient term is similar to that given in Corby et al. (1972), in which avoids large truncation errors are avoided.

- DARLAM uses a Lambert conformal projection.

- A one-way nesting technique with exponentially decreasing weights is used (Davies (1976) style).

- Multiple nesting options are available.

- A shape-conserving interpolation option is available (Bermejo and Staniforth, 1992).

3.3.2 Physical parameterisation schemes

- DARLAM presently uses an Arakawa/Gordon mass-flux cumulus convection scheme.

- Evaporation of rainfall is included in simulations.

- Tiedtke shallow convection is used.

- GFDL parameterisation for long-wave and short-wave radiation is applied.

- Interactive diagnosed cloud distributions are included.

- Gravity wave drag options are available.

- Stability-dependant boundary layer and vertical mixing (Louis (1979) style) are included.

- The vegetation/canopy scheme includes:
    - six layers for soil temperatures
    - six layers for soil moisture (Richards' equation)

- Diurnally varying skin temperatures for SSTs are included.

- An option for cumulus mixing of trace gasses exists.

DARLAM incorporates a set of physical parameterisation schemes that are similar to those used in the CSIRO9 AGCM (described in section 3.2). The surface fluxes are calculated with a modified Louis (1979) parameterisation. The roughness length over land is 0.16m, while Charnock's (1955) formulation is used over the ocean with a parameter value of 0.018.

There are however some differences between the parameterisation schemes used in the two models. In some experiments with DARLAM (Walsh and McGregor, 1995, 1997a) a modified Kuo (1974) convection scheme was used in the nested model and gravity wave drag was excluded. Sensitivity experiments indicated that DARLAM results were not severely affected by differences in the convection parameterisation (note that the CSIRO9 AGCM uses a version of the Arakawa (1972) convection scheme). In previous simulations with DARLAM over South Africa, Joubert et al. (1998, 1999) used a modified version of the Arakawa (1972) convection scheme. Here it was mentioned that several other convection schemes have been tested in earlier unpublished sensitivity tests but that the Arakawa (1972) scheme outperformed the others in numerous single-month sensitivity tests. In these experiments enhanced surface drag parameterisation has been included near mountainous terrain to account for subrid-scale topographic drag. Further details of the parameterisation and vertical mixing schemes are outlined in McGregor et al. (1993a). Different methods for determining soil moisture (Kondo et al., 1990) is used in monthly climate simulations with the two models (see section 2.8). These methods are known as the α-method (DARLAM) and β-method (CSIRO9 AGCM).

Vegetation data includes soil and vegetation types as well as the associated physical characteristics. Albedo fields have been derived from data produced by the Simple Biosphere model (SiB) (Dorman and Sellers, 1989). These fields are used in the surface canopy scheme of Kowalczyk et al. (1994). The US Navy 5' topography fields were aggregated to model grid resolution to produce surface elevation fields.

3.4 THE NESTING TECHNIQUE

In experiments performed with DARLAM (see section 3.5 for more details) a one-way nesting technique was followed, with boundary conditions specified from the CSIRO9 AGCM or observational analyses. At each time-step the outermost boundary rows of DARLAM are relaxed towards the interpolated values supplied every 8 or 12 hours by the CSIRO9 AGCM. A modified Davies (1976) scheme with exponentially decreasing weights as proposed by Giorgi et al. (1994) was used. At each time step, the contribution of the forcing boundary conditions decreases exponentially to below five percent at five grid-points inside the outer boundary. For MSLP and temperature the boundary fields are altered to compensate for any differences that might arise in elevation fields as a result of diverse model topographic features (DARLAM vs CSIRO9 AGCM).

3.5 PREVIOUS EXPERIMENTS PERFORMED WITH DARLAM

3.5.1 INTERNATIONAL EXPERIMENTS

CSIRO scientists (McGregor, Katzfey and Walsh) have performed most limited-area climate modelling experiments with DARLAM over the Australian region. At higher latitudes the nested climatologies produced are generally superior to those produced by the forcing AGCMs and compare reasonably well to regional observations over the Australian continent (Walsh and McGregor, 1995).

The first experiment performed with DARLAM was for perpetual January conditions (McGregor and Walsh, 1991, 1993). In an effort to simulate the climate of a domain encompassing Australia for perpetual January conditions DARLAM has been nested at grid resolutions of 250 and 125 km within a version of the Australian Bureau of Meteorology Research Centre's AGCM. The experiments indicated significant improvements in LAM precipitation patterns over that of the AGCM. Another finding was that tropical region topography near the boundary of the domain requires careful treatment (McGregor and Walsh, 1991, 1993).

A 60 km resolution DARLAM simulation has been nested within another DARLAM simulation at a resolution of 125 km to investigate the impacts of the enhanced greenhouse effect on the climate of Tasmania (McGregor and Walsh; 1994). This doubly-nested simulation within the CSIRO9 AGCM generated significantly improved regional climate detail for Tasmania.

These experiments were followed by high-resolution climate simulations for January and July over the Australian region (Walsh and McGregor,1995). They one-way nested DARLAM at a resolution of 125 km within the CSIRO9 AGCM. One new aspect of these simulations was that the model domain extended to tropical regions both north and south of the equator. The size of the domain was also considerably larger than those used in previous experiments. Ten separate 30-day simulations have been performed for January as well as July. Ensemble averages of the ten January and July simulations have been used as the model climatology. The 30-day simulations incorporated both diurnally and seasonally varying radiation but were initialised separately from CSIRO9 AGCM output fields. No vertical mode initialisation was performed. A short spin-up period of approximately two days allowed for the DARLAM moisture cycle to reach equilibrium. DARLAM results indicated improvements in simulations away from the model boundaries. DARLAM simulations were also closer to reality over sub-tropical and mid-latitude regions. The improvement appeared to be the greatest in mid-latitudes over land.

The latter DARLAM simulations showed a general improvement in the simulation of precipitation when compared to the AGCM. This result, along with improved results obtained for screen temperatures, may be attributed to more detail in the DARLAM topography (Walsh and McGregor, 1995). Biases relative to observations in the DARLAM simulations pointed out that the general overestimation of rainfall is a problem that occurs in regions of steep topography. Over the ocean the simulation of precipitation by the CSIRO9 AGCM and DARLAM was of comparable quality (Walsh and McGregor, 1995).

A follow up ensemble of 10-year runs was carried out in both seasonal and multi-month mode (see section 2.8). These runs showed that the multi-month approach reproduces climatologies almost as well as the seasonally varying runs, provided that care is taken with the initialisation of soil variables (McGregor, 1997a).

DARLAM has been used by Renwick et al. (1997) for 50 km doubly-nested simulations over New-Zealand. The study showed significant improvements in precipitation patterns near topography or coastal features. There is, however, a tendency for excessive precipitation on the highest peaks. Extreme precipitation over New Zealand was modelled at 15 km resolution by Katzfey (1995).

Finally, the nested model has been applied over Antartica (Walsh and McGregor, 1996) and for studying inter-annual variability (Walsh and McGregor, 1997a). It has also been used to simulate the transport of greenhouse gasses and the characteristics of their sources and sinks (McGregor, 1997a).

3.5.2 EXPERIMENTS PERFORMED OVER SOUTHERN AFRICA

To date, only two NCM experiments have been performed over southern Africa. Joubert et al. (1998) used DARLAM to simulate January climate over the region. January was used to represent mid-summer (austral summer) conditions, given that most of the region experiences a pronounced summer rainfall maximum (Tyson, 1986). Using a one-way nesting procedure, lateral boundary and initial conditions were supplied by the CSIRO9 AGCM. The experiment consisted of twenty January ensemble members nested individually at 125 km resolution within the CSIRO9 AGCM.

The model simulation showed that DARLAM results are generally better than those of the CSIRO9 AGCM. The MSLP distribution simulated by DARLAM is more accurate over land masses than in the AGCM simulation. Throughout the troposphere DARLAM winds prove to be better than CSIRO9 AGCM wind simulations. Analysis of lower level wind patterns revealed that the CSIRO9 AGCM does not capture the observed low-level convergence in the vicinity of Mozambique. DARLAM noticeably improves on the latter flow deficiency, probably because of its more adequate representation of the topography of Madagascar (Joubert et al., 1998). It therefore seems essential that when designing LAM experiments over Southern Africa, Madagascar should be included in the model domain. Furthermore, it may prove worthwhile to choose the eastern boundary of the model domain as far away from Madagascar as possible.

Joubert et al. (1998) found that DARLAM captures the spatial pattern of observed rainfall and inter-annual rainfall variability over the region as a whole more accurately than the AGCM. Over most parts of the subcontinent, inter-annual variability in the DARLAM simulation is not significantly different from observations. Over the steep escarpment along the south-eastern coastline of South Africa, DARLAM simulates more rainfall than the AGCM and significantly more rainfall than observed. Inter-annual variability of rainfall over this region however, was not significantly different from the associated observed inter-annual variability. Over Madagascar, DARLAM simulates more rainfall than the AGCM, but less than observed. Here the simulated inter-annual variability is also significantly less than observed.

Joubert et al. (1998) concluded that DARLAM provides a more accurate and detailed simulation of the January climate over Southern Africa than the CSIRO AGCM. This is largely due to the fact that regional topographical features which influence the southern African climate are more clearly resolved by the 125 km LAM resolution (Joubert et al., 1998).

In the second nested climate modelling experiment over southern Africa Joubert et al. (1999) used DARLAM to simulate the full seasonal cycle in a 10-year simulation using present-day atmospheric CO_2 concentrations. The model's ability to simulate daily rainfall statistics during January was assessed. The NCM was one-way nested within the CSIRO9 AGCM. Again it was found that DARLAM simulates too much rain and too many rain days over the eastern parts of South Africa. The probability of occurrence of rainfall events of a given magnitude (expressed as the frequency of occurrence / total number of rain events*100) is largely similar to observations. However, the fact that the model simulates up to three times the observed number of rain days in January resulted in an overestimation of total rainfall. (Joubert et al., 1999).

Above average model simulated rainfall over the escarpment is associated with anticyclone ridging to the south of the subcontinent, which extends through the troposphere to the 500hPa level (Joubert et al.,1999). It is worth noting that observed extreme rainfall events are often associated with a similar circulation pattern, suggesting that DARLAM reliably reproduces the circulation responses associated with above-average rainfall (Joubert et al., 1999). In the DARLAM simulations, stronger than normal (compared to the nested model's climate) anticyclonic circulation is associated with above average moisture content, particularly in the zone of convergence on the leading edge of the ridging anticyclone (Joubert et al., 1999). In the immediate vicinity of the escarpment, simulations of anomalous onshore or upslope flow results in simulated upward motion indicating that the correct set of conditions for rainfall is produced (Joubert et al., 1999). While these results indicate sound physical reasons for rainfall to occur they do not explain why the daily rainfall statistics (both number of rain days and observed rainfall) are so much higher than observed (Joubert et al., 1999). One possible cause for this overestimation relates to a known problem concerning the representation of flow around steep orographic barriers (discussed in section 3.6). Despite problems experienced by Joubert et al. (1999) in the rainfall simulation, it was concluded that DARLAM results show a marked improvement in the simulation of southern African climate detail relative to the CSIRO9 AGCM.

3.6 THE ROLE OF TOPOGRAPHY IN DARLAM SIMULATIONS

Steep topography may lead to excessive accumulated topographic precipitation (Giorgi et al., 1994; McGregor and Walsh, 1994; Jones et al., 1995). This problem is more evident at higher model resolution but is probably not specific to LAMs (McGregor, 1997a). The reason for this is still not fully understood but for DARLAM the excess precipitation occurs at resolved scales and therefore is probably related to the model's mountain wave response (McGregor, 1997a). Horel et al. (1994) however, attribute excessive simulated 5-day rainfall over the Andes to dynamical effects of the Kuo cumulus parameterisation scheme.

A second unsolved (but closely related) problem in nested climate modelling is the fact that LAMs tend to simulate too many rain days (compared to observations) as well as lower than observed rainfall intensities (rain per rain day) in regions of steep topography. This result has been noticed using different climate models (Jenkins and Barron, 1997; Walsh and McGregor, 1995; McGregor and Walsh, 1994; Giorgi et al., 1994).

The steep eastern escarpment of southern Africa contributes to the problem of excessive simulations of rainfall over regions of steep topography by LAMs. Evidence provided by Joubert et al. (1998) suggests that DARLAM simulates too much moisture over the eastern escarpment of South Africa. Over steep topography such as the eastern escarpment of South Africa and eastern Madagascar DARLAM simulates in excess of twice as much daily rainfall as is observed. The lower-tropospheric flow over the escarpment during rain events is upslope (perpendicular to the obstacle) as surface moisture is advected onshore around a ridging anticyclone (Joubert et al., 1998). It is speculated that DARLAM's semi-implicit, semi-Lagrangian scheme over-estimates vertical velocities over steep topographic gradients due to the semi-Lagrangian mountain resonance effect (Joubert et al., 1999). In essence, the very steep topography of south-eastern Southern Africa is difficult to reproduce in semi-Lagrangian regional model formulations (Joubert et al., 1998, 1999). This may be a reason for rainfall over-estimation along the southern escarpment. These results also indicate that improvements in the simulation of regional rainfall totals will only follow from further development of the regional model itself (Joubert et al., 1999).

McGregor (1997a) points out that various models use one or more of the following methods to ameliorate the problem. These methods include a filter of the topography, time averaging of latent heat (Giorgi, 1991) and the use of different precipitation triggers from the AGCM. Some models (Giorgi et al., 1993a, Walsh and McGregor, 1995) also reduce the horizontal diffusion near topography in order to reduce spurious vertical redistribution of moisture related to the use of terrain-following co-ordinates. Leung et al. (1996) report benefits from using a new subgrid parameterisation for topographic parameterisation.

The mountain wave response problem in DARLAM is probably related to the semi-Lagrangian technique used in the model to discretirise the total derivatives in the governing equations. Semi-Lagrangian treatment of advection improves model efficiency by permitting larger time steps than those allowed by Eulerian schemes (see Chapter 4). In order to remain stable, Eulerian time schemes must satisfy the Courant-Friedrichs-Lewy (CFL) criterion that restricts the size of the time step allowed to use for a given spatial resolution and advecting wind. However, it has been known for some time that there is a problem incorporating stationary orographic forcing into models using semi-Lagrangian techniques.

Coiffier et al. (1987) showed that semi-Lagrangian methods lead to wrong stationary solutions for Courant numbers greater than unity in the context of a three-time level linear baroclinic model and therefore suggested that the time-step advantage of semi-Lagrangian schemes vanishes in the presence of topography. In their review paper, Staniforth and Côté (1991) identified the need for further research on the incorporation of stationary forcing in semi-Lagrangian models in a way that does not limit the Courant number. This approach was reiterated by Tanguay et al. (1992). Kaas (1987) proposed solving this problem by spatially averaging the forcing along a directory and Tanguay et al (1992) have examined the effects of the solution proposed by Kaas (1987) in controlled experiments. They demonstrated that spatial averaging considerably reduces the level of spurious noise in the vicinity of the North American Rockies for integrations of both global spectral and regional finite difference models. The analysis however, indicates that although spatial averaging alleviates the problem, it is not eliminated.

Rivest and Staniforth (1994) examined the problem in the context of the shallow-water equations. Using a simple one-dimensional model, the source of the problem has clearly been shown to be spurious numerical resonance induced by the semi-Lagrangian semi-implicit discretization in the presence of topographic forcing. They found that simply off centring the semi-implicit scheme eliminates the spurious resonance. This can be achieved with a second order accurate (in time) scheme without loss of accuracy. Only 48-hour forecasts obtained from a global shallow-water model were evaluated however, and issues pertinent to longer time integrations such as mass conservation were not addressed in the study. The solution advocated by Rivest and Staniforth (1994) was subsequently included in the thermodynamic and momentum equations of some versions of the DARLAM code. The effectiveness of the solution over the steep south-eastern escarpment of South Africa remains to be illustrated.

CHAPTER 4

THE MULTIPLY-UPSTREAM SEMI-LAGRANGIAN METHOD OF SIMULATING ADVECTION

4.1 INTRODUCTION

Analytic and numerical solutions of the Eulerian equations of hydrodynamics are limited in extent by the non-linear advection, or transport terms. Analytic solutions are difficult to obtain because the advection terms render the equations non-linear. Finite difference numerical solutions are readily derived in principle but are inaccurate because finite difference approximations of the advection terms can introduce errors in phase and amplitude (Crowley, 1968; Mesinger and Arakawa, 1976). In order to remain stable, Eulerian time schemes must satisfy the Courant-Friedrichs-Lewy (CFL) criterion that restricts the size of the time step used for a given spatial resolution and advecting wind.

A Lagrangian approach to solving the equations of fluid motion involves following a fixed set of particles throughout the period of integration. However, Welander (1955) indicated that, in general, a set of fluid particles which are initially regularly distributed soon become significantly deformed and are therefore rendered unsuitable for numerical integration. To avoid this difficulty, while still concentrating on fluid particles, Wiin-Nielsen (1959) introduced a semi-Lagrangian approach, whereby a set of particles which arrive at a regular set of grid points are traced back over a single time interval to the location of the initial departure points. The values of the dynamical quantities at the departure points are obtained by interpolation from neighbouring grid points with known values. The semi-Lagrangian approach differs from the Lagrangian approach because in the former the set of particles in question changes at each time step.

In multiply-upstream semi-Lagrangian schemes the grid points used for interpolation to the departure point of a particle are selected in such a way that they always surround the departure point. When the winds are strong the set of grid points may be many grid intervals upstream from the arrival grid point. The term “multiply-upstream” is used to describe a scheme using interpolation points selected in this way (Bates and McDonald, 1982).

During the last fifteen years there has been an increased interest in semi-Lagrangian techniques to manipulate horizontal or vertical advection in numerical prediction models. The essential feature of such schemes is that the total or material derivatives in the equations of motion are treated directly by calculating the departure points of fluid parcels. The upstream value of the required fields are then usually evaluated by spatial interpolation (McGregor, 1993). The main advantage of semi-Lagrangian techniques is that it allows for the relaxation of the CFL criterion. The popularity of the semi-Lagrangian approach stems however not only from the large permissible time steps but also from the high degree of advection accuracy. The schemes may be either two-time level or three-time level.

This chapter deals with the semi-Lagrangian method of numerically modelling the advective process. The goal is to clarify and elaborate upon some of the theoretical issues of semi-Lagrangian advection and to compare the semi-Lagranian scheme used in DARLAM to well-tested Eulerian schemes in order to evaluate their relative merits with respect to stability and accuracy.

4.2 THE ADVECTION EQUATION

In order to examine the properties of numerical advection schemes, numerical approximations to the two–dimensional advection equation in Cartesian co-ordinates will be analysed. The horizontal (two-dimensional) *non-linear* advection equation may be expressed as:

$$\frac{\partial\psi}{\partial t}+u\frac{\partial\psi}{\partial x}+v\frac{\partial\psi}{\partial y}=0 \qquad \textbf{(4.1)}$$

Here $u=u(x,y,t)$ and $v=v(x,y,t)$ are the advection velocity components in the x and y directions respectively and t is time. The dependant variable $\psi=\psi(x,y,t)$ is some property (for example non-diffusive moisture) of the fluid that is transported by the flow field, so that its total derivative along an instantaneous streamline is zero. That is, equation **(4.1)** when written with respect to an observer who moves with the fluid simplifies to

$$\frac{d\psi}{dt}=0\,,\ \ \psi=\psi(x_0,y_0,t_0)$$

so that an observer will measure no change in ψ as time passes. Equation **(4.1)**, also called the colour equation, is considered in practise to be the most important part of the atmospheric governing equations (Mesinger and Arakawa, 1976).

The *linear* two-dimensional advection equation is

$$\frac{\partial\psi}{\partial t}+u\frac{\partial\psi}{\partial x}+v\frac{\partial\psi}{\partial y}=0\,; \qquad u,\ v \text{ constant} \qquad \textbf{(4.2)}$$

The *non-linear* advection equation in one space dimension is

$$\frac{\partial\psi}{\partial t}+u\frac{\partial\psi}{\partial x}=0 \qquad \textbf{(4.3)}$$

where $\psi=\psi(x,t)$ and $u=u(x,t)$, while the *linear* advection equation in one space dimension is

$$\frac{\partial \psi}{\partial t}+u\frac{\partial \psi}{\partial x}=0; \qquad \text{u constant} \tag{4.4}$$

Equation **(4.4)** describes the simplest advective processes and has proved to be a useful framework for the evaluation and comparison of numerical integration schemes.

Before investigating the properties of numerical solutions of the non-linear advection equation **(4.1)** it is useful to first obtain an analytical solution of the linear two-dimensional advection equation **(4.2)** in the form of a single harmonic

$$\psi(x,y,t)=\mathrm{Re}\left\{\Psi(t)e^{I(kx+ly)}\right\} \tag{4.5}$$

Here $\Psi(t)$ is the wave amplitude, and k and l are wave numbers in the x and y directions respectively. $k=\frac{2\pi}{L_x}$ and $l=\frac{2\pi}{L_y}$ with L_x and L_y the wavelengths in the x and y directions respectively. The imaginary number I is defined as $I^2 \equiv -1$.

Substituting equation **(4.5)** into the linear advection equation **(4.2)** gives

$$\frac{d\Psi}{dt}+Iku\Psi+Ilv\Psi=0 \tag{4.6}$$

Thus, the problem of solving the partial differential equation **(4.2)** has been reduced to that of solving an ordinary differential equation **(4.6)** with the following solution:

$$\Psi(t)=\Psi(0)e^{-I(ku+lv)t} \tag{4.7}$$

$\Psi(0)$ denotes the initial value of the amplitude. Hence, the desired harmonic solution is

$$\psi(x,y,t)=\mathrm{Re}\left\{\Psi(0)e^{Ik(x-ut)+Il(y-vt)}\right\} \tag{4.8}$$

Each wave component is advected at a constant velocity of $c=\sqrt{u^2+v^2}$ in the x-y plane, with no changes in amplitude. Important features in the assessment of a numerical integration scheme are therefore the damping (if any) and the phase speed of a single harmonic.

The one-dimensional linear advection equation **(4.4)** also has a solutions in the form of a single harmonic component,

$$\psi(x,t)=\mathrm{Re}\left\{\Psi(t)e^{Ikx}\right\}$$

provided that

$$\frac{d\Psi}{dt} + Iku = 0 . \tag{4.9}$$

The solution of equation **(4.9)** is

$$\Psi(t) = \Psi(0)e^{-Ikut} \tag{4.10}$$

or, for discrete values $t = n\Delta t$ (n is the number of time steps and Δt the time interval),

$$\Psi^n = \Psi(n\Delta t) = \Psi(0)e^{-Ikun\Delta t} \tag{4.11}$$

where $\Psi(0)$ is the initial value of the amplitude. In equation **(4.11)** $\omega = -ku\Delta t$ represents the change in argument (or phase change) of the **(4.11)** in a single time step Δt. This will obviously also be the phase change in time of the true solution of the linear one-dimensional advection equation.

4.3 EULERIAN SCHEMES TO SOLVE THE ADVECTION EQUATION

In this section some well-tested Eulerian schemes to solve the advection equation are formulated and their accuracy and stability properties are discussed.

4.3.1 LEAPFROG SCHEME

4.3.1.1 Construction of the leapfrog scheme

One of the most widely used numerical schemes to solve the advection equation is the leapfrog scheme. The scheme is obtained by replacing both the time and space derivatives in the advection equation by centred (second order accurate) finite difference approximations. The scheme is a three-level scheme, meaning that it relates the values of the dependant variable at three time levels.

Approximating the space derivatives in the two-dimensional linear advection equation **(4.2)** with standard second order accurate difference quotients (Mesinger and Arakawa, 1976) results in

$$\frac{\partial \psi_{i,j}}{\partial t} = -u\frac{\psi_{i+1,j} - \psi_{i-1,j}}{2\Delta x} - v\frac{\psi_{i,j+1} - \psi_{i,j-1}}{2\Delta y} . \tag{4.12}$$

The co-ordinates of grid point (i,j) are given by $x = i\Delta x$ and $y = j\Delta y$ with Δx and Δy the spatial increments in the x and y directions respectively.

Approximate values for $\psi(i\Delta x, j\Delta y)$ are denoted by $\psi_{i,j}$. Centred differences are used for the time derivative, resulting in the following equation:

$$\psi_{i,j,k+1} = \psi_{i,j,k-1} - \Delta t\left[u\frac{\psi_{i+1,j,k} - \psi_{i-1,j,k}}{\Delta x} + v\frac{\psi_{i,j+1,k} - \psi_{i,j-1,k}}{\Delta y}\right] \qquad \textbf{(4.13)}$$

The points in time where the numerical solution is computed for equation **(4.2)** are given by $t = k\Delta t$, with $k \geq 2$. The solution for time step $t = 1.\Delta t$ is approximated by using backward time differencing:

$$\psi_{i,j,1} = \psi_{i,j,0} - \Delta t\left[u\frac{\psi_{i+1,j,,0} - \psi_{i-1,j,0}}{2\Delta x} + v\frac{\psi_{i,j+1,0} - \psi_{i,j-1,0}}{2\Delta y}\right]. \qquad \textbf{(4.14)}$$

4.3.1.2 Amplitude accuracy

It is instructive to investigate the amplitude and phase properties of numerical solutions from the linear advection equation **(4.2)**. Von Neumann's, or the Fourier series method (Mesinger and Arakawa, 1976), is employed for this purpose. A solution of the linear advection equation can be expressed in the form of a Fourier series, where each harmonic component is also a solution (Mesinger and Arakawa, 1976). The stability of a single harmonic may be tested and stability of all admissible harmonics then constitutes a necessary condition for stability of the scheme (Mesinger and Arakawa, 1976).

It is worthwhile to note that when using a grid point method to numerically solve partial differential equations with wave-type solutions, it is impossible to resolve waves with wavelengths shorter than $\min\{2\Delta x, 2\Delta y\}$ (Mesinger and Arakawa, 1976).

Returning to the von Neumann method, a solution of the finite difference equation **(4.13)** can be derived by substituting a solution of the following form of a single harmonic into equation **(4.12)**:

$$\psi_{i,j}^{n} = \mathrm{Re}\left\{\Psi^{n} e^{I(ki\Delta x + lj\Delta y)}\right\} \qquad \textbf{(4.15)}$$

This is analogue to solution **(4.8)** of the linear advection equation at discrete points $i\Delta x$, $j\Delta y$ and $n\Delta t$. Here Ψ^{n} represents the amplitude of the numerical solution at time level n. After some rearrangement, it follows that the single harmonic **(4.15)** is a solution of equation **(4.12)** provided that

$$\frac{d\Psi}{dt} = I\left(-\frac{u}{\Delta x}\sin k\Delta x - \frac{v}{\Delta y}\sin l\Delta y\right)\Psi \qquad \textbf{(4.16)}$$

Approximating the time derivative in **(4.12)** with centred differences yields

$$\Psi^{n+1} = \Psi^{n-1} + 2I\left(-u\frac{\Delta t}{\Delta x}\sin k\Delta x - v\frac{\Delta t}{\Delta y}\sin l\Delta y\right)\Psi^{n} \qquad \textbf{(4.17)}$$

Equation **(4.17)** enables analyses explaining the behaviour of the amplitude Ψ^n with an increase in time step (n). The amplification factor $|\lambda|$ is defined as

$$\Psi^{n+1} \equiv \lambda\Psi^{n} \qquad \textbf{(4.18)}$$

Taking the absolute value on both sides yields

$$\left|\Psi^{n+1}\right| = |\lambda|\left|\Psi^{n}\right|$$

For the stability of each harmonic solution **(4.15)**, it is required that

$$\left|\Psi^{n}\right| = |\lambda|^{n}\left|\Psi^{0}\right| < B$$

where B is a finite number. Taking the logarithm on both sides yields:

$$n\ln|\lambda| < B' \quad \text{where} \quad B' \equiv \ln\left(\frac{B}{\left|\Psi^{0}\right|}\right)$$

Thus, B' is a new constant. Since $t = n\Delta t$, the necessary condition for stability becomes

$$\ln|\lambda| < \frac{B'}{t}\Delta t \qquad \textbf{(4.19)}$$

Suppose that boundedness of the solution is required for a finite time t.

Condition **(4.19)** can then be written as

$$\ln|\lambda| \le O(\Delta t)$$

Defining $|\lambda| \equiv 1+\delta$ and in view of the power series expansion

$$\ln(1+\delta) = \sum_{n=0}^{\infty}\frac{(-1)^{n}}{n+1}\delta^{n+1} \quad \text{for} \quad -1<\delta<1$$

(Ellis and Gulick, 1994) it follows that the stability condition obtained is equivalent to

$$\delta \le O(\Delta t)$$

or

$$\frac{d|\lambda_1|}{dp} = 1 + \frac{p}{\sqrt{p^2 - 1}}$$

which is unbounded if $p \to 1$

From equation **(4.21)** follows that the stability criterion $|p| \leq 1$ has to be written as

$$\left| u\frac{\Delta t}{\Delta x}\sin k\Delta x + v\frac{\Delta t}{\Delta y}\sin l\Delta y \right| \leq 1$$

This must be true for all resolvable wavelengths, which are all admissible values of the wave numbers k and l. If only the cases where $\Delta x = \Delta y$ is considered, the condition simplifies to

$$c\frac{\Delta t}{\Delta x}\sqrt{(\sin k\Delta x)^2 + (\sin l\Delta x)^2} \leq 1$$

where $c = \sqrt{u^2 + v^2}$. Mesinger and Arakawa (1976) showed that the case where $\sin k\Delta x$ = $\sin l\Delta x$ = 1 does occur within the admissible range of wave numbers. Thus, if the two-dimensional linear advection equation **(4.2)** is approximated using the leapfrog finite difference scheme, the amplitude of a solution in the form of a single harmonic component will remain bounded if

$$c\frac{\Delta t}{\Delta x}\sqrt{2} \leq 1 \qquad \textbf{(4.23)}$$

This constitutes a necessary condition for the stability of the scheme and is commonly known as the CFL criterion.

4.3.1.3 Phase accuracy

In this section the phase properties of the leapfrog scheme is investigated by considering approximations to the solution of the less complex one-dimensional linear advection equation **(4.4)**. The von Neumann method involves defining the amplification factor λ as

$$\Psi^{n+1} \equiv \lambda \Psi^n$$

(equation **(4.18)**). λ can be written as

$$\lambda = |\lambda| e^{I\theta} \qquad \textbf{(4.24)}$$

Equation **(4.18)** and **(4.24)** yields that the amplitude of the numerical solution at any time step is given by (Mesinger and Arakawa, 1976)

$$\Psi^n = |\lambda|^n \Psi^0 e^{In\theta}$$

Comparing this with equation **(4.11)** reveals that θ represents the change in argument (phase change) the numerical solution at each time step (Mesinger and Arakawa, 1976).

It is of interest to consider the phase change of the numerical solution per time step (θ) relative to that of the true solution ($\omega = -ku\Delta t$) namely

$$R = \frac{\theta}{\omega}$$

If the phase change of the numerical solution (θ) per time step is equal to that of the true solution (ω), the relative phase change (R) is unity. However, an expression for the phase change (θ) of the numerical solution first needs to be derived. Using the notation (following Mesinger and Arakawa (1976))

$$\lambda \equiv \lambda_{re} + I\lambda_{im}$$

it follows from equation **(4.24)** that

$$\tan\theta = \frac{\lambda_{im}}{\lambda_{re}} \qquad \textbf{(4.25)}$$

or

$$R = \frac{1}{\omega}\tan^{-1}\left(\frac{\lambda_{im}}{\lambda_{re}}\right). \qquad \textbf{(4.26)}$$

It has been shown in section 4.3.1.2 that the leapfrog scheme is stable if $p \leq 1$ for the linear two-dimensional advection equation **(4.2)**. The same condition applies when solving the linear one-dimensional equation **(4.4)** with the leapfrog scheme, but now $p = -u\frac{\Delta t}{\Delta x}\sin k\Delta x$. Substituting the two solutions for (λ) from equation **(4.22)** into equation **(4.26)**, indicates that the relative phase change of the leapfrog scheme is

$$R_1 = \frac{1}{\omega}\tan^{-1}\left(\frac{p}{\sqrt{1-p^2}}\right)$$

$$R_2 = \frac{1}{\omega}\tan^{-1}\left(\frac{-p}{\sqrt{1-p^2}}\right)$$

with the condition that $|p| < 1$ with $p = -u\frac{\Delta t}{\Delta x}\sin k\Delta x$ for the one-dimensional linear advection equation (compare this to equation **(4.21)**).

For $|p| = 1$ it follows from equation **(4.22)** that $\lambda_1 = \lambda_2 = Ip$, implying that both values of λ have imaginary parts only. Equation **(4.24)** yields, for $p = \pm 1$, that

$$R_1 = R_2 = \pm\frac{\pi}{2\omega}$$

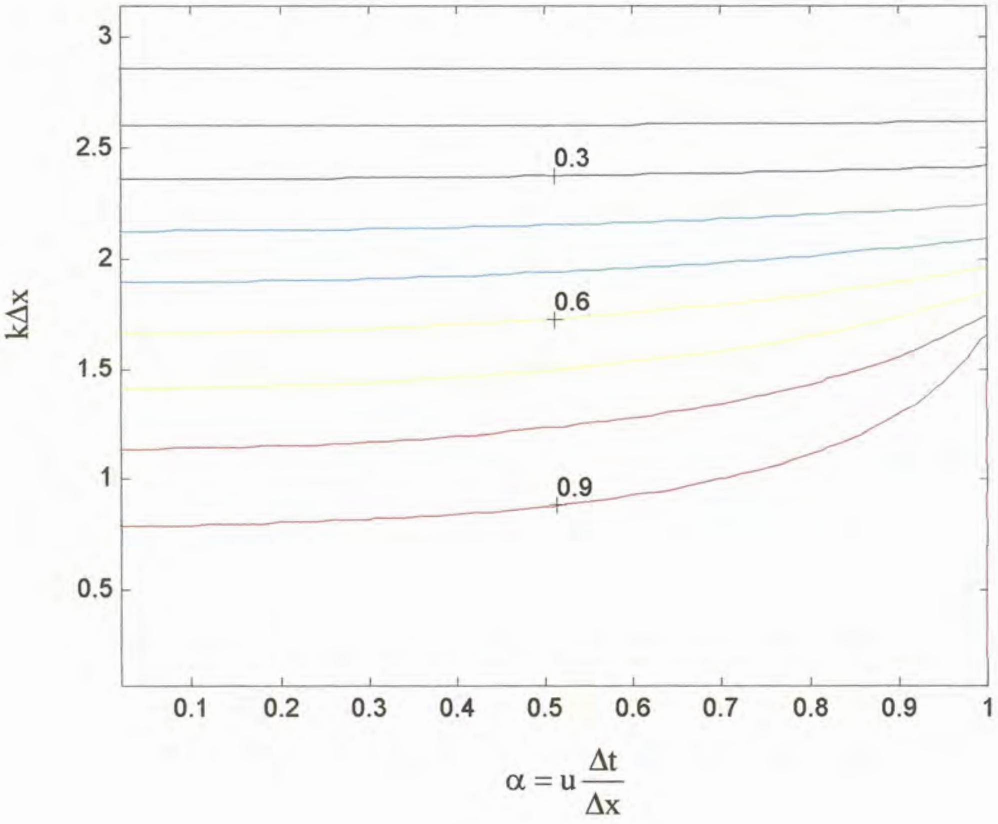

Figure 4.1 Relative phase speed isolines plotted as a function of $k\Delta x$ and α for the physical mode of the leapfrog scheme.

Relative phase speed isolines (R) are plotted in figure 4.1 for the physical mode for $0 \le k\Delta x \le \pi$ (admissible wave numbers) and $0 < \alpha = u\frac{\Delta t}{\Delta x} \le 1$ ($u\frac{\Delta t}{\Delta x} \le 1$ is the one-dimensional CFL criterion – analogue to equation **(4.23)**).

It is obvious that the physical mode is decelerating $(R<1)$ and that the deceleration increases as the wave number (k) increases. Also, the deceleration increases as α decreases. The relative phase speed of the computational mode is the same in magnitude as found for the physical mode but opposite in sign.

4.3.2 LAX-WENDROFF SCHEMES

4.3.2.1 Construction of the Lax-Wendroff and modified Lax-Wendroff schemes

Lax and Wendroff (1960) described an alternative finite difference method, which has since attracted considerable attention. For the linear two-dimensional advection equation **(4.2)** the Lax-Wendroff scheme is implemented as follows:

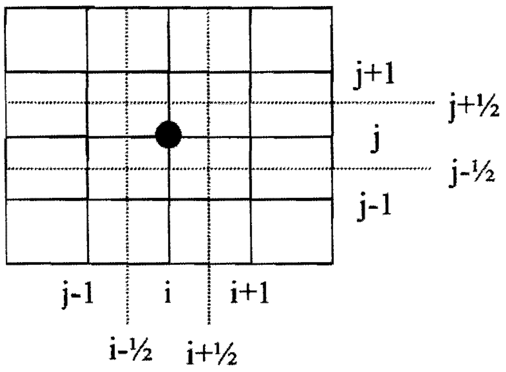

Figure 4.2 Grid configuration for the Lax-Wendrof scheme. The horizontal increment is Δx and the vertical increment is Δy.

Suppose the value of the dependant variable ψ needs to be updated at all grid points $(i\Delta x, j\Delta y)$ (circle in figure 4.2). First, provisional values for ψ at time step $n+\frac{1}{2}$ are calculated for all the "half points" at positions (x, y) with $x = \pm\left(i+\frac{1}{2}\right)\Delta x$ and $y = \pm\left(j+\frac{1}{2}\right)\Delta y$ (where the dotted lines cross in figure 4.2).

This is achieved by applying the following finite difference equation to each of the "half points":

$$\psi^{n+\frac{1}{2}} = \left(\psi^{xy}\right)^n - \frac{1}{2}\left\{\alpha_1\left(\delta_x\psi^y\right)^n + \alpha_2\left(\delta_y\psi^x\right)^n\right\} \qquad \textbf{(4.27)}$$

Equation **(4.27)** employs centred space (equations **(4.30a)** and **(4.30b)** with $m = 1$) and forward time differencing. α_1 and α_2 are given by **(4.31)**. It is necessary to take arithmetic averages in space when calculating the centred space differences (equations **(4.30a)** and **(4.30b)**) and when calculating ψ^n at a particular half point (equation **(4.29)**). Note that the "half points" used at time step $n+½$ are spatially staggered.

Using these provisional values a second step is taken, centred in both space and time, to update the values of the dependant variable (at time step $n+1$) at all grid points $x = i\Delta x$ and $y = j\Delta y$ (circle in figure 4.2):

$$\psi^{n+1} = \psi^{n} - \left\{ \alpha_1 \left(\delta_x \psi^y\right)^{n+\frac{1}{2}} + \alpha_2 \left(\delta_y \psi^x\right)^{n+\frac{1}{2}} \right\} \tag{4.28}$$

Note that

$$\left(\psi^{xy}\right)^n = \frac{\psi^n_{i-\frac{1}{2},j-\frac{1}{2}} + \psi^n_{i-\frac{1}{2},j+\frac{1}{2}} + \psi^n_{i+\frac{1}{2},j-\frac{1}{2}} + \psi^n_{i+\frac{1}{2},j+\frac{1}{2}}}{4}, \tag{4.29}$$

$$\left(\delta_{mx} \psi^y\right)^n = \frac{\psi^n_{i+\frac{m}{2},j+\frac{1}{2}} + \psi^n_{i+\frac{m}{2},j-\frac{1}{2}}}{2m} - \frac{\psi^n_{i-\frac{m}{2},j+\frac{1}{2}} + \psi^n_{i-\frac{m}{2},j-\frac{1}{2}}}{2m} \tag{4.30a}$$

$$\left(\delta_{my} \psi^x\right)^n = \frac{\psi^n_{i+\frac{1}{2},j+\frac{m}{2}} + \psi^n_{i-\frac{1}{2},j+\frac{m}{2}}}{2m} - \frac{\psi^n_{i+\frac{1}{2},j-\frac{m}{2}} + \psi^n_{i-\frac{1}{2},j-\frac{m}{2}}}{2m} \tag{4.30b}$$

$$\alpha_1 = u\frac{\Delta t}{\Delta x} \quad \text{and} \quad \alpha_2 = v\frac{\Delta t}{\Delta y} \tag{4.31}$$

Equations (4.27) to (4.31) constitute the Lax-Wendroff scheme. Note again that $m=1$ when using equations **(4.30a)** and **(4.30b)**. Similar to the leapfrog scheme, the Lax-Wendroff scheme is second-order-accurate in space and time (Gadd, 1978a). The Lax-Wendroff scheme is, however, a two-level scheme (involving only time steps n and $n+1$) whereas the leapfrog scheme is a three-level scheme (time step $n-1$ is also involved). Two-level schemes are more attractive, since no computational initial condition is required as for three-level schemes. Certain types of non-linear computational instability can be avoided for this reason (Morton, 1971). In practical situations two-level schemes lead to smaller requirements for computer storage and allow exact model restarts to be made from a single field (Gadd, 1978a).

The damping and phase errors of the Lax-Wendroff scheme have been studied by Morton (1971), who indicated that the phase performance is rather poor compared to the leapfrog scheme on a time-staggered grid. Without time staggering the phase lag errors of the two schemes are similar (Gadd, 1978a).

Gadd (1978a) illustrated that a simple and inexpensive modification to the Lax-Wendroff scheme may result in a scheme with substantially reduced phase speed errors. In this modified Lax-Wendroff scheme the first step (equation **(4.27)**) remains the same. In the second step four rather than two grid points are used in the finite difference approximation to the spatial derivatives. Thus, equation **(4.28)** is replaced by

$$\psi^{n+1} = \psi^{n} - (1+a)\left\{\alpha_1\left(\delta_x \psi^{y}\right)^{n+\frac{1}{2}} + \alpha_2\left(\delta_y \psi^{x}\right)^{n+\frac{1}{2}}\right\} + a\left\{\alpha_1\left(\delta_{3x} \psi^{y}\right)^{n+\frac{1}{2}} + \alpha_2\left(\delta_{3y} \psi^{x}\right)^{n+\frac{1}{2}}\right\} \qquad \textbf{(4.32)}$$

where $a \geq 0$ on intuitive grounds (Gadd, 1978a)

Equation **(4.32)** remains a second order accurate approximation in space and time (Gadd, 1978a). Equations **(4.29)**, **(4.30a)** and **(4.30b)** and **(4.31)** are still applied.

The linear one-dimensional advection equation **(4.4)** provides a useful framework for a theoretical analysis of the stability and phase properties of the Lax-Wendroff schemes. In the one-dimensional case the schemes are constructed in exactly the same way as for the two-dimensional equation:

First, provisional values for the dependant variable ψ at time step $n+\frac{1}{2}$ are calculated at all "half points" $x = \left(i \pm \frac{1}{2}\right)\Delta x$. This is achieved by using

$$\psi^{n+\frac{1}{2}}_{i+\frac{1}{2}} = \left(\psi^{x}\right)^{n}_{i+\frac{1}{2}} - \frac{1}{2}\alpha\left(\delta_x \psi\right)^{n}_{i+\frac{1}{2}} \qquad \textbf{(4.33)}$$

Secondly, the values of the dependant variable (at time level n) is updated at all points $x = i\Delta x$

$$\psi_i^{n+1} = \psi_i^{n} - \alpha\left\{(1+a)\left(\delta_x \psi\right)_i^{n+\frac{1}{2}} - a\left(\delta_{3x}\psi\right)_i^{n+\frac{1}{2}}\right\} \qquad \textbf{(4.34)}$$

Note that

$$\left(\psi^{x}\right)_i^{n} = \frac{\psi^{n}_{i-\frac{1}{2}} + \psi^{n}_{i+\frac{1}{2}}}{2} \qquad \textbf{(4.35)}$$

and

$$\left(\delta_{mx}\psi\right)_i^{n} = \frac{\psi^{n}_{i+\frac{m}{2}} - \psi^{n}_{i-\frac{m}{2}}}{m} \qquad \textbf{(4.36)}$$

As previously mentioned $\alpha = u\frac{\Delta t}{\Delta x}$

Note that $a \geq 0$. Also keep in mind that $a = 0$ reduces to the original Lax-Wendroff scheme. Equations **(4.33)** and **(4.34)** may be combined (Gadd, 1978a) to give

$$\psi_i^{n+1} = \psi_i^n - \alpha\left\{\left(1+\frac{2}{3}a\right)(\delta_{2x}\psi)_i^n - \frac{2}{3}a(\delta_{4x}\psi)_i^n\right\} + \frac{1}{2}\alpha^2\left\{\left(1+\frac{4}{3}a\right)(\delta_x^2\psi)_i^n - \frac{4}{3}a(\delta_{2x}^2\psi)_i^n\right\} \qquad \textbf{(4.37)}$$

4.3.2.2 Amplitude accuracy

The phase and amplitude properties of equation **(4.37)** may be investigated by considering a single Fourier harmonic, with the discrete equivalent in the form of $\psi_i^n = \mathrm{Re}\left\{\Psi^n e^{I(ki\Delta x)}\right\}$. Keeping in mind relationship **(4.18)**, substitution of the Fourier harmonic into equation **(4.37)** yields Gadd (1978a):

$$\lambda(\alpha,k) = 1 - 2\alpha^2\left(\sin\frac{k\Delta x}{2}\right)^2\left[1+\frac{4}{3}a\left(\sin\frac{k\Delta x}{2}\right)^2\right] - 2I\alpha\left(\sin\frac{k\Delta x}{2}\right)\left(\cos\frac{k\Delta x}{2}\right)\left[1+\frac{4}{3}a\left(\sin\frac{k\Delta x}{2}\right)^2\right]$$

(4.38)

Thus, the amplitude of the Fourier harmonic is damped by a factor $|\lambda|$ at each time step. For computational stability it is required that $|\lambda| \leq 1$ for all wave numbers k. Taking absolute values on both sides of equation **(4.38)** and squaring gives

$$|\lambda|^2 = 1 - 4\alpha^2\left(\sin\frac{k\Delta x}{2}\right)^4\left(1+\frac{4}{3}a\left(\sin\frac{k\Delta x}{2}\right)^2\right)\left\{(1-\alpha^2)\left[1+\frac{4}{3}a\left(\sin\frac{k\Delta x}{2}\right)^2\right] - \frac{4}{3}a\right\}$$

(4.39)

which yields the computational stability criterion

$$(1-\alpha^2)\left[1+\frac{4}{3}a\left(\sin\frac{k\Delta x}{2}\right)^2\right] - \frac{4}{3}a \geq 0 \qquad \textbf{(4.40)}$$

When $a = 0$ (Lax-Wendroff scheme) condition **(4.40)** reduces to $\alpha \leq 1$ which is the well-known CFL criterion. For $a = \frac{1}{2}$ condition **(4.40)** reduces to the less generous $\alpha \leq \frac{1}{3}$. This is unacceptable in numerical models where the time step is dictated by the wind speed (Gadd, 1978a) because the calculations are too expensive due to the small time step required to meet the stability criterion. Therefore, a condition is required on a that ensures that $\alpha \le 1$ remains a sufficient condition for stability.

The most restrictive case in equation **(4.40)** is that of $\frac{k\Delta x}{2} = 0$ so that the required condition is $a \le \frac{3}{4}(1-\alpha^2)$. In the scheme proposed by Gadd (1978a) the limiting form of a, namely $a = \frac{3}{4}(1-\alpha^2)$ was adopted.

Lines of constant $|\lambda(\alpha, k)|$ are displayed in figure 4.3 ($a = 0$, Lax-Wendroff scheme) and figure 4.4 ($a = \frac{3}{4}(1-\alpha^2)$, modified Lax-Wendroff scheme), for $0 \le k\Delta x \le \pi$ and $0 \le \alpha \le 1$. Note that only solutions with wavelengths $L_x \ge 2\Delta x$ can be resolved, therefore only wave numbers $k\Delta x \le \pi$ are admissible.

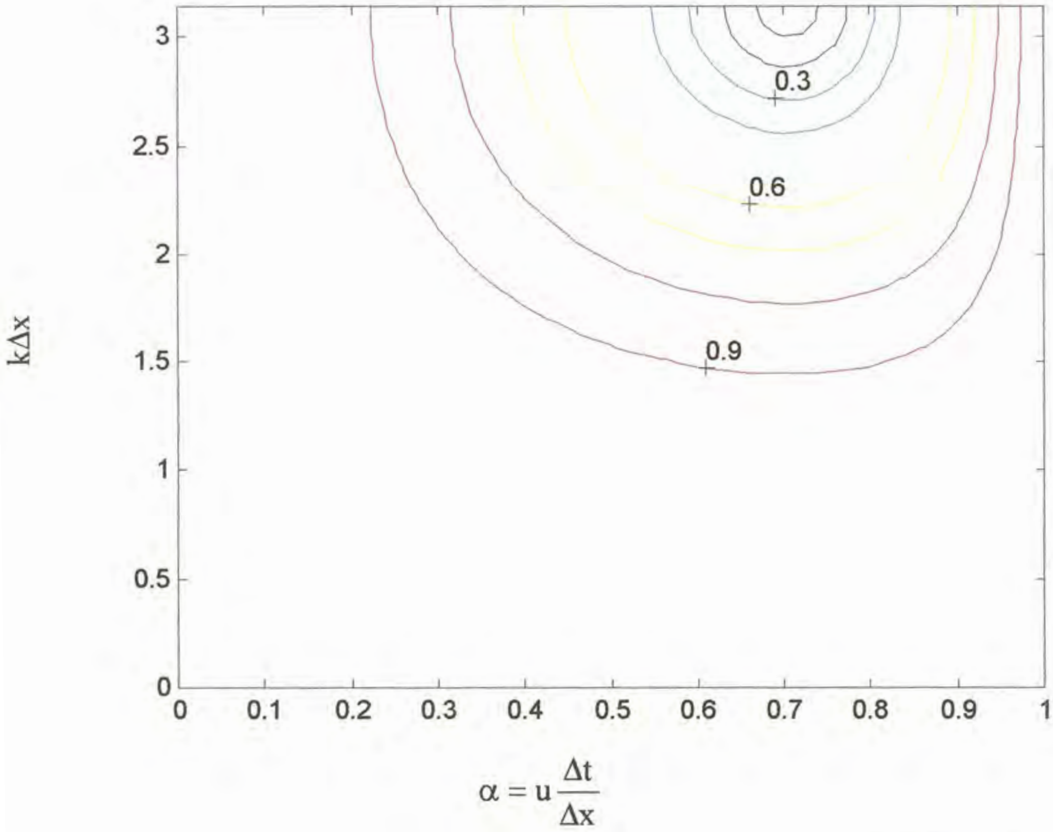

Figure 4.3 Isolines of the amplification factor plotted as a function of $k\Delta x$ and α for the Lax-Wendroff scheme.

In both schemes the damping is most noticeable for the shortest resolvable wavelengths and it decreases as the wavelength increases. Both schemes are undamped when $\alpha = 0.0$ or $\alpha = 1.0$. The Lax-Wendroff scheme is most severely damped when α is close to 0.7 but for the modified Lax-Wendroff scheme most of the damping occurs when α is between 0.5 and 0.6. The modified Lax-Wendroff scheme is the significantly less damped of the two schemes. This represents an improvement of the modified Lax-Wendroff scheme over the Lax-Wendroff scheme.

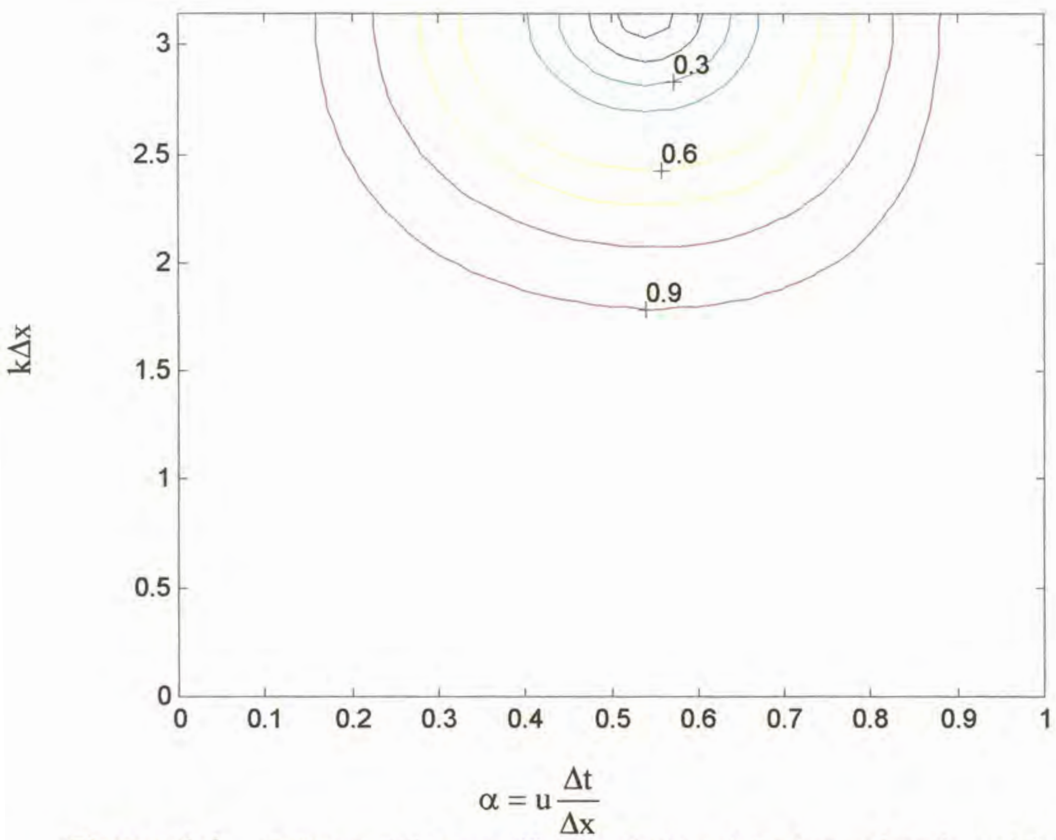

Figure 4.4 Isolines of the amplification factor plotted as a function of $k\Delta x$ and α for the modified Lax-Wendroff scheme.

The stability properties of the two-dimensional Lax-Wendroff schemes correspond closely to those of the one-dimensional schemes. For the two-dimensional version of the scheme $a = \frac{3}{4}\left(1-\chi^2\right)$ is chosen (Gadd, 1978a) where $\chi^2 = \alpha_1^2 + \alpha_2^2$.

Writing

$\alpha_1 = \chi \cos\phi$, $\alpha_2 = \chi \sin\phi$ and $d_x = \frac{1}{2} k\Delta x$, $d_y = \frac{1}{2} l\Delta y$

where k and l are wavenumbers in the x and y directions, it may be shown (Gadd, 1978a) that the application of equations (4.27), (4.28) and (4.31) to a typical Fourier mode yields a amplification factor of

$$\lambda(d_x, d_y, \chi, \phi) = 1 - 2\chi^2 A\{A + (1-\chi^2)B\} - 2I\chi\eta\{A + (1-\chi^2)B\}$$

where

$A = \cos\phi \sin d_x \cos d_y + \sin\phi \cos d_x \sin d_y$

$B = \cos\phi \sin^3 d_x \cos d_y + \sin\phi \cos d_x \sin^3 d_y$

and $\eta = \cos d_x \cos d_y$

It may be shown that $|\lambda| \leq 1$ provided that $\chi^2 \leq 1$ (Gadd, 1978a), which is the same as the necessary computational stability criterion for linear two-dimensional advection of the ordinary Lax-Wendroff scheme (Gadd, 1978a). For the special event where $\Delta x = \Delta y$ the necessary condition for stability simplifies to

$$c\frac{\Delta t}{\Delta x} \leq 1 \qquad \textbf{(4.41)}$$

Note that this is more generous than the typical two-dimensional CFL condition **(4.23)** as a result of the averaging operators in **(4.27)** and **(4.28)** (Gadd, 1978a).

4.3.2.3 Phase accuracy

From equations **(4.26)** and **(4.38)** it follows that, when the one-dimensional Lax-Wendroff schemes are applied to the linear advection equation **(4.4)**,

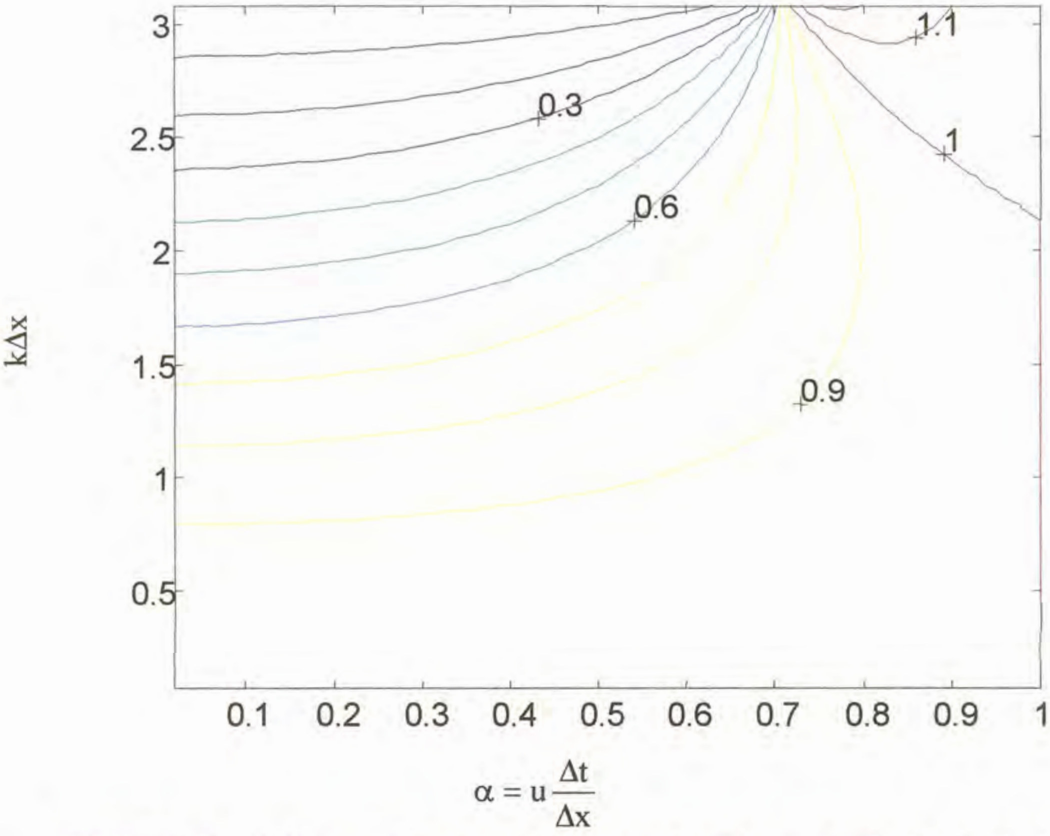

Figure 4.5 Relative phase speed isolines plotted as a function of $k\Delta x$ and α for the Lax-Wendroff scheme.

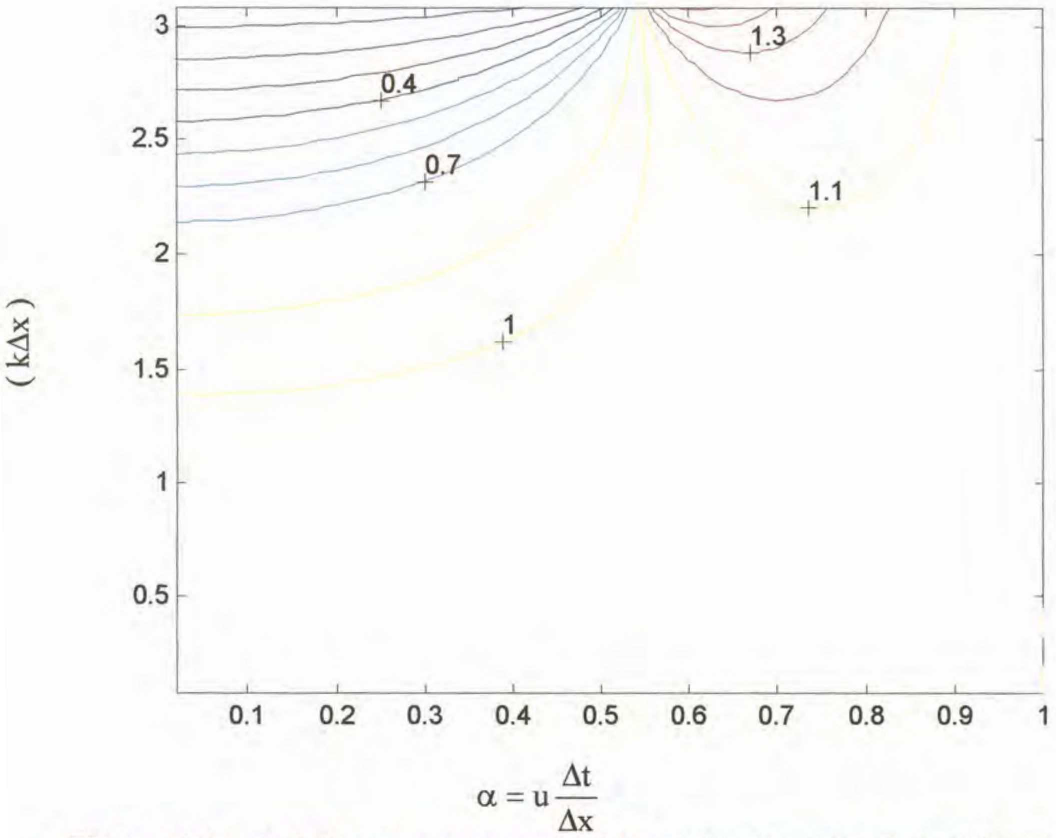

Figure 4.6 Relative phase speed isolines plotted as a function of $k\Delta x$ and α for the modified Lax-Wendroff scheme.

$$R(\alpha,k)=\frac{1}{\omega}\tan^{-1}\left\{\frac{-2\alpha\left(\sin\frac{k\Delta x}{2}\right)\left(\cos\frac{k\Delta x}{2}\right)\left[1+\frac{4}{3}a\left(\sin\frac{k\Delta x}{2}\right)^2\right]}{1-2\alpha^2\left(\sin\frac{k\Delta x}{2}\right)^2\left[1+\frac{4}{3}a\left(\sin\frac{k\Delta x}{2}\right)^2\right]}\right\} \qquad \textbf{(4.42)}$$

Relative phase speed isolines are plotted in figure 4.5 (Lax-Wendroff scheme) and figure 4.6 (modified Lax-Wendroff scheme) for $0 \le k\Delta x < \pi$ (admissible wave numbers) and $0 \le \alpha = u\frac{\Delta t}{\Delta x} \le 1$ (the one-dimensional CFL-criterion, compare this to equation **(4.41)**)

The superior phase properties of the modified Lax-Wendroff scheme (compared to the Lax-Wendroff scheme (figure 4.5) and leapfrog scheme (figure 4.1)) are obvious from figure 4.6. Interesting to note is that for most values of α and k the numerical phase speed is slightly greater than the analytic phase speed, in contrast to the usual phase lag of finite difference models (Gadd, 1978a). Gadd (1978a) discusses the case where $k\Delta x = \pi$ (corresponding to the shortest resolvable wave). This wave either does not move at all or moves exactly one grid length in a time step. The transition occurs when $\alpha^2 = 1 - \frac{1}{\sqrt{2}}$, which gives a singularity in R. Since this wave is not properly resolved (Gadd, 1978a) the strong damping visible in figures 4.5 and 4.6 at $k\Delta x = \pi$ is an advantage.

4.4 MCGREGOR'S SEMI-LAGRANGIAN ADVECTION SCHEME

4.4.1 MULTIPLY-UPSTREAM SEMI-LAGRANGIAN ADVECTION

In the semi-Lagrangian approach of numerically simulating advection, a set of particles which arrive at a regular set of grid points are traced back over a single time interval to their departure points. The values of the dynamical quantities at the departure points are obtained by interpolation from neighbouring grid points with known values. The essential feature of semi-Lagrangian numerical models is that the total, or material derivatives, in the equations of motion are treated directly by calculating the departure points of fluid parcels. The upstream value of the required fields are usually evaluated by spatial interpolation (McGregor, 1993).

In multiply-upstream semi-Lagrangian schemes the grid points used for interpolation to the departure point of a particle are chosen in such a way that they always surround the departure point. When the winds are strong, this set of grid points may be many grid intervals upstream from the arrival grid point of the particle. The term "multiply-upstream" is used to describe a scheme using interpolation points chosen in this way (Bates and McDonald, 1982).

4.4.2 MCGREGOR'S METHOD OF DETERMINING DEPARTURE POINTS

During an integration of the primitive equations using the multiply-upstream semi-Lagrangian approach, the departure point (x_*, y_*) of a particle in a velocity field $\overline{v} = (u, v)$ over a time interval Δt may be estimated in a variety of ways. A simple straight-line trajectory back in time using only the velocity at the arrival point possesses inadequate accuracy (Robert, 1982). Most schemes therefore involve a sequence of iterations. A first guess of the departure position is determined by using a straight-line trajectory and an estimation of the departure velocity is then found by horizontal interpolation at the central point of the trajectory. This process is repeated several times using an updated advection velocity (McDonald, 1987; McDonald and Bates, 1987, 1989). McGregor (1993) points out that a significant overhead of such schemes can arise from the horizontal interpolation (traditionally bicubic) that is carried out during the iterations. Several authors however, reported acceptable accuracy using just linear interpolation (Temperton and Staniforth, 1987; Bates et al., 1990).

McGregor (1993) derived a more economical method to determine the position of departure points that avoids horizontal interpolation in the trajectory analysis. The method considers a set of vectors moving with the fluid where each vector will be associated at time t with a different grid point. Note that the grid points have fixed locations while the vectors move with the fluid. To advance the model integration from time t to time t + Δt, a vector $\bar{r}(t+\Delta t)$ is constructed at the position of each arrival grid point. It is required to identify a starting position for the vector at the preceding time step namely $\bar{r}(t)$. Each vector $\bar{r}(t)$ therefore represents a departure point in the form (x_*, y_*). The process may be expressed in terms of a truncated Taylor series (McGregor, 1993), namely

$$\bar{r}(t) \approx \bar{r}(t+\Delta t) + \sum_{n=1}^{N} \frac{(-\Delta t)^n}{n!} \frac{d^n \bar{r}}{dt^n}(t+\Delta t) \qquad \textbf{(4.43)}$$

where

$$\frac{d^n \bar{r}(t)}{dt^n} = \frac{d}{dt} \frac{d^{n-1} \bar{r}(t)}{dt^{n-1}} \qquad n = 2,3,\ldots N \qquad \textbf{(4.44)}$$

and the total derivative operator has the usual definition of a time derivative that follows the motion of a parcel,

$$\frac{d}{dt} = \frac{\partial}{\partial t} + \bar{v} \cdot \bar{\nabla}. \qquad \textbf{(4.45)}$$

An array of the vectors $\bar{r}(t+\Delta t)$ is needed so that the $\bar{v} \cdot \bar{\nabla}$ operator in equation **(4.45)** may be conveniently evaluated. $\bar{v} = \frac{d\bar{r}}{dt}$ is the velocity of the fluid at position $\bar{r}(t)$, and $\bar{\nabla}$ is the spatial gradient operator. In equation **(4.45)** the time derivative on the left-hand side is naturally viewed from a Lagrangian viewpoint. The right hand side allows for its instantaneous evaluation at the same point in time and space via Eulerian derivatives (McGregor, 1993). McGregor (1993) points out that in the above equations, each component of $\bar{r} = (x_*, y_*)$ may be obtained independently from the others.

If the Eulerian velocity changes with time it becomes difficult, or at least very cumbersome, to evaluate the partial time derivatives for the higher order terms at $t + \Delta t$. In the scheme proposed by McGregor (1993) the total time derivative in **(4.45)**, for use in **(4.43)** and **(4.44)**, is replaced by the following approximation:

$$\frac{d}{dt} \approx \hat{v} \cdot \bar{\nabla}. \qquad \textbf{(4.46)}$$

Here $\hat{v}$ represents the Eulerian velocity at the point in space which corresponds to $\bar{r}(t+\Delta t)$, but is evaluated at the intermediate time $t + \frac{\Delta t}{2}$

(McGregor, 1993). The velocity $\hat{v}$ may conveniently be determined from the known velocities at previous time steps (McGregor, 1993). Temperton and Staniforth (1987), suggested the following third-order accuracy formulation in time:

$$\hat{v} = \frac{1}{8}\left[15\bar{v}(t) - 10\bar{v}(t-\Delta t) + 3\bar{v}(t-2\Delta t)\right] + O\left(\Delta t^3\right)$$

From an Eulerian point of view, approximation **(4.46)** suggests that for advection purposes, the velocities remain constant at their centred-in-time values over the time interval $[t, t+\Delta t]$ (McGregor, 1993).

The above scheme, using equations **(4.43)**, **(4.44)** and **(4.46)** and retaining terms up to the N^{th} total time derivative, is called a D_N scheme (McGregor, 1993). Equation **(4.46)** indicates that the lowest-order D_1 scheme only produces a straight-line trajectory, using a velocity $\hat{v}$ evaluated at the arrival position. The D_2 scheme uses estimates for both the velocity and acceleration along the trajectory. The D_3 and higher-order versions of the scheme effectively solve the trajectory by incorporating higher-order curvature terms derived kinematically for the arrival point from the velocity field $\hat{v}$ at time $t + \frac{\Delta t}{2}$ (McGregor, 1993). The number of terms that should be retained in the Tailor series **(4.43)** depends on the smoothness of the velocity field (McGregor, 1993). McGregor (1993) mentions that only slight benefit has been found in going beyond the D_3 scheme. Above, the scheme description focuses on two time-level applications. This might be modified if three time-level applications are required (McGregor, 1993).

4.4.3 INTERPOLATION

Approximating the non-linear or linear two-dimensional advection equation according to the semi-Lagrangian philosophy yields

$$\psi\{I_*\Delta x, J_*\Delta y, (n+1)\Delta t\} = \psi\{x_*, y_*, n\Delta t\}. \tag{4.47}$$

Here (x_*, y_*) denote the position of the departure point for the arrival grid point $(I_*\Delta x, J_*\Delta y)$. Introducing the notation $\psi^n_{I_*,J_*} = \psi(I_*\Delta x, J_*\Delta y, n\Delta t)$, the function $\psi(x_*, y_*, t)$ is approximated by a Lagrange interpolating polynomial (Carnahan et al., 1969) using values of ψ at the grid positions nearest to x_* and y_*:

$$\psi(x_*, y_*, t) = \sum_{\mu}\sum_{\nu} W_{\mu\nu}\psi^n{}_{\mu\nu} \tag{4.48}$$

where

$$W_{rs} = \prod_{\mu \neq r} \frac{(x_* - x_\mu)}{(x_r - x_\mu)} \prod_{\nu \neq s} \frac{(y_* - y_\nu)}{(y_s - y_\nu)} \qquad \textbf{(4.49)}$$

McDonald (1984) investigated the relative merits of bilinear, biquadratic, bicubic and biquartic interpolation schemes to approximate $\psi(x_*, y_*, t)$ for constant in time velocity fields. The semi-Lagrangian scheme used by McDonald closely relates to the D1 scheme (the schemes are identical for constant in time velocity fields). McDonald (1984) found that bicubic interpolation gives the best phase representation of the true solution and bicuartic interpolation the most faithful amplitude representation. In DARLAM, bicubic interpolation is employed.

The subscripts μ and ν range over the points being used in the bicubic interpolation as:

$$\mu : i-2, i-1, i, i+1 \qquad\qquad \upsilon : j-2, j-1, j, j+1 \qquad \textbf{(4.50)}$$

The points (i, j) are chosen for the bicubic interpolation such that

$$(i-1)\Delta x < x_* \leq i\Delta x \qquad\qquad (j-1)\Delta y < y_* \leq j\Delta y \qquad \textbf{(4.51)}$$

4.4.4 AMPLITUDE ACCURACY

An investigation of the stability properties of multiply-upstream semi-Lagrangian schemes, when applied to the linear advection equation, reveals interesting properties. For the linear two-dimensional advection equation **(4.2)** or linear one-dimensional advection equation **(4.4)**, the velocity field is constant, so that $\frac{d\bar{r}^n}{dt^n}$ vanishes when $n \geq 2$. Thus, as indicated by equation **(4.43)** all the D_N schemes reduce to the D_1 scheme.

If α, $\hat{\alpha}$, β, and $\hat{\beta}$ are defined as

$$\alpha = u\frac{\Delta t}{\Delta x} \qquad\qquad \beta = v\frac{\Delta t}{\Delta y}$$

$$\hat{\alpha} = \alpha + i - I_* \qquad\qquad \hat{\beta} = \beta + j - J_* \qquad \textbf{(4.52)}$$

the selection of i and j in equation **(4.51)** guarantees that

$$0 \leq \hat{\alpha} < 1 \qquad \text{and} \qquad 0 \leq \hat{\beta} < 1 \qquad \textbf{(4.53)}$$

McDonald (1984) showed that these conditions are sufficient to ensure unconditional stability of his multiply-upstream semi-Lagrangian scheme when applied to the linear advection equation.

In order to examine the stability of the D$_1$ scheme with bicubic interpolation for constant advection velocity, a solution in the form of a single harmonic (equation **(4.15)**) is assumed and substituted into equation **(4.47)**. Equations **(4.48)** and **(4.49)** are used to evaluate $\psi(x_*, y_*, t)$.

First note that equation **(4.49)** can be written as

$$W_{rs} = \prod_{\mu \neq r} \frac{(x_* - x_\mu)}{(x_r - x_\mu)} \prod_{\nu \neq s} \frac{(y_* - y_\nu)}{(y_s - y_\nu)} = w_r w_s$$

where

$$w_r = \prod_{\mu \neq r} \frac{(x_* - x_\mu)}{(x_r - x_\mu)} \quad \text{and} \quad w_s = \prod_{\nu \neq s} \frac{(y_* - y_\nu)}{(y_s - y_\nu)}. \qquad \textbf{(4.54)}$$

Using equations **(4.50)**, **(4.51)** and **(4.52)** equation **(4.54)** can be written as

$$w_{i+r} = \prod_{\substack{\mu=-2 \\ \mu \neq r}}^{1} \frac{\hat{\alpha} + \mu}{\mu - r} \quad \text{and} \quad w_{j+s} = \prod_{\substack{\nu=-2 \\ \nu \neq s}}^{1} \frac{\hat{\beta} + \nu}{\nu - s} \qquad \textbf{(4.55)}$$

where the subscripts μ and ν range over the points: $\mu: -2, -1, 0, 1 \quad \nu: -2, -1, 0, 1$. Substituting the harmonic into equation **(4.47)** yields

$$\psi_{I_*, J_*}^{n+1} = \sum_{\mu=-2}^{1} \sum_{\nu=-2}^{1} w_{i+\mu} w_{j+\nu} \psi_0 \lambda^n e^{I[(i+\mu)k\Delta x + (j+\nu)l\Delta y]}$$

This may be expressed as

$$\psi_{I_*, J_*}^{n+1} = \sum_{\mu=-2}^{1} \sum_{\nu=-2}^{1} w_{i+\mu} w_{j+\nu} \psi_0 \lambda^n e^{I(ik\Delta x + jl\Delta y)} e^{I\mu k\Delta x} e^{I\nu l\Delta y} .$$

Rearranging the terms gives

$$\psi_{I_*, J_*}^{n+1} = \left\{ \sum_{\mu=-2}^{1} w_{i+\mu} e^{I\mu k\Delta x} \sum_{\nu=-2}^{1} w_{i+\nu} e^{I\nu l\Delta y} \right\} \psi_0 \lambda^n e^{I(ik\Delta x + jl\Delta y)}$$

Substitution of equation **(4.55)** into the last equation gives

$$\psi_{I_*, J_*}^{n+1} = \left\{ \sum_{\mu=-2}^{1} \prod_{\substack{r=-2 \\ r \neq \mu}}^{1} \frac{\hat{\alpha} + r}{r - \mu} e^{I\mu k\Delta x} \sum_{\nu=-2}^{1} \prod_{\substack{s=-2 \\ s \neq \nu}}^{1} \frac{\hat{\beta} + s}{s - \nu} w_{i+\nu} e^{I\nu l\Delta y} \right\} \psi_0 \lambda^n e^{I(ik\Delta x + jl\Delta y)}$$

Thus, λ splits into the product of a "x-amplification factor" and "y-amplification factor" (McDonald, 1984) in the following way:

$$\lambda = \hat{\Lambda}(\hat{\alpha},k)\hat{\Lambda}(\hat{\beta},l),$$

where

$$\hat{\Lambda}(\hat{\alpha},k) = \sum_{\mu=-2}^{1}\prod_{\substack{r=-2\\ r\neq\mu}}^{1}\frac{\hat{\alpha}+r}{r-\mu}e^{I\mu k\Delta x} \quad \text{and} \quad \hat{\Lambda}(\hat{\beta},l) = \sum_{\nu=-2}^{1}\prod_{\substack{s=-2\\ s\neq\nu}}^{1}\frac{\hat{\beta}+s}{s-\nu}e^{I\nu l\Delta y}.$$

This makes the analysis particularly simple. A scheme is stable if both $\left|\hat{\Lambda}(\hat{\alpha},k)\right| \leq 1$ and $\left|\hat{\Lambda}(\hat{\beta},l)\right| \leq 1$ since it guarantees that $|\lambda \leq 1|$. A little bit of algebra shows that (McDonald, 1984):

$$\hat{\Lambda}(\hat{\alpha},k) = \left[1 - c\hat{\alpha}^2 - \frac{c^2\hat{\alpha}(1-\hat{\alpha}^2)}{3}\right] + I\hat{\alpha}\sin(k\Delta x)\left[1 + \frac{c(1-\hat{\alpha}^2)}{3}\right] \qquad \textbf{(4.56)}$$

where $c = 1 - \cos(k\Delta x)$. This yields

$$\left|\hat{\Lambda}(\hat{\alpha},k)\right|^2 = 1 - \frac{\hat{\alpha}(2-\hat{\alpha})(1-\hat{\alpha}^2)c^2[3 + 2c\hat{\alpha}(1-\hat{\alpha})]}{9} \qquad \textbf{(4.57)}$$

As can be shown, $\left|\hat{\Lambda}(\hat{\alpha},k)\right| \leq 1$ as long as $0 \leq \hat{\alpha} \leq 1$. Similarly, $\left|\hat{\Lambda}(\hat{\beta},l)\right| \leq 1$ for $0 \leq \hat{\beta} < 1$ as can be seen by replacing $\hat{\alpha}$ and k with $\hat{\beta}$ and l in equation **(4.57)**. Hence the scheme is unconditionally stable since conditions applicable to $\hat{\alpha}$ and $\hat{\beta}$ are guaranteed by the choice of interpolation grid points given in **(4.51)**.

Following McDonald (1984) the quantities $\hat{\alpha}$ and $\hat{\beta}$ can also be expressed in the bicubic interpolation schemes as

$$\begin{aligned} \hat{\alpha} &= \alpha - [\alpha] && \text{if } \alpha \geq 0 \\ \hat{\alpha} &= \alpha - [\alpha - 1] && \text{if } \alpha < 0 \end{aligned}$$

Here, $[x]$ is the integer part of x, $\hat{\beta}$ is defined in exactly the same way as $\hat{\alpha}$ with β replacing α in all the above equations. Substituting these values of $\hat{\alpha}$ in equation **(4.57)** gives a function $|\Lambda(\alpha,k)| = \left|\hat{\Lambda}(\hat{\alpha},k)\right|$ with the property that

$$|\Lambda(\alpha+n,k)| = |\Lambda(\alpha,k)| \qquad \textbf{(4.58)}$$

where n represents any integer.

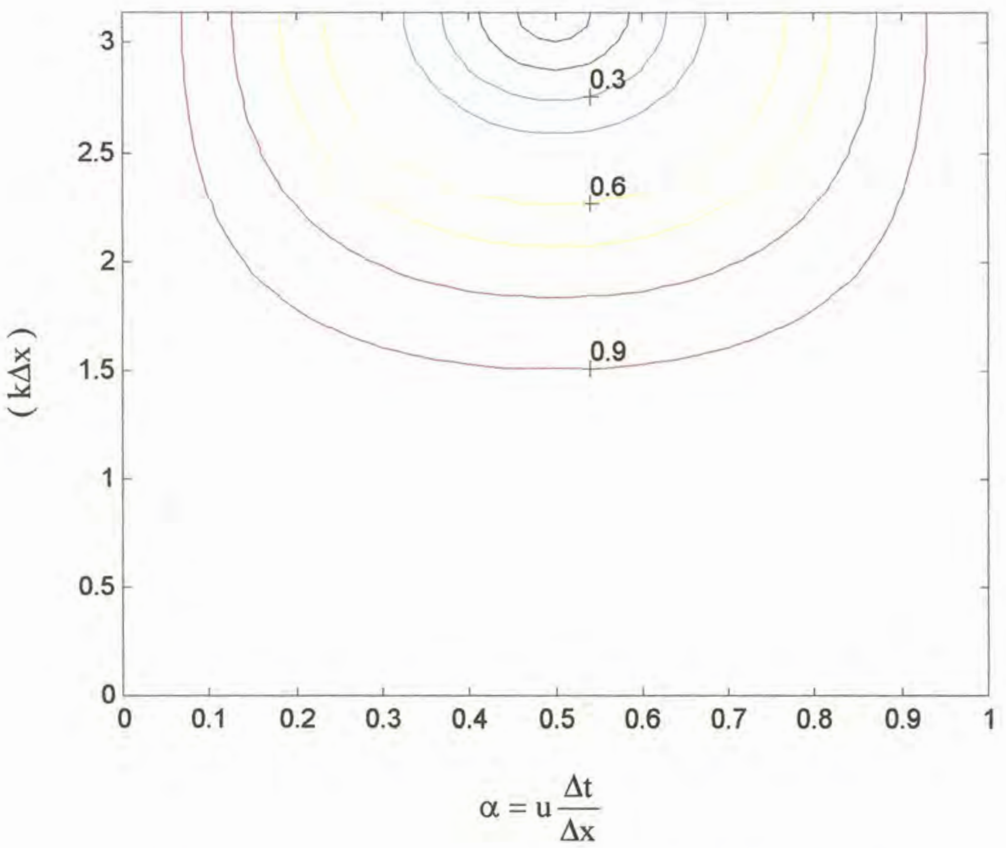

Figure 4.7 Isolines of the amplification factor plotted as a function of $k\Delta x$ and α for the D_1 scheme.

The lines of constant $|\Lambda(\alpha,k)|$ are displayed in figure 4.7 for $0 \le k\Delta x < \pi$ (the admissible wave numbers) and $0 < \alpha \le 1$. Equation **(4.58)** ensures that the graphs for all other regions $n < \alpha \le n+1$ are identical to the graph illustrated in figure 4.7. Note that for the one-dimensional linear advection equation **(4.4)** it applies that $|\lambda(\hat{\alpha},k)| = |\hat{\Lambda}(\hat{\alpha},k)|$, so that figure 4.8 is directly comparable to figures 4.3 and 4.4.

The D_N schemes with bicubic interpolation are most severely damped when $\alpha = 0.5$ and undamped when $\alpha = 0$ or $\alpha = 1$. The damping is the most noticeable at the shortest resolvable wavelengths and it decreases as the wavelength increases. The Lax-Wendroff scheme is most damped, followed by the D_N schemes with bicubic interpolation, modified Lax-Wendroff and leapfrog schemes. No damping is present in the leapfrog scheme as long as the CFL criterion (equation **(4.23)**) applies.

4.4.5 PHASE ACCURACY

From equations **(4.26)** and **(4.56)** and for the D_1 scheme with bicubic interpolation (in one spatial dimension), it follows that:

$$R(\alpha,k)=\frac{-1}{\omega}\tan^{-1}\left\{\frac{\hat{\alpha}\sin(k\Delta x)\left[1+\frac{c\left(1-\hat{\alpha}^2\right)}{3}\right]}{\left[1-c\hat{\alpha}^2-\frac{c^2\hat{\alpha}\left(1-\hat{\alpha}^2\right)}{3}\right]}\right\}$$

Relative phase speed isolines are plotted in figure 4.9 for the D$_1$ scheme where $0 \le k\Delta x \le \pi$ (admissible wave numbers) and $0<\alpha=u\frac{\Delta t}{\Delta x}\le 1$. The figure reveals that the D$_1$ scheme has the most realistic phase representation of all the schemes studied. A net phase lag occurs for $\alpha<\frac{1}{2}$ and there is a phase gain for $\frac{1}{2}<\alpha\le 1$

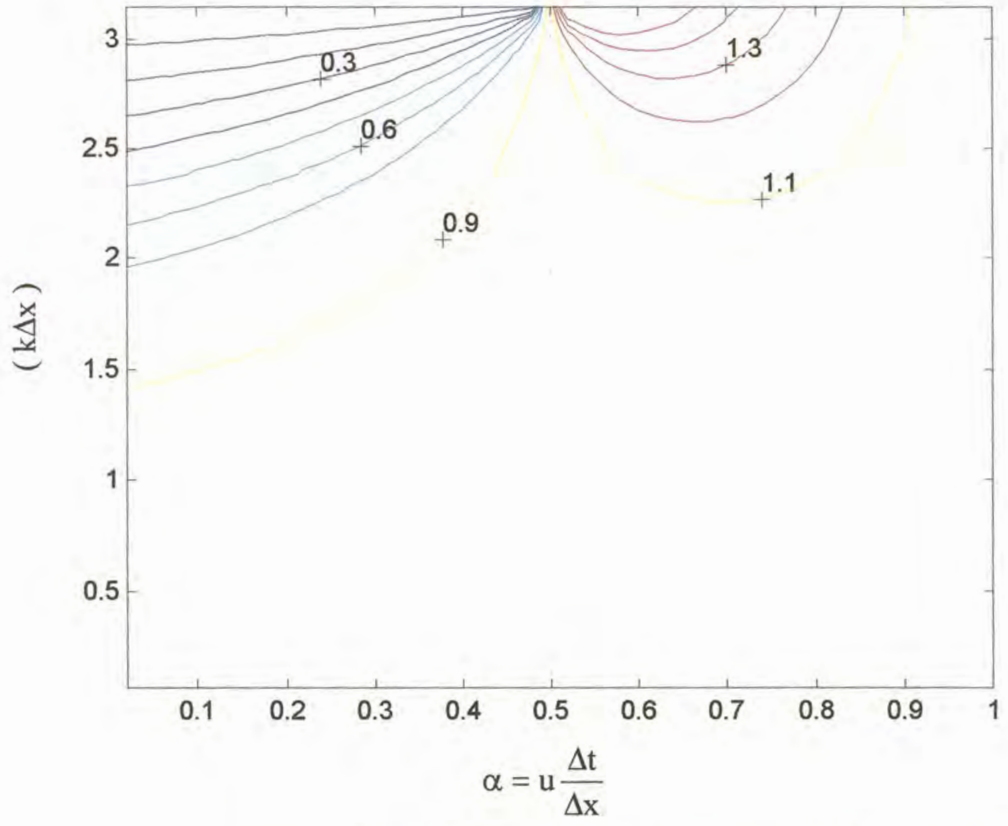

Figure 4.8 Relative phase speed isolines plotted as a function of $k\Delta x$ and α for the D$_1$ scheme.

4.5 TWO-DIMENSIONAL NUMERICAL TESTS

4.5.1 STEADY TWO-DIMENSIONAL FLOW: CROWLEY'S CONE TEST

In this section the accuracy and stability of the semi-Lagrangian D_1, D_2 and D_3 schemes are examined and compared to the Leapfrog and Lax-Wendroff finite difference schemes. The test problem used for this purpose is the advection of a cone at constant angular velocity about a point in the (x, y) plane, using the two-dimensional advection equation **(4.1)** (Crowley, 1968). The domain consists of 33x33 grid points covering the area $-16 \le x \le 16, -16 \le y \le 16$. An equation for the cone in its initial position, where the height ψ at any point is expressed as a function of x and y, is

$$\psi(x,y) = -25\sqrt{(x+8)^2 + y^2} + 100; \quad (x+8)^2 + y^2 \le 16$$

The cone therefore has an initial height of $\psi = 100$ units, a base diameter of 8 grid units and is initially centred at position $(-8,0)$. The domain configuration includes a buffer zone of one row around the lateral boundary where the height is held zero. These are the same settings as those used previously by McDonald (1984) and McGregor (1993).

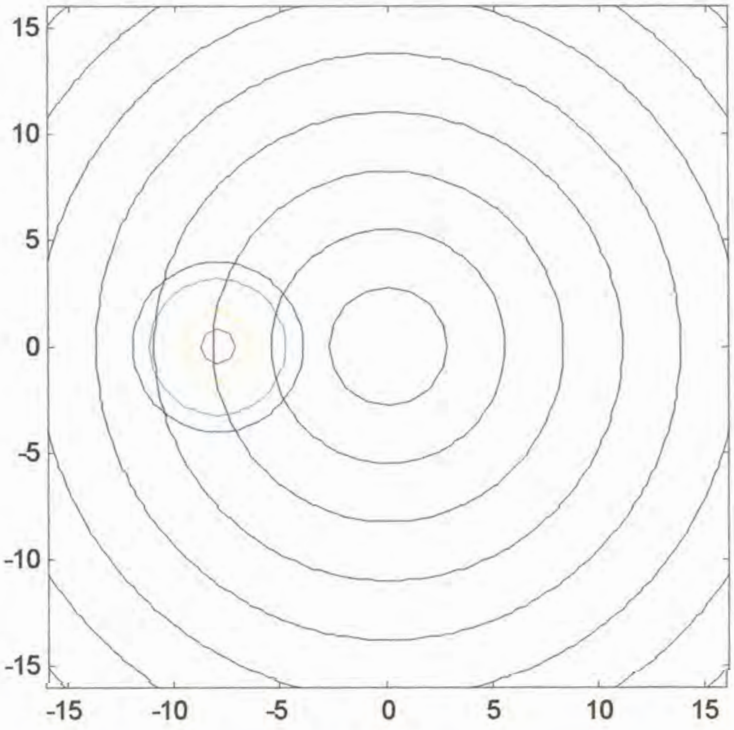

Figure 4.9 Isotachs of the velocity field (black contours) for Crowley's cone test with the initial cone location in colour. The cone has a height of 100 units, a base diameter of 8 units and is centred at position (-8,0).

The velocity field is given by

$$\overline{v} = (\Omega y, -\Omega x)$$

which constitutes steady two-dimensional solid-body rotation about the position $(0,0)$.

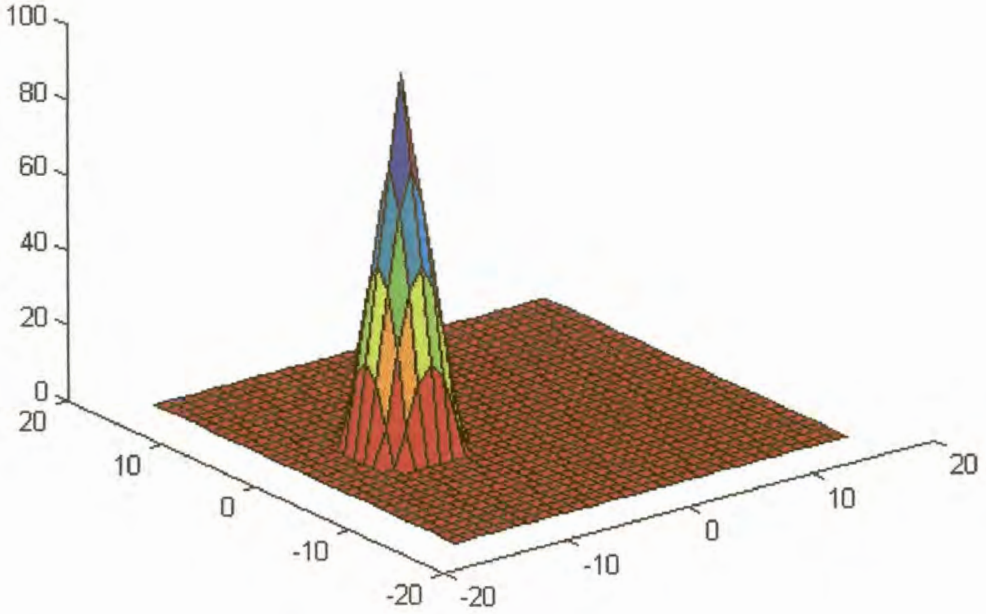

Figure 4.10 Initial cone configuration in 3-dimensions for Crowley's test. The cone has a height of 100 units, base diameter of 8 units and is centred at position (-8,0).

Isotachs (constant wind speed contours) of the constant in time velocity field (black contours) and height level contours which depict the initial cone position are displayed in figure 4.9. The rotation is clockwise and the angular velocity is chosen to be $\Omega = 7.2722$ rads^{-1}. A 3-dimensional representation of the cone in figure 4.9 is displayed in figure 4.10.

Since the evolution of ψ is governed by advection only and the specified velocity field corresponds to solid rotation, it is expected that the cone should migrate in a circle of constant radius in a clockwise direction around the centre of the grid mesh.

In this section the term "integration area" is used to refer to all the inner grid points, in other words, the 31x31 grid points covering the domain where $-15 \leq x \leq 15, -15 \leq y \leq 15$. The passive lateral boundary zone where the height of the cone is held zero is therefore excluded from the integration area. Two complications may develop near the boundary of the integration area during semi-Lagrangian calculations. In the first place the upstream point (x_*, y_*) may be of such a nature that the values of (i, j), which satisfy equation **(4.51)**, fall outside the defined domain. Secondly, even if these points fall inside the domain, some of the points needed to perform the interpolation may fall outside. Following McDonald (1984), a solution to the former complication is to introduce a number of additional passive boundary lines when the field is initially defined. Similar to the passive boundary zone, the height of the cone is kept as zero at the additional boundary points and is never updated during the integration. The number of passive lateral boundary rows is chosen as the smallest integer greater than the maximum possible value of $|\kappa_x|$ or $|\kappa_y|$, where

$$\kappa_x = \sum_{n=1}^{N} \frac{(-\Delta t)^n}{n!} \frac{d^n x}{dt^n} \qquad \text{and} \qquad \kappa_y = \sum_{n=1}^{N} \frac{(-\Delta t)^n}{n!} \frac{d^n y}{dt^n}$$

Here, $N = 1,2,3$ for the D_1, D_2 and D_3 schemes respectively.

The second complication is resolved by performing a bilinear interpolation whenever the bicubic interpolation scheme requires points which fall outside the area of integration plus additional boundary lines.

As long as $|\kappa_x|$ and $|\kappa_y|$ are < 1, only one passive boundary line is required. If values of $|\kappa_x|$ and $|\kappa_y|$ are expected to be less or equal than m (where m is a positive integer), m passive boundary lines must be included. If space is at its premium, the inclusion of additional boundary rows represents a drawback of the semi-Lagrangian schemes, since the size of the arrays has to be increased to accommodate these additional values of the fields.

Figure 4.11a shows the scalar distribution of the cone after one revolution using the Leapfrog scheme with 48 steps per revolution. The associated time step yields that the maximum value of $\frac{c\Delta t}{\Delta x}$ (listed in Table 4.1) is almost four times the maximum value allowed for the CFL criterion (equation **(4.23)**) to be satisfied. Thus, it is not surprising that the solution became unstable (note the dramatic increase in cone height depicted in figure 4.11a).

Figure 4.11b (288 steps per revolution) vividly illustrates other typical problems associated with finite difference approximations of the non-linear advection equation. Although the integration remained stable (the CFL criterion is satisfied in this case, see Table 4.1), large errors in phase and amplitude are present (Table 4.2). Spurious trailing waves can also be observed in the numerical solution (figure 4.11b).

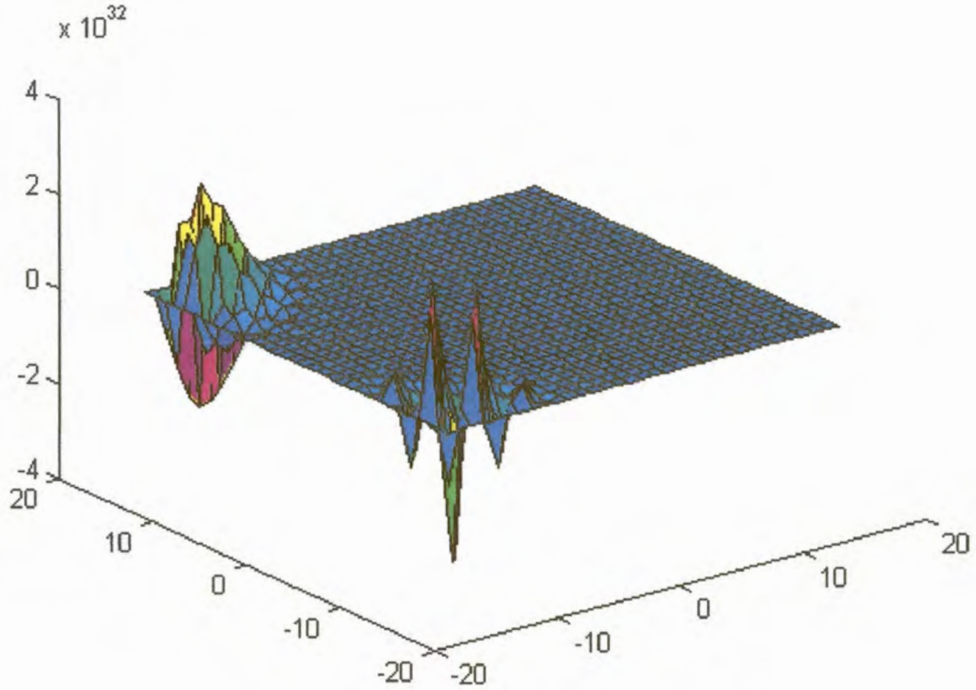

Figure 4.11a The advected scalar field in Crowley's cone test after one revolution (48 steps) with the Leapfrog scheme.

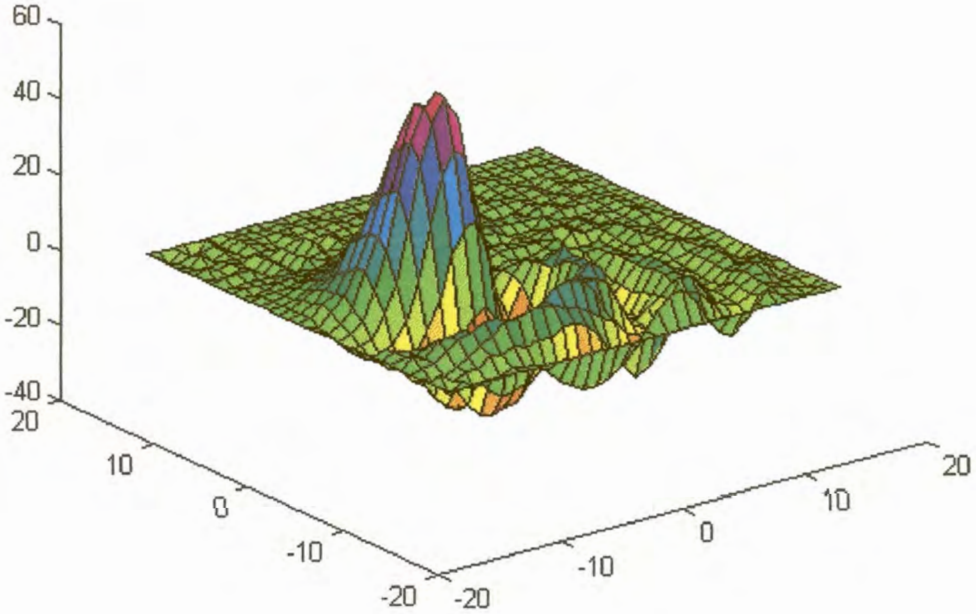

Figure 4.11b The advected scalar field in Crowley's cone test after one revolution (288 steps) with the Leapfrog scheme.

Figures 4.12a and 4.12b show the scalar distribution after one revolution using the Lax-Wendroff and modified Lax-Wendrof schemes respectively with 288 time steps per revolution. The time step yields that the maximum value of $\frac{c\Delta t}{\Delta x}$ (listed in Table 4.1) in the two schemes is less than half the value required to satisfy the CFL criterion (equation **(4.41)**). Figures 4.12a and 4.12b as well as Table 4.2 clearly illustrate that the Lax-Wendroff scheme has damping and phase properties that are inferior to those of the modified Lax Wendroff scheme. Unpleasant trailing waves occur in both integrations, but the amplitudes of these waves are significantly smaller for the modified Lax Wendroff scheme. Conservation properties of the modified Lax-Wendroff scheme are undoubtedly superior to those of the Lax-Wendroff scheme (Table 4.2). Whilst the modified Lax-Wendroff scheme clearly represents an improvement over the Lax-Wendroff (and the Leapfrog) schemes, phase errors may still be problematic.

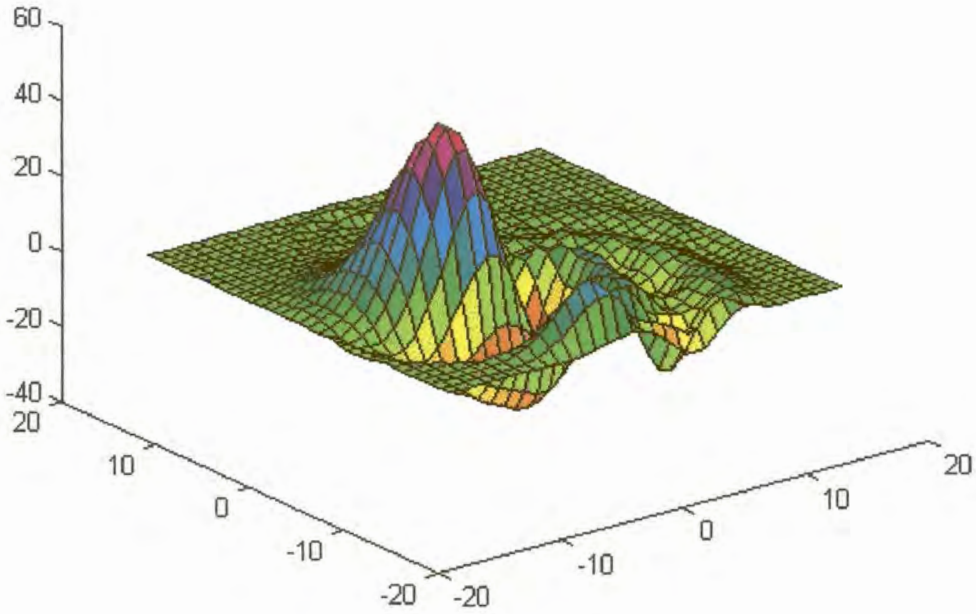

Figure 4.12a The advected scalar field after one revolution (288 steps) with the Lax-Wendroff scheme.

The last column in Table 4.2 also suggests that the Lax-Wendroff scheme has a tendency to artificially enhance the concentration of the advected scalar field.

Both the Lax-Wendroff and modified Lax-Wendroff schemes become unstable when 48 steps are used for one revolution. This comes as no surprise, since the CFL criterion is violated by a factor of almost three (Table 4.1). Note that in comparison with the Leapfrog and semi-Lagrangian schemes, the quantity $c\frac{\Delta t}{\Delta x}$ attains larger magnitudes (for this specific velocity field) when the two Lax-Wendroff schemes are used. This is due to caculations performed at the outer "half-points" during integrations with the two Lax-Wendroff schemes.

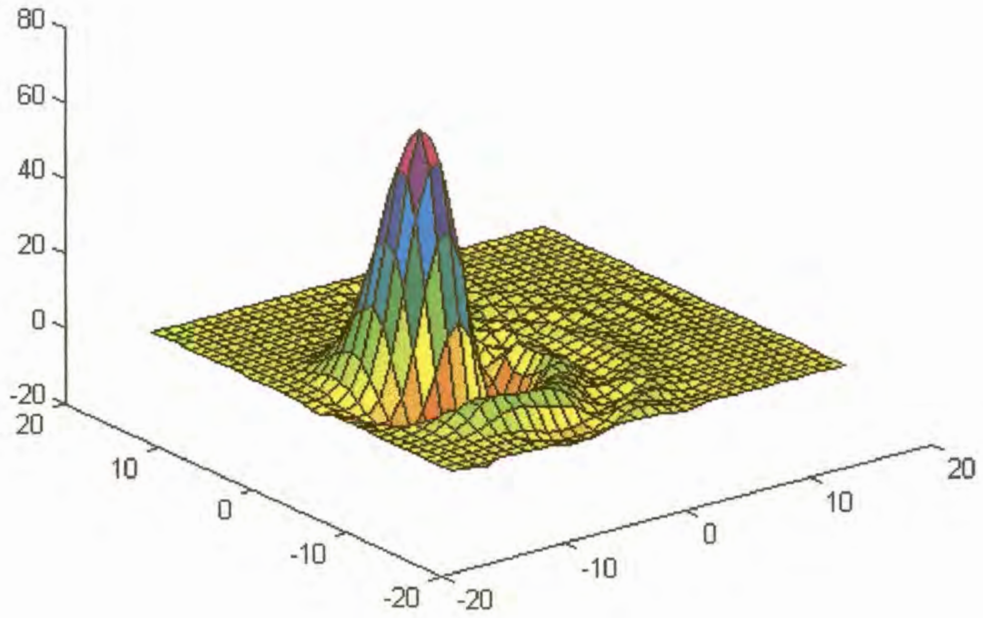

Figure 4.12b The advected scalar field after one revolution (288 steps) with the modified Lax-Wendroff scheme.

Scheme	Number of time steps per revolution	$c\frac{\Delta t}{\Delta x}$	Number of passive boundary lines needed
Leapfrog	48	2.777	1
	288	0.463	1
Lax-Wendroff	48	2.869	1
	288	0.478	1
Modified	48	2.869	2
Lax-Wendroff	288	0.478	2
D1, D2 and D3	48	2.777	3
	288	0.463	1

Table 4.1. Maximum values of $c\frac{\Delta t}{\Delta x}$ and the number of passive boundary lines required for the various schemes expressed as a function of the amount of time steps used per revolution in Crowley's cone test.

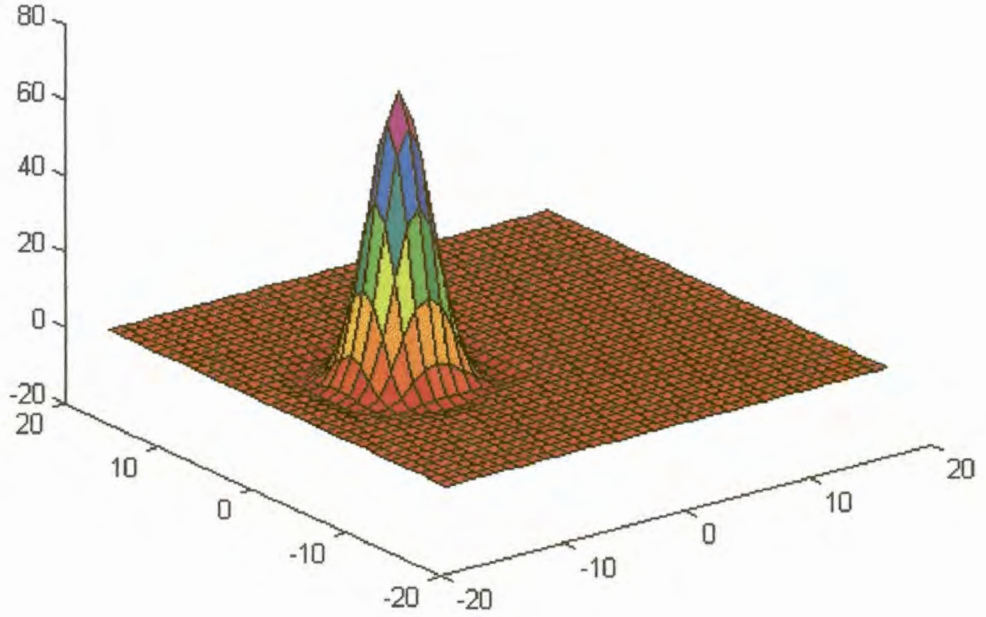

Figure 4.13a The advected scalar field after one revolution (48 steps) with the D_3 scheme.

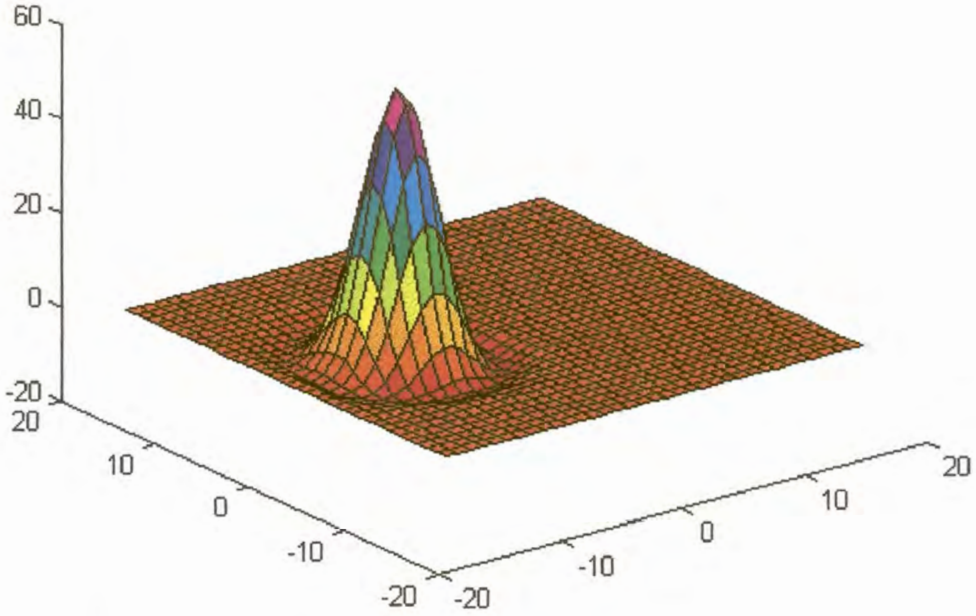

Figure 4.13b The advected scalar field after one revolution (288 steps) with the D_3 scheme.

The position and symmetry of the scalar distribution after one revolution using 48 steps (figure 4.13a) or 288 steps (figure 4.13b) are excellent for the D_1, D_2 and D_3 schemes. The figures are for the D_3 scheme. Some smoothing of the profile is however evident for smaller time steps (Table 4.2). The height errors for the higher-order semi-Lagrangian schemes (Table 4.2) are least when larger time steps are used. This may be attributed to the smaller number of interpolations performed at each revolution (McGregor, 1993). Note that the semi-Lagrangian schemes remain stable (Table 4.2) when 48 steps per revolution is used, despite the fact that the CFL criterion is violated by a factor of almost three (Table 4.1).

Scheme	Number of iterations	Maximum height	Minimum height	Distance error	Angular error in degrees	$\frac{\sum \psi_{ij}}{\sum \psi_{ij}(0)}$	$\frac{\sum \psi_{ij}^2}{\sum \psi_{ij}^2(0)}$	$\frac{\sum \lvert\psi_{ij}\rvert}{\sum \lvert\psi_{ij}(0)\rvert}$
Leapfrog	288	56.8	-22.3	-0.384	-23.2	1.013	1.002	2.602
	2*288	56.3	-22.2	-0.384	-23.2	1.014	1.001	2.613
	4*288	56.3	-22.1	0.062	-29.7	1.014	1.000	2.616
	10*288	56.3	-22.1	0.062	-29.7	1.015	1.000	2.616
Lax-Wendroff	288	48.9	-20.6	0.062	-29.7	1.005	0.867	2.429
	2*288	49.1	-21.7	0.062	-29.7	1.006	0.919	2.613
	4*288	49.3	-22.2	-0.384	-23.2	1.007	0.955	2.743
	10*288	49.6	-22.8	0.062	-29.7	1.008	0.983	2.862
Modified	288	67.5	-16.6	-0.250	-14.0	1.000	0.914	1.749
Lax-Wendroff	2*288	73.7	-14.7	0.062	-7.1	1.002	0.957	1.640
	4*288	76.0	-14.8	0.062	-7.1	1.004	0.976	1.648
	10*288	76.7	-15.4	0.062	-7.1	1.008	0.989	1.704
D_1	48	58.5	-2.0	-3	0	0.442	0.317	0.517
	288	54.2	-2.5	-1.0	0	0.868	0.577	1.052
	2*288	53.9	-2.5	0	0	0.932	0.619	1.126
	4*288	54.5	-2.6	0	0	0.965	0.641	1.163
	10*288	54.7	-2.6	0	0	0.987	0.655	1.186
D_2	48	74.6	-1.5	0	0	0.995	0.847	1.099
	288	56.4	-2.3	0	0	1.000	0.678	1.191
	2*288	55.5	-2.4	0	0	1.000	0.671	1.196
	4*288	55.1	-2.5	0	0	1.001	0.668	1.199
	10*288	55.0	-2.5	0	0	1.001	0.666	1.200
D_3	48	76.9	-1.5	0	0	1.000	0.852	1.102
	288	56.4	-2.3	0	0	1.000	0.678	1.191
	2*288	55.5	-2.4	0	0	1.000	0.671	1.196
	4*288	55.2	-2.5	0	0	1.001	0.668	1.199
	10*288	55.0	-2.6	0	0	1.001	0.666	1.200

Table 4.2. Maximum height, minimum height, radial error in units of grid lengths, angular error in degrees, and conservation properties after one revolution of Crowley's cone test are shown for various schemes. Initially the maximum height is 100 and the minimum is zero.

The D_2 and D_3 schemes are superior to the D_1 scheme since they have smaller height errors, better phase representation and better conservation properties (Table 4.2). The D_3 scheme produces superior results to the D_2 scheme with respect to reduced height errors and improved conservation properties, especially for larger time steps (Table 4.2).

The conservation properties $\frac{\sum \psi_{ij}}{\sum \psi_{ij}(0)}$ and $\frac{\sum |\psi_{ij}|}{\sum |\psi_{ij}(0)|}$ are excellent (Table 4.2) in the D_2 and D_3 schemes. However, the conservation property $\frac{\sum \psi_{ij}^2}{\sum \psi_{ij}^2(0)}$ (Table 4.2) is relatively low (compared to the values obtained for the two Lax-Wendroff schemes) for the semi-Lagrangian schemes. This may be attributed to the bicubic interpolation procedure used at each time step, which spuriously spreads the scalar field over an artificially large region. When the small values at each grid point are squared during the calculation of the conservation property $\frac{\sum \psi_{ij}^2}{\sum \psi_{ij}^2(0)}$, relatively low values are obtained. When smaller time steps are used the effect becomes even more apparent (Table 4.2) because more bicubic interpolations are performed. This represents a further drawback of the semi-Lagrangian schemes, despite the fact that the scalar field is conserved finely.

Figures 4.13a, 4.13b and Table 4.2 suggest that the D_1, D_2 and D_3 schemes are superior to the modified Lax-Wendroff scheme with respect to the occurrence of phase errors. The unpleasant trailing waves present in the Lax-Wendroff simulations are absent in the semi-Lagrangian results. Analysis of the height error in Table 4.2 suggests that the modified Lax-Wendroff scheme preserves the cone height. However, it wrongly creates large negative values for the scalar field (minimum height in Table 4.2). The conservation property $\frac{\sum |\psi_{ij}|}{\sum |\psi_{ij}(0)|}$ indicate that the modified Lax-Wendroff scheme falsely increases the scalar concentration. In this respect the modified Lax-Wendroff scheme is undoubtedly inferior to the D_2 and D_3 schemes.

4.5.2 STRONG DEFORMATIONAL FLOW: SMOLARKIEWICZ'S TEST

As long as the modified Lax Wendroff scheme is applied to a constant velocity field or to smooth non-deformational flow (such as the flow field defined in Crowley's cone test), it provides reasonable results. For deformational flow however, significant differences exist between the behaviour of the modified Lax-Wendroff and the semi-Lagrangian schemes. It is difficult to prove stability of a scheme under conditions of non-uniform flow, since stability features may depend on the structure of the velocity field. Therefore a fixed chosen example, which involves strong deformational flow will be used in this study to evaluate the properties of the various schemes under conditions of non-uniform flow.

Smolarkiewicz (1982) defined an interesting deformational flow pattern to evaluate the performance of his multidimensional generalisation of the Crowley (1968) advection scheme. The challenge is to capture the advection properties of a scalar distribution (initially a cone of height 1 unit and base radius 15 units centred on a square domain with a boundary dimension of $L = 100$ units) in a flow field defined by the stream function:

$$\phi(x, y) = A \sin(kx)\cos(ky)$$

where $A = 8$, $k = \frac{4\pi}{L}$ and the position of the central point on the square is $x = y = 50$. This is also the position of the centre of the initial cone distribution.

The equation for the initial scalar distribution is

$$\psi(x,y) = -\left(\frac{1}{15}\right)\sqrt{(x-50)^2 + (y-50)^2} + 1\,; \quad (x-50)^2 + (y-50)^2 \le 15^2$$

and the velocity field is given by

$$\bar{v} = \left(-\frac{\partial\phi}{\partial y}, \frac{\partial\phi}{\partial x}\right) = [Ak\sin(kx)\sin(ky), Ak\cos(kx)\cos(ky)]$$

Following Smolarkiewicz (1982), $\Delta t = 0.7$ s is chosen, implying that $c\frac{\Delta t}{\Delta x} = 0.7$. Deformation of the velocity field is defined as (Smolarkiewicz, 1982):

$$\mathrm{Def} \equiv \frac{\partial u}{\partial x} - \frac{\partial v}{\partial y}.$$

As a result of the inequality $\mathrm{Max(Def)}\Delta t = 1.4 > 1$, deformation can be considered as strong (Smolarkiewicz, 1982).

Isolines of the stream function (blue and green lines) and height level lines of the initial scalar distribution (red contours) are illustrated in figure 4.14. The initial scalar distribution is displayed in three-dimensions in figure 4.15. The velocity field is constructed in terms of a set of square boxes with symmetrical vortices. Rotation in the blue vortices in figure 4.14 is clockwise while the green vortices represent counter-clockwise rotation. Each vortex occupies a square of side length 25 units.

The radius of the base of the cone is slightly greater than the radius of the vortices (figure 4.14), so that at the initial time the cone distribution covers areas in six vortices. It is expected that the solution, after a long enough integration period, will be of such a nature that two symmetrical pieces of the cone will move into the area of the two central vortices (Smolarkiewicz, 1982).

Staniforth et al. (1987), pointed out that fluid elements are constrained to move along the streamlines for this problem and cannot escape from the vortex in which they are found at the initial point in time (because they cannot cross the bounding streamline of the vortex). Since the initial scalar distribution is nonzero over six vortexes, it will be nonzero over these six vortexes for all time. A second consequence of this property of fluid elements is that for each of the four peripheral vortices the solution should be identically zero everywhere inside the streamline that is tangent to the base of the cone at initial time (see figure 4.14). Thus, for each of these four vortices the nonzero part of the solution is confined to a narrow region close to its boundary.

Corners and centres of vortices are stagnation points of the flow. The corners are saddle points of the stream function, whereas the centres are local extrema. The solution of the advection problem at any stagnation point retains its initial value for all time intervals. However fluid elements in an infinitesimally small neighbourhood of saddle points are transported along their initial streamline and replaced by an upstream fluid element carrying a different value of the scalar field. Consequently, an increasing gradient in the scalar distribution develops at saddle points (Staniforth et al., 1987).

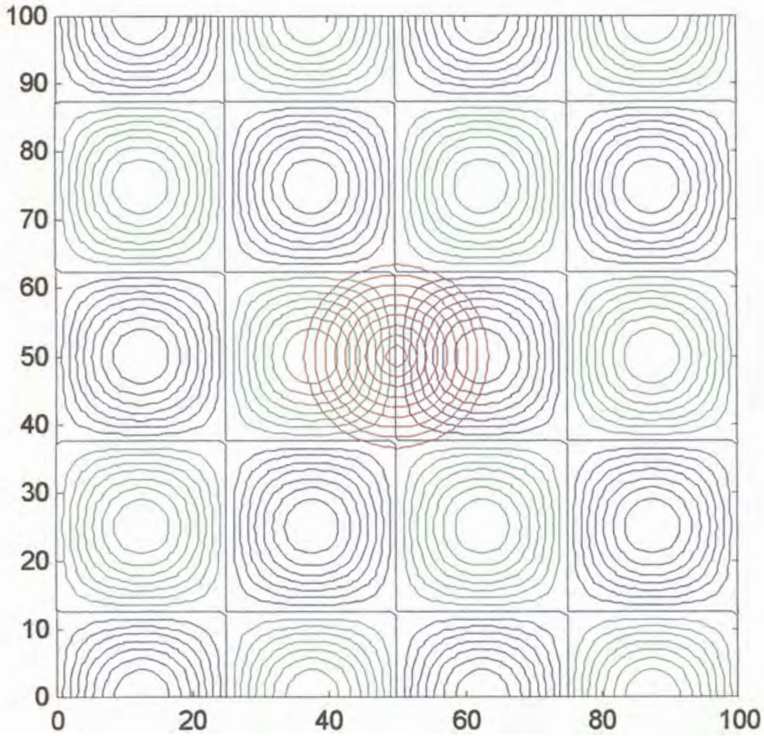

Figure 4.14 Isolines of the streamfunction for Smolarkiewicz's test with the initial scalar distribution (red contours) in the form of a cone of height 1 unit and base diameter 30 units superimposed. Rotation of the blue vortices is clockwise while the green vortices represent counter-clockwise rotation.

There have been attempts to find the analytic solution of Smolarkiewicz test problem. Staniforth et al. (1987) illustrated that when the position of a fluid element at time t_0 is known, its position at time t may be found in terms of Jacobian elliptic functions. Since the quantity ψ is conserved along a trajectory, ψ can be predicted at time t, as long as ψ is known at $t = t_0$ (Staniforth et al., 1987). However, Leonard et al. (1996) point out that the solution presented by Staniforth et al. (1987) deals with nodal-point values on a highly variable grid with drastically increased resolution in regions of large gradient in the advected field. Instead of working with this analytic solution, Leonard et al. (1996) preferred to use a highly accurate fourth-order Runge-Kutta scheme with a small time step to find the initial position (and hence the initial ψ value) of a fluid element located at position (x_1, y_1) at time t. In this section the results of the various schemes will be evaluated against the expected qualitative behaviour of the true solution.

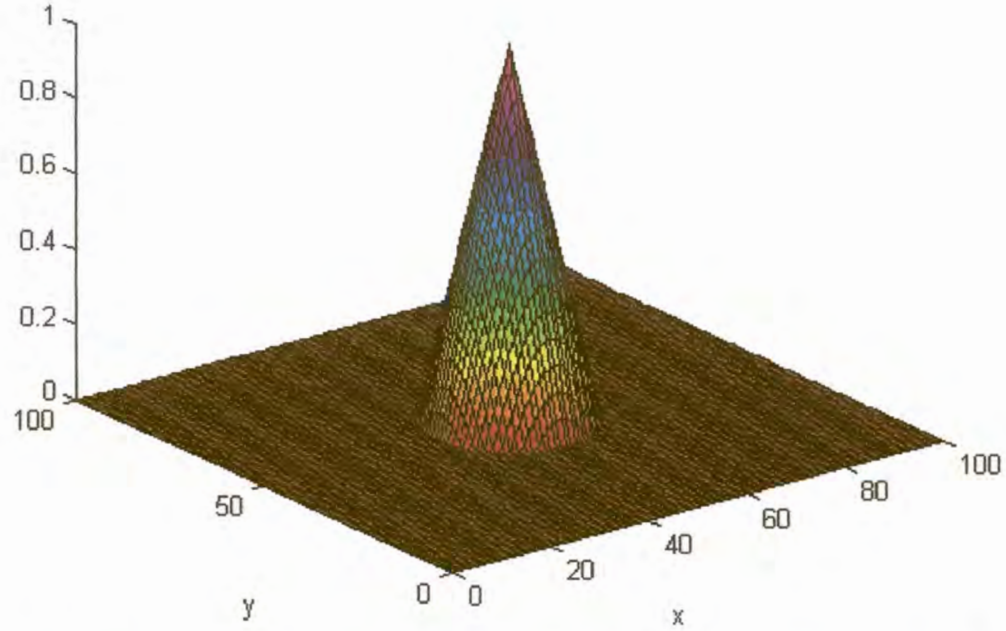

Figure 4.15 Initial cone configuration in 3-dimensions for Smolarkiewic's test. The cone has a height of 1 unit, base diameter of 30 units and is centred at position (50,50).

The numerical solutions obtained after 19, 38, 57, 75, 377 and 3768 iterations (using $\Delta t = 0.7$ s) with the D$_3$ scheme are displayed in figures 4.16a to 4.16f. respectively. The number of iterations given above closely correspond to the times t=T/200, t=T/100, t=3T/200, t=T/50, t=T/10 and t=T where T=2637.6 s is the final time of integration used by Smolarkiewicz (1982). Staniforth et al. (1987) give presentations of the analytical solution of Smolarkiewicz's problem at these time steps.

In figure 4.16a it can be seen that the scalar distribution inside each of the two "main vortexes" starts to rotate about the vortex centres. Maximum quantities move away from the domain centre towards the stagnation points in the positive y direction. The distribution has a left/right symmetry. The behaviour of the numerical solution in figure 4.16a (after 19 iterations) is thus in complete harmony with the expected qualitative behaviour of the true solutions that was discussed earlier.

The fragments of the cone that were initially inside the four peripheral vortices move along their trajectories near the perimeter (figure 4.16b, 38 iterations). Simultaneously, a strong gradient in the scalar distribution is developing near the saddle points of the two "main vortices". Figure 4.16c (57 iterations) reveals the first qualitative difference between the numerical solution and the true solution: Negative scalar quantities exist in the numerical solution (black contours in figure 4.16c). Negative weights used in the bicubic interpolation procedure possibly contribute to this defect in the numerical solution.

After 75 iterations (figure 4.16d) the negative scalar distribution in the numerical simulation has increased slightly. The fact however, that the true solution remains confined to the six vortexes that contained the initial cone distribution and the fact that the scalar distribution cannot cross the bounding streamlines, are well represented in the simulation with the D_3 scheme. The scalar quantity starts to spiral in towards the centres of the two main vortexes.

In figure 4.16e the scalar distribution is divided into two symmetrical pieces, with maximum concentrations located within the two "main vortexes", as can be expected. Although this pattern is still preserved in figure 4.16f there is a sudden outbreak of negative scalar quantities over some of the peripheral vortexes. The negative quantities also succeeded in crossing the bounding streamlines and intruding into the centres of some of the peripheral vortexes, which is inconsistent with the expected qualitative behaviour of the true solution.

The numerical solution depicted in figures 4.16a to 4.16f closely corresponds to the analytical solution presented by Staniforth et al. (1986). The solution remains stable although some of the scalar distribution eventually escapes into the peripheral vortices (figure 4.16f). The D_1 and D_2 schemes qualitatively illustrate the same behaviour as the D_3 scheme (not shown). The conservation properties of the D3 scheme are slightly superior to that of the D_2 scheme (Table 4.3). The conservation properties of the D_1 scheme are inferior to those of the D_2 and D_3 schemes for all cases expect for the final case of 3768 iterations in Table 4.3. The two latter schemes spuriously create more of the scalar quantity when $t \to T$, especially in the form of negative quantities intruding some of the peripheral vortices (figure 4.6bf). The reason for this interesting behaviour (and why it is absent in the D_1 solution) is not presently known.

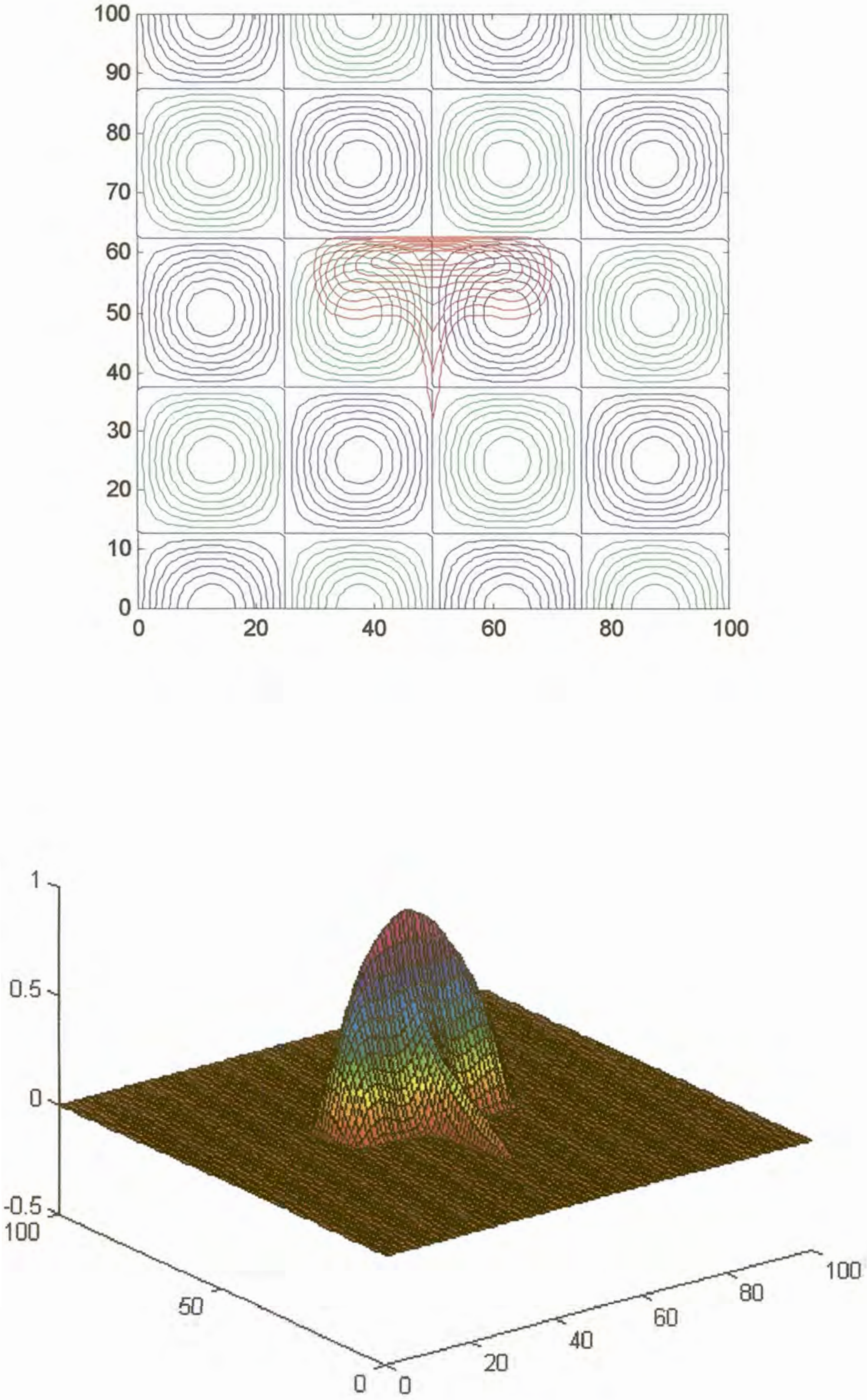

Figure 4.16a The scalar distribution in Smolarkiewicz's deformational flow after 19 iterations ($\Delta t=0.7$ s) with the D_3 scheme.

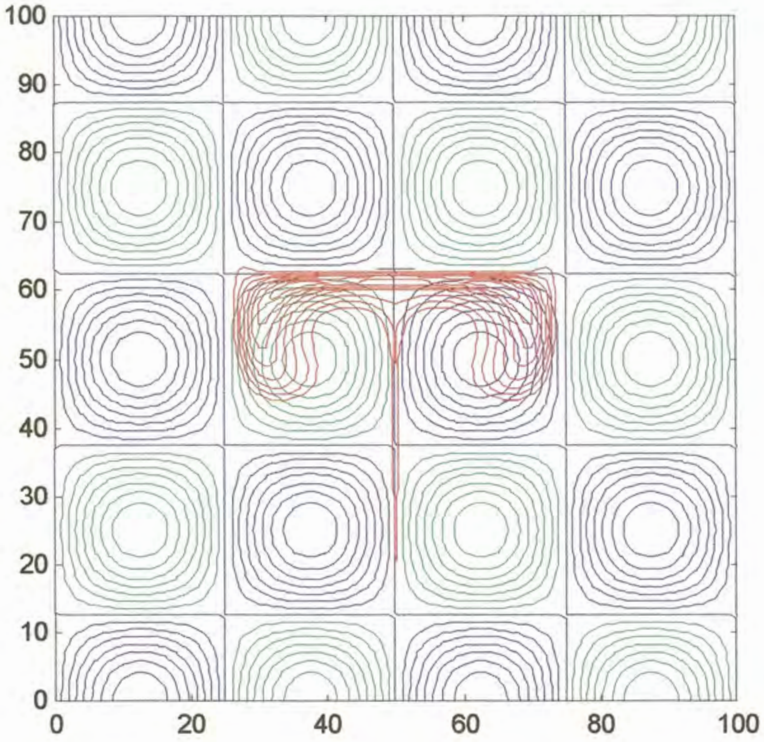

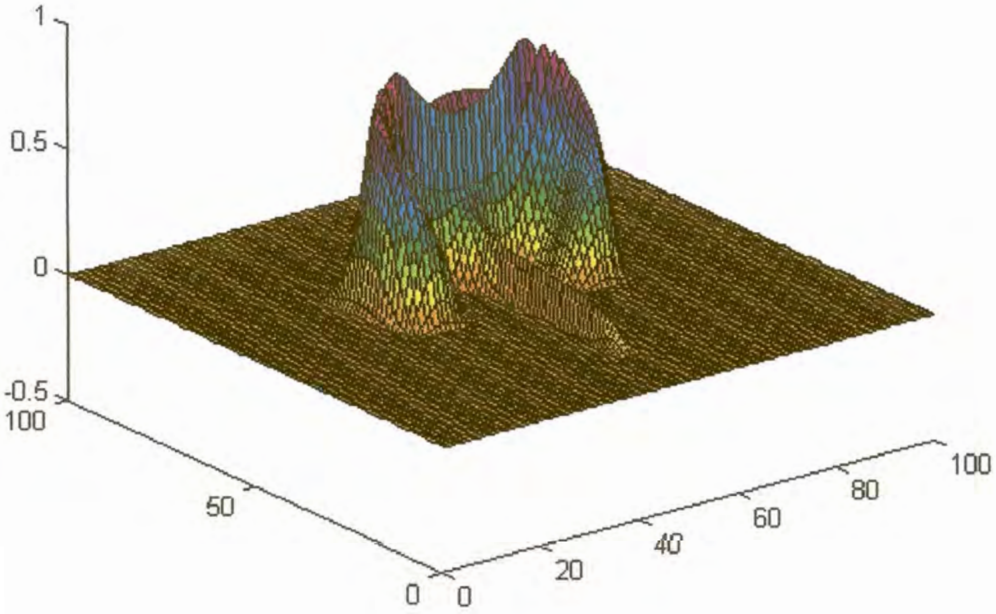

Figure 4.16b The scalar distribution in Smolarkiewicz's deformational flow after 38 iterations ($\Delta t=0.7$ s) with the D_3 scheme.

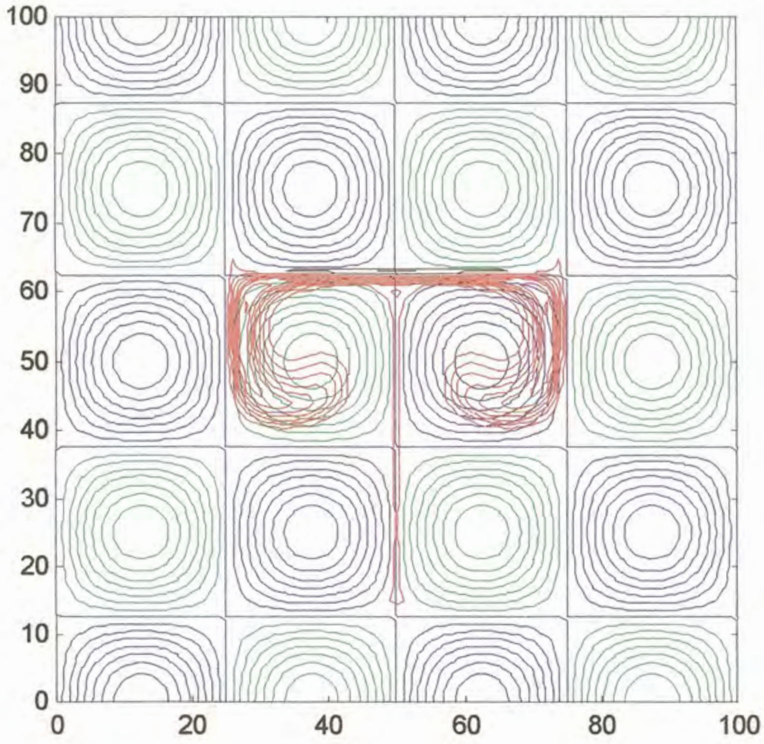

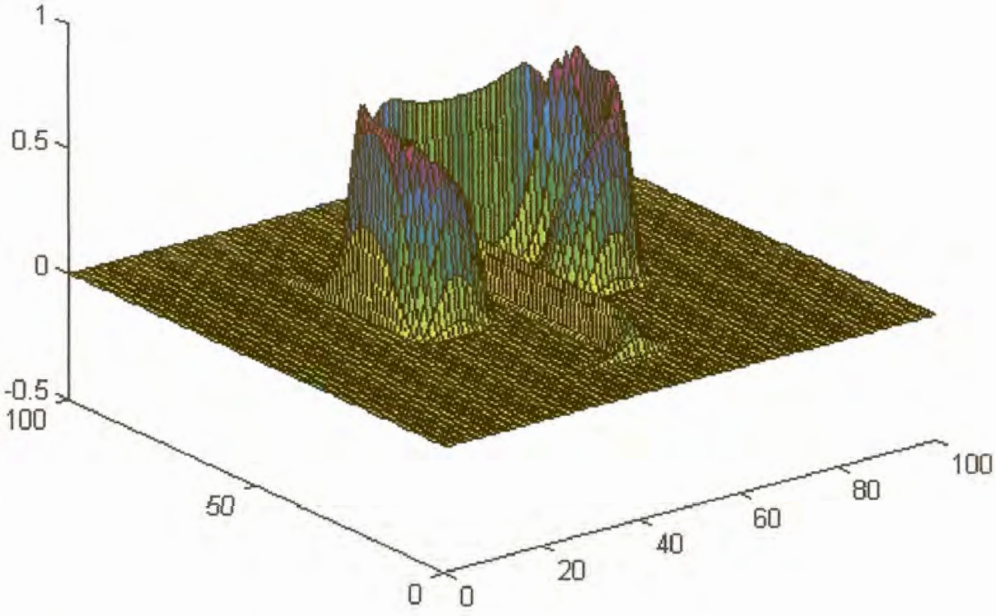

Figure 4.16c The scalar distribution in Smolarkiewicz's deformational flow after 57 iterations ($\Delta t = 0.7$ s) with the D_3 scheme.

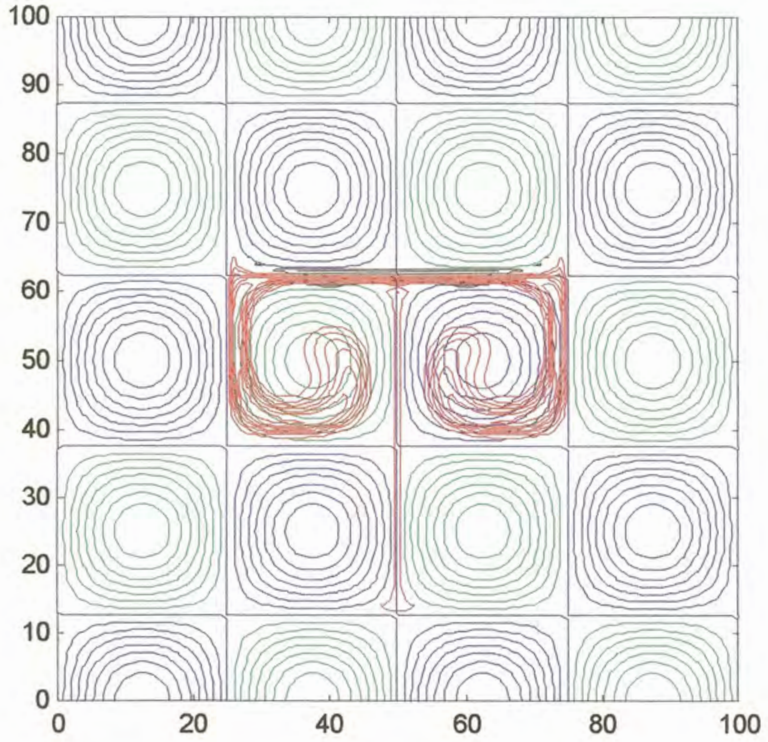

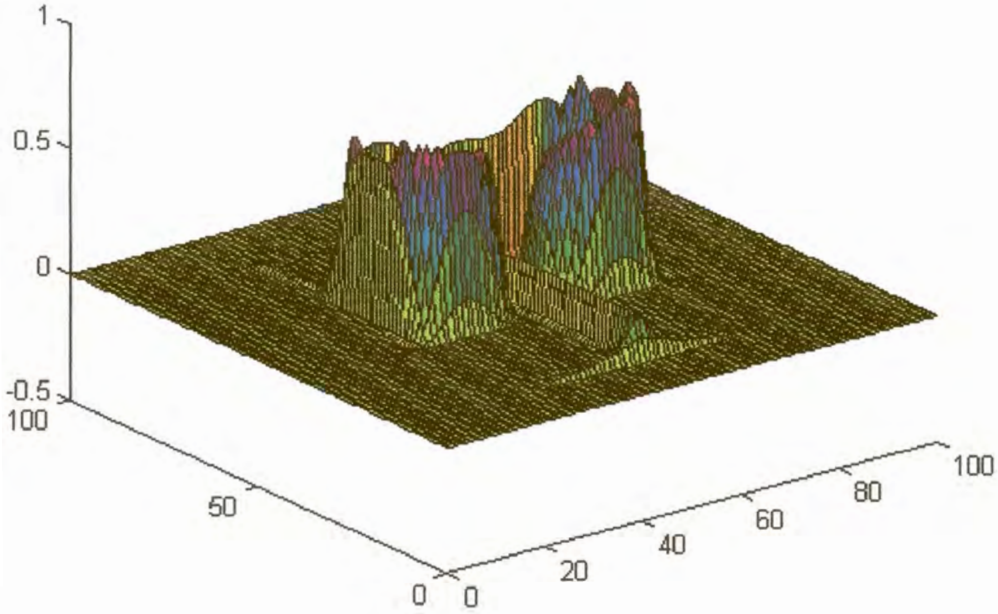

Figure 4.16d The scalar distribution in Smolarkiewicz's deformational flow after 75 iterations ($\Delta t = 0.7$ s) with the D_3 scheme

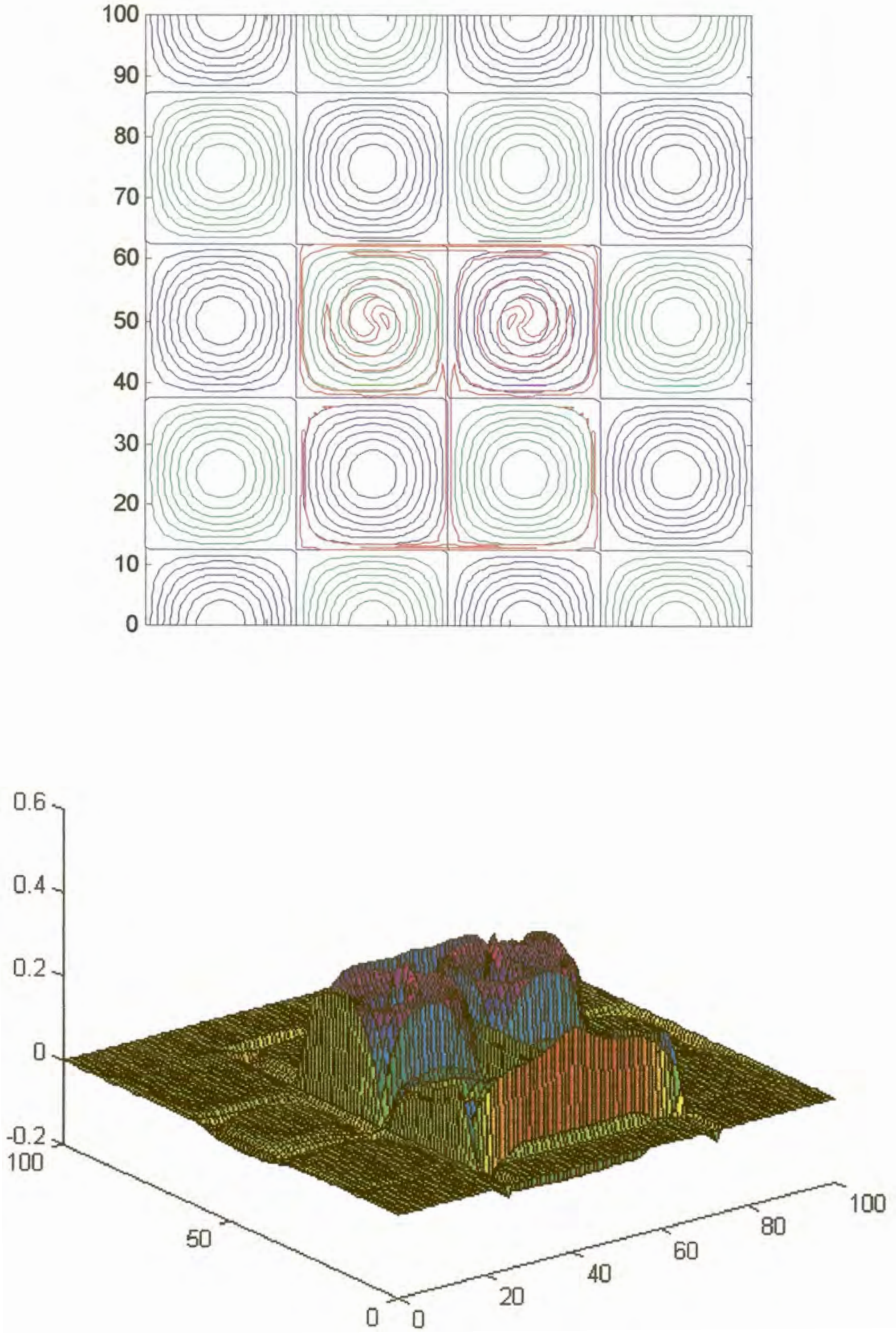

Figure 4.16e The scalar distribution in Smolarkiewicz's deformational flow after 377 iterations ($\Delta t = 0.7$ s) with the D_3 scheme

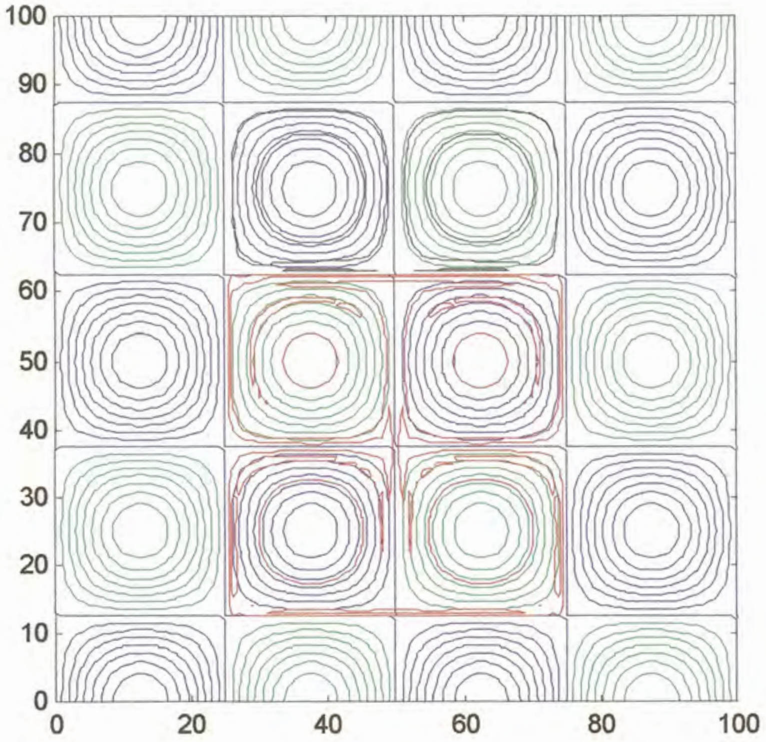

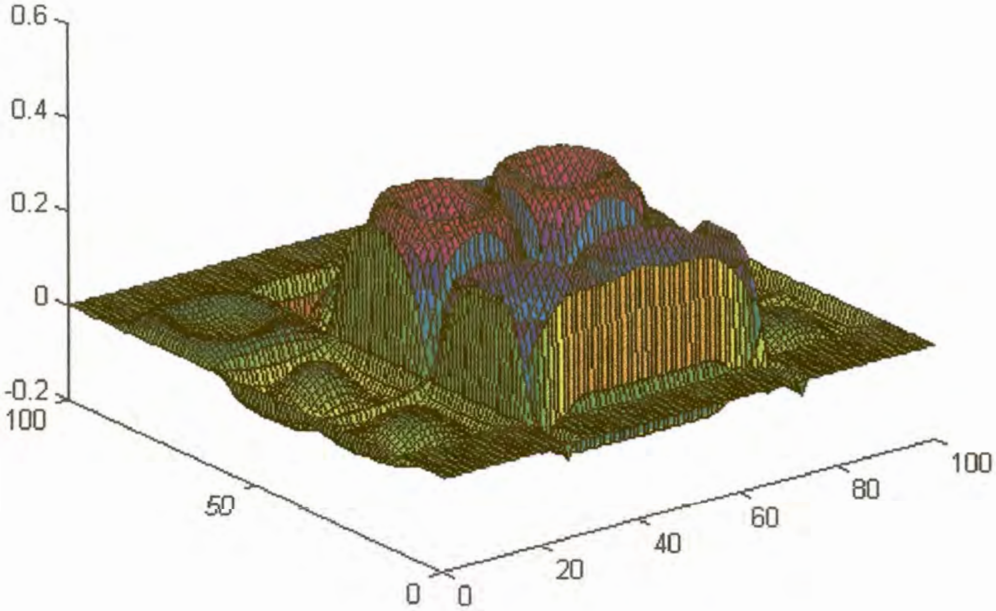

Figure 4.16f The scalar distribution in Smolarkiewicz's deformational flow after 3768 iterations ($\Delta t=0.7$ s) with the D_3 scheme

The Leapfrog scheme and both Lax-Wendroff schemes spectacularly fail Smolarkiewicz's test. After only 57 iterations, growing instabilities can be observed in the numerical solutions of all three these schemes. This can be seen from the conservation property $\frac{\sum|\psi_{ij}|}{\sum|\psi_{ij}(0)|}$ in Table 4.3, which for all three finite difference schemes rapidly increases as time increases. The instabilities grow exceptionally fast in the numerical solution of the Leapfrog scheme.

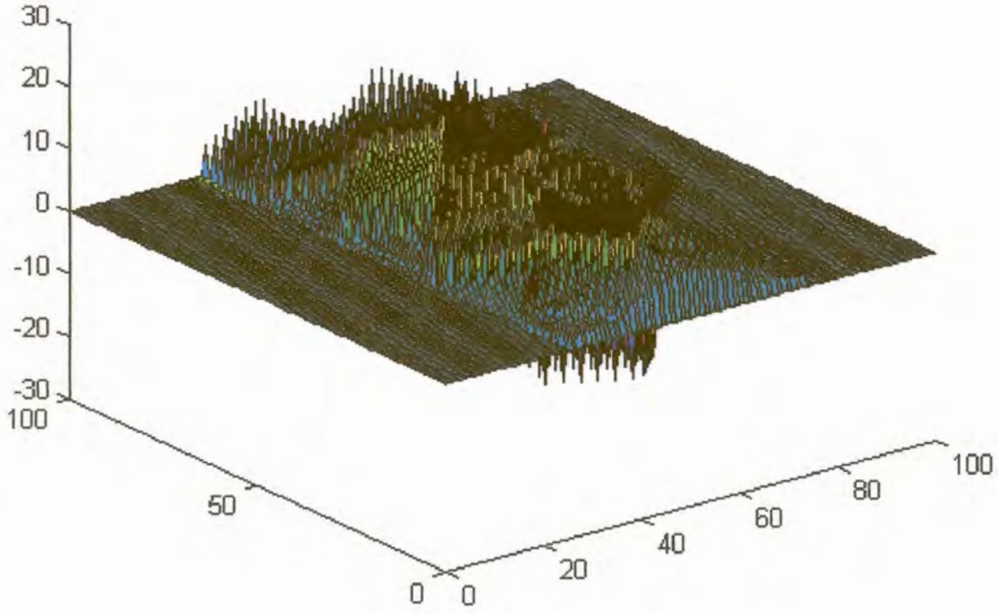

Figure 4.17 The scalar distribution in Smolarkiewicz's deformational flow after 377 iterations ($\Delta t = 0.7$ s) with the leapfrog scheme.

Figure 4.17 show the solution obtained from the leapfrog scheme after 377 iterations. Figure 4.18 shows the corresponding solution produced by the modified Lax-Wendroff scheme. The solution obtained from the Lax-Wendroff scheme (not shown) is qualitatively similar to that of the modified Lax-Wendroff scheme. Conservation properties of the Lax-Wendroff scheme are only slightly inferior to those of the modified Lax-Wendroff scheme (Table 4.3). For Smolarkiewicz's test (strong deformational flow) the modified Lax-Wendroff scheme does not offer significant advantages over the computationally more efficient Lax-Wendroff scheme. In contrast to the finite

Scheme	Number of iterations	$\frac{\sum \psi_{ij}}{\sum \psi_{ij}(0)}$	$\frac{\sum \psi_{ij}^2}{\sum \psi_{ij}^2(0)}$	$\frac{\sum \lvert\psi_{ij}\rvert}{\sum \lvert\psi_{ij}(0)\rvert}$
Leapfrog	19	1.000	1.014	1.034
	38	1.000	1.097	1.164
	57	1.000	1.466	1.671
	75	1.000	2.576	2.719
	377	6.107	1936.076	109.665
	3768	Unstable	Unstable	Unstable
Lax-Wendroff	19	1.000	1.007	1.022
	38	1.000	1.042	1.081
	57	1.000	1.123	1.255
	75	1.000	1.320	1.530
	377	0.959	2.478	3.156
	3768	0.861	26.58	12.401
Modified	19	1.000	1.007	1.022
Lax-Wendrof	38	1.000	1.041	1.081
	57	1.000	1.123	1.255
	75	1.000	1.321	1.530
	377	0.959	2.476	3.154
	3768	0.862	26.946	12.519
D_1	19	1.001	1.008	1.010
	38	1.004	1.025	1.041
	57	1.012	1.076	1.122
	75	1.017	1.081	1.199
	377	1.016	0.468	1.526
	3768	1.028	0.446	1.873
D_2	19	1.000	0.998	1.009
	38	1.002	1.009	1.043
	57	1.009	1.060	1.125
	75	1.013	1.058	1.200
	377	1.015	0.493	1.407
	3768	1.154	0.961	2.792
D_3	19	1.000	0.999	1.009
	38	1.002	1.010	1.043
	57	1.009	1.061	1.125
	75	1.013	1.058	1.200
	377	1.015	0.493	1.407
	3768	1.151	0.954	2.780

Table 4.3 Conservation properties of various schemes for Smolarkiewic's test, expressed as a function of the number of iterations (Δt=0.7 s).

difference schemes, the D_N schemes all remain stable during the integration. Compared to the finite difference schemes, the conservation properties of the D_N schemes (in Table 3) are excellent. For Smolarkiewicz's test of strong deformational flow the D_N schemes are by far superior over the finite difference schemes studied.

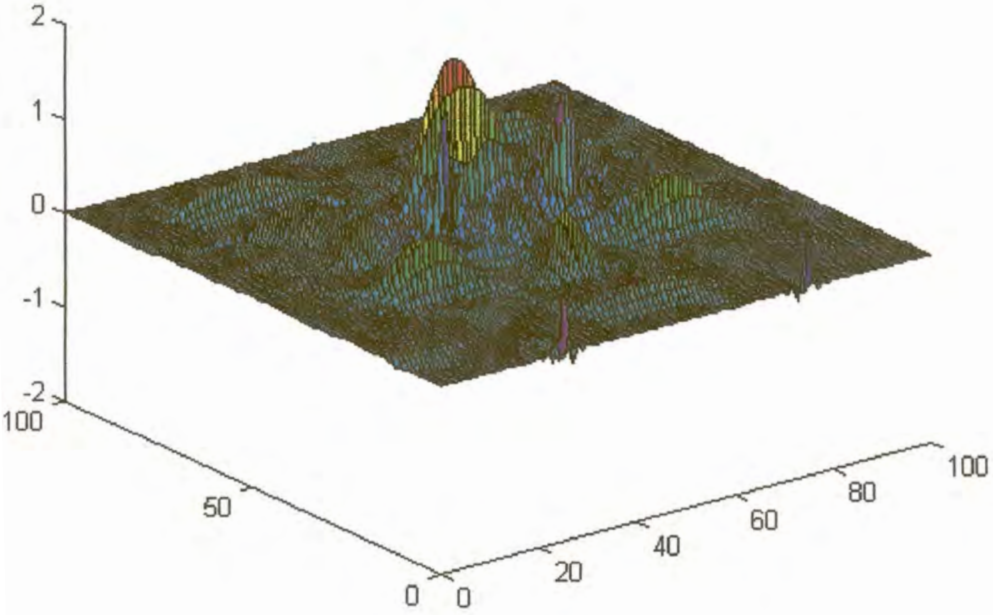

Figure 4.18 The scalar field in Smolarkiewicz's deformational flow after 377 iterations ($\Delta t = 0.7$ s) with modified Lax-Wendroff scheme.

CHAPTER 5

JANUARY AND JULY CLIMATE SIMULATIONS OVER SOUTHERN AFRICA USING DARLAM

5.1 INTRODUCTION

Chapter 5 describes the results of climatological simulations over the SADC region with DARLAM. The LAM is one-way nested within simulations of selected months (January and July) from a long seasonal varying simulation of the CSIRO9 AGCM (both models are discussed in Chapter 3). The relatively coarse resolution (spectral resolution of R21) AGCM with 9 levels in the vertical is used to provide boundary conditions to DARLAM, which is run at a horizontal grid resolution of 60 km with 18 levels in the vertical. The AGCM supplies large-scale synoptic forcing to DARLAM through its lateral boundaries. DARLAM's dynamical formulation and physical parameterisation schemes are similar to those used in the AGCM but it's higher resolution adds significant smaller-scale detail to the coarser simulation of the AGCM. This chapter will illustrate that the additional detail provides improved simulation results, when compared to AGCM results over most regions of the LAM domain.

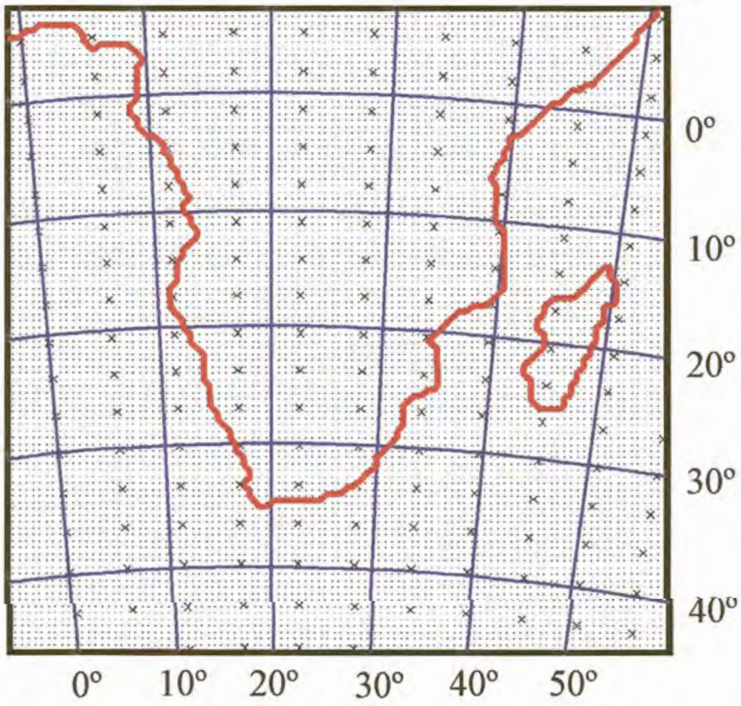

Figure 5.1 DARLAM domain used for the simulations over the SADC region. The 60 km x 60 km spaced nested model grid points (on a Lambert conformal projection) are indicated by dots. Gaussian grid points of the R21 CSIRO9 AGCM are indicated by crosses.

The DARLAM domain covers the entire SADC region. Therefore, an important feature of the simulations is the inclusion of extensive regions north and south of the equator (see section 2.3.1). It might be expected that DARLAM would perform better over mid-latitude than tropical regions. Weather systems generally move slower in tropical regions and internal quasi-stationary systems may evolve within the nested model domain independent of the boundary forcing (Walsh and McGregor, 1995, also see section 2.3.1). It is also worthwhile to note that large regions of southern Africa are influenced by both tropical and mid-latitude systems. The LAM's domain size (figure 5.1) is considerably larger and both the horizontal and vertical resolution much finer than used in any previously performed climate simulations over the SADC region. The results presented here also include the first July climate simulations over the SADC region.

The DARLAM simulations of climate for January (the peak rainfall month over southern Africa) and July are qualitatively compared with observations as well as results from the AGCM. Of interest is the extent to which boundary forcing supplied by the AGCM influences nested model simulations, as well as the extent to which the higher resolution of the nested model results in improved climate simulations of surface and lower-tropospheric conditions over the region.

5.2 EXPERIMENTAL DESIGN AND VALIDATION DATA

A one-way nesting technique is used in these experiments. Every 12 hours lateral boundary conditions are supplied by the CSIRO9 AGCM. At each time step the outermost DARLAM boundary grid rows are relaxed toward interpolated AGCM values. The nesting procedure of Davies (1976) is used, but with exponentially decreasing weights. Initial atmospheric conditions for DARLAM (including soil moistures) are supplied by the forcing AGCM and SSTs are prescribed every 12 hours by the AGCM.

Nine separate 30-day simulations have been performed for both January (mid-summer) and July (mid-winter). The averages of these simulations constitute the model climatology for these months. The 30-day simulations incorporated both diurnal and seasonally varying radiation but were initialised separately with output fields taken from the CSIRO9 AGCM. No vertical-mode initialisation has been performed. A short spin-up period of about two days allowed for the moisture cycle to reach equilibrium. Similar experiments over the Australian region indicated that the spin-up process has a negligible effect on the DARLAM climate (Walsh and McGregor, 1995). For surface pressure and temperature the boundary fields are altered to compensate for any differences in height that may arise in the interpolated topography of the AGCM relative to DARLAM.

In this study January resembles mid-summer (austral summer) conditions, since it has been shown that most of southern Africa receives a pronounced summer rainfall maximum during January (Tyson, 1986). July represents mid-winter conditions. Mean circulation, temperature and rainfall fields as simulated by both the AGCM and LAM are compared to observed fields. Observed mean sea-level pressure (MSLP), 10 m u and v wind components, 2m-temperature and rainfall were obtained from 4-hourly NCEP (National Centre for Environmental Prediction) reanalysis data (Kalnay et al., 1996). The fields constitute 40-year (1958-1998) mean monthly climatologies for January and July on a 2.5°x 2.5° grid resolution. The relatively low spatial resolution of the observed data compared to the 60 km resolution of DARLAM renders the data unsuitable for quantitative model verification.

DARLAM simulations has been performed on a Pentium III computer with two 550 MHz processors. It took 11-minutes (CPU time) to simulate a model day at 60 km resolution with 18 levels in the vertical. An advective time step of 15 minutes was used.

5.3 MODEL TOPOGRAPHY

The interior of South Africa is characterised by an elevated plateau with altitudes in excess of 1000 m. Maximum altitudes in excess of 3500 m occur along the South African eastern escarpment, as well as over Tropical East Africa. The coastal margins along the east and south-east coast of southern Africa are narrow and marked by steep topographic gradients. The R21 spectral resolution of the CSIRO9 AGCM uses a significantly smoothed topography as lower altitude boundary (figure 5.2a). The plateau is narrow and maximum altitudes are under-estimated by as much as 2500 m. Topographic gradients along the escarpment are also very gentle (figure 5.2a). In the AGCM's representation the topography of Madagascar is poorly resolved and extremely smooth over the entire island. Islands such as Mauritius and La Reunion are not even captured by the AGCM topography. The spectral method requires that the surface topography is spectrally fitted to a wave resolution of R21. The initial observed topography consists of a 1°x1° data set that is spatially averaged to the 64x56 global Gaussian grid of the CSIRO9 AGCM, and then spectrally resynthesized to R21 resolution (McGregor et al., 1993a). A consequence of this procedure is non-zero and even negative sea elevation (blue regions in figure 5.2a) which is caused by the Gibbs phenomenon (McGregor et al., 1993a).

With a horizontal resolution of 60 km, DARLAM provides a more detailed representation of observed regional topographic features over southern Africa (figure 5.2b). More realistic maximum elevations occur over the escarpment of south-eastern South Africa (in excess of 2400 m above sea level) and Tropical East Africa (in excess of 3000 m above sea level). In general, DARLAM contains much more detail at 60 km resolution than found in the associated AGCM topography field, for example features such as steep topographic gradients along the southern African escarpment and the Namibian highlands are well captured. The eastern mountain ranges of Madagascar are more obvious and realistic. Even smaller islands such as Mauritius, La Reunion and the Comoros are visible in the DARLAM topography field (not shown). This is a significant improvement on the AGCM topography.

Experiments performed over Australia (McGregor and Walsh, 1993) indicated that climate simulations by LAMs are significantly improved by a better representation of topography (also see Chapter 3).

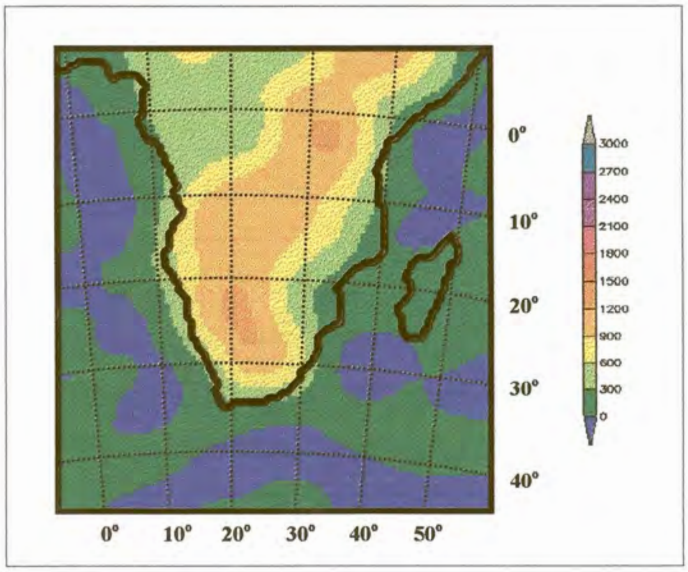

Figure 5.2a CSIRO AGCM representation of topography at R21 spectral resolution over the SADC region. The contour interval is 300 m. Note the smoothed elevation over land and negative elevation over the oceans.

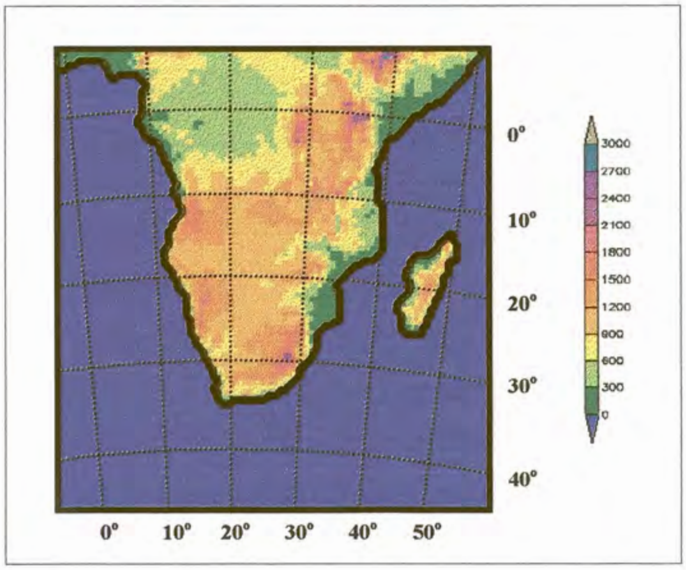

Figure 5.2b DARLAM representation of topography at a 60 km grid point resolution over the SADC region. The contour interval is 300 m. The additional detail is a significant improvement over the AGCM topography.

5.4 MODEL OUTPUT RESULTS

5.4.1 MEAN SEA-LEVEL PRESSURE

Characteristic features of the observed mean sea-level pressure (MSLP) distribution over the SADC region and adjacent oceans are illustrated in figures 5.3a (January) and 5.3b (July).

The January MSLP distribution over the SADC region is characterised by a deep continental low-pressure system (heat low) located at 25°S over Botswana and Namibia and two well-defined anticyclones over the oceans adjacent to the subcontinent (figure 5.3a). A well-developed meridional pressure gradient is present to the south of South Africa where the pressure drops toward the circumpolar trough. Lower pressures occur over the tropical subcontinent during January (figure 5.3a), which indicate the location of the southern extension of the Intertropical Convergence Zone (ITCZ). The relative higher MSLP recorded over south-eastern South Africa and eastern Madagascar during January (figure 5.3a) are the result of migrating high-pressure systems that frequently ridge to the south of the African continent during summer seasons.

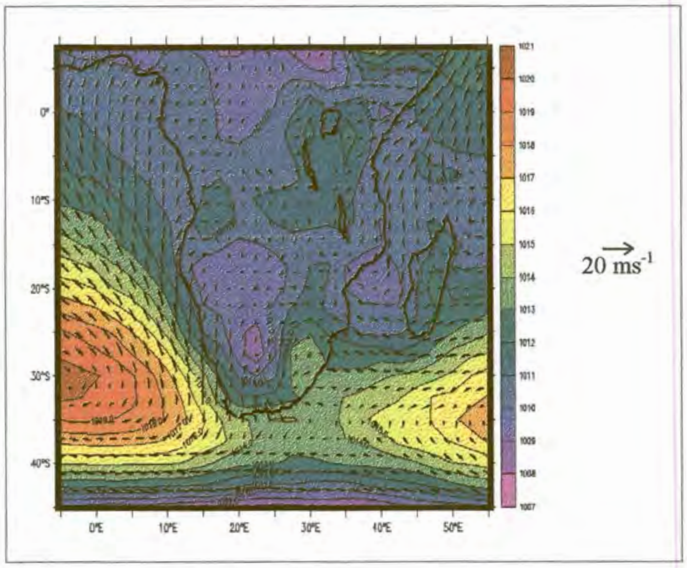

Figure 5.3a Observed mean sea-level pressure (MSLP) measured in hPa and wind vectors (at 10 m altitude) meassured in ms^{-1} for January as obtained from a 40-year (1958 to 1998) NCEP reanalysis climatology. The pressure contour interval is 1 hPa.

During the austral winter (July) the observed oceanic anticyclones intensify and shift northward. At the same time a well-developed high-pressure belt develops over the subcontinent (figure 5.3b). The meridional pressure gradient to the south of South Africa increases as a result of the deeper circumpolar trough, causing westerly winds to intensify over this region. Over tropical regions south of the equator pressures are generally higher in association with the northward propagation of the ITCZ during winter.

The semi-stationary low-pressure cell (a trough in July) present in the NCEP reanalysis field over the Mozambique channel (figures 5.3a and 5.3b) can be regarded as a giant lee low that originates downwind of the eastern Madagascar mountain range in the persistent easterly wind flow (wind vectors in figure 5.3a and 5.3b). The amplitude of this trough and its southward extent decrease in the austral winter (fig 5.3b). The increased amplitude and greater southward extent during January is likely to result from the observed southward shift of the south-easterly trade wind regime during the austral summer, in association with the usual simultaneous occurrence of relative higher SSTs in the Mozambique channel.

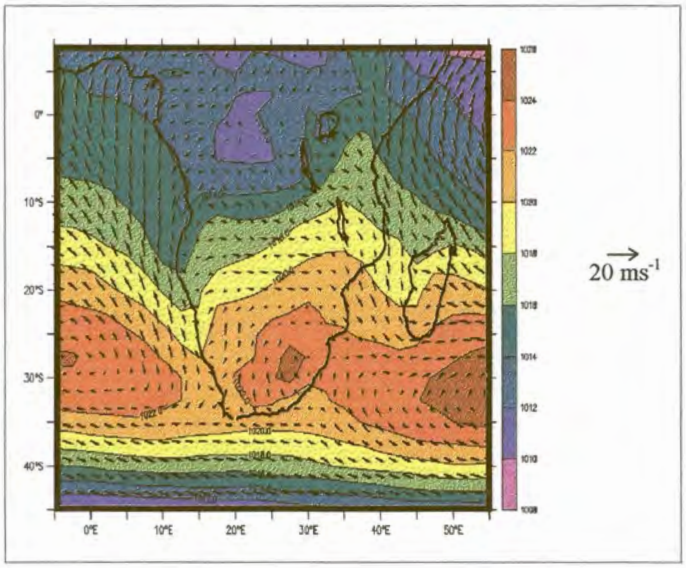

Figure 5.3b Observed mean sea-level pressure (MSLP) measured in hPa and wind vectors (at 10 m altitude) measured in ms^{-1} for July as obtained from a forty year (1958 to 1998) NCEP reanalysis climatology. The pressure contour interval is 2 hPa.

The general synoptic-scale features of the observed MSLP are adequately captured in the CSIRO9 AGCM simulations for January and July (figures 5.3c and 5.3d).

In the January simulation (figure 5.3c), the low-pressure cell over Namibia and Botswana is located further to the north and west than observed, although the intensity of the cell is well reproduced. The relative position (also meridional position) of the oceanic anticyclones is well captured. The amplitudes of both these cells however, are overestimated. The meridional pressure gradient to the south of South Africa, as simulated by the CSIRO9 AGCM, closely corresponds to the observed gradient. The CSIRO9 AGCM overestimates MSLPs over tropical regions and fails to reproduce the presence of lower pressures in the Mozambique Channel. MSLPs over the Mozambique Channel are severely overestimated (by as much as 4 hPa). The CSIRO9 AGCM also fails to capture the pattern of relatively higher MSLPs over the south-eastern part of South Africa and eastern Madagascar.

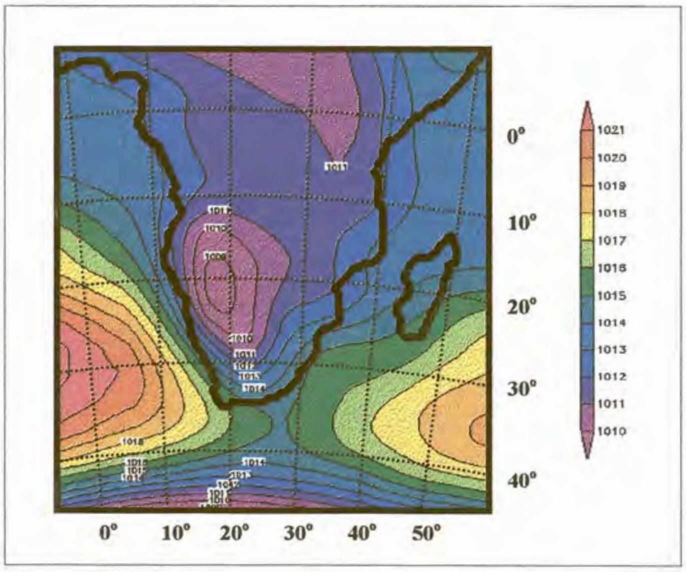

Figure 5.3c Mean sea-level pressure (MSLP) measured in hPa for January as simulated by the CSIRO9 AGCM. The pressure contour interval is 1 hPa.

The CSIRO9 AGCM successfully simulates the observed northward shift and intensification of the subtropical anticyclones in July, as well as the tighter meridional pressure gradient associated with the deeper circumpolar trough (figure 5.3d). The simulation of amplitudes of the broader July MSLP pattern is weaker when compared to the simulation of January amplitudes. In particular, the intensity of the Indian Ocean high-pressure system is underestimated by more than 4hPa. As found in the January simulations, the CSIRO9 AGCM simulates higher than observed MSLPs over the tropical regions and again fails to simulate the trough in the Mozambique Channel. The July CSIRO9 AGCM simulation however, does capture the higher pressures over tropical regions south of the equator (relative to January) suggesting that the model succeeds in simulating the northward displacement of the ITCZ during the austral winter.

DARLAM is forced at the lateral edges of its domain by boundary conditions supplied by the CSIRO9 AGCM. The January and July MSLP patterns as simulated by the LAM (Figure 5.3e and 5.3f) are therefore similar to those of the CSIRO9 AGCM. As a matter of fact the two model simulations have much in common, especially over maritime regions where the higher resolution surface topography of the LAM is absent. The lower intensities of the two subtropical oceanic high-pressure systems, as simulated by DARLAM for

January, are slightly more accurate than in the corresponding CSIRO9 AGCM simulations (compare figures 5.3a, 5.3c and 5.3e).

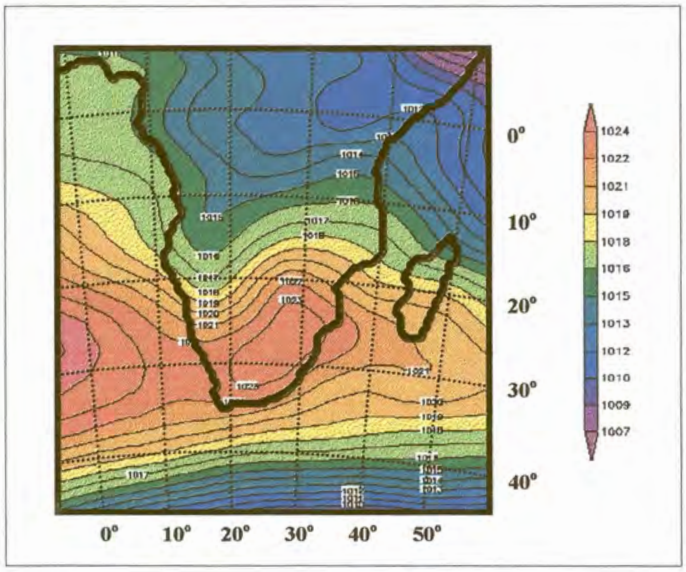

Figure 5.3d Mean sea-level pressure (MSLP) measured in hPa for July as simulated by the CSIRO9 AGCM. The pressure contour interval is 1 hPa.

The DARLAM continental low over the western subcontinent is larger in extent and slightly deeper than found in CSIRO9 AGCM simulations. The low simulated by DARLAM also extends further to the south and east. The centre of the low (figure 5.3e) is in close correspondence with the observed position (figure 5.3a), which represents a significant improvement over the AGCM simulation (figure 5.3c).

The DARLAM simulations of MSLP over southern Africa and Madagascar contain far more detail than the corresponding CSIRO9 AGCM simulations. DARLAM adequately simulates the observed pattern of high-pressure intrusion over the south-eastern parts of South Africa and Madagascar (compare figures 5.3a and 5.3e). This may be explained by the fact that the high resolution topography in DARLAM enables the model to capture low-level mass convergence along the south-eastern escarpment of South Africa and Madagascar when high pressure systems ridge to the south of Africa. The AGCM, with its smooth topography, is unable to capture this pattern (compare figures 5.3c and 5.3a).

Another outstanding feature in the DARLAM simulation is the reproduction of the observed low in the Mozambique Channel. Altitudes in the DARLAM topography over Madagascar are in excess of 1200 m (figure 5.2b), which is sufficient to capture the development of a gigantic lee low that is located downwind of the Madagascar mountain range. DARLAM underestimates the intensity of the low, however. This low does not exist in the CSIRO9 AGCM simulation probably as a result of the smoothed topography (figure 5.2a).

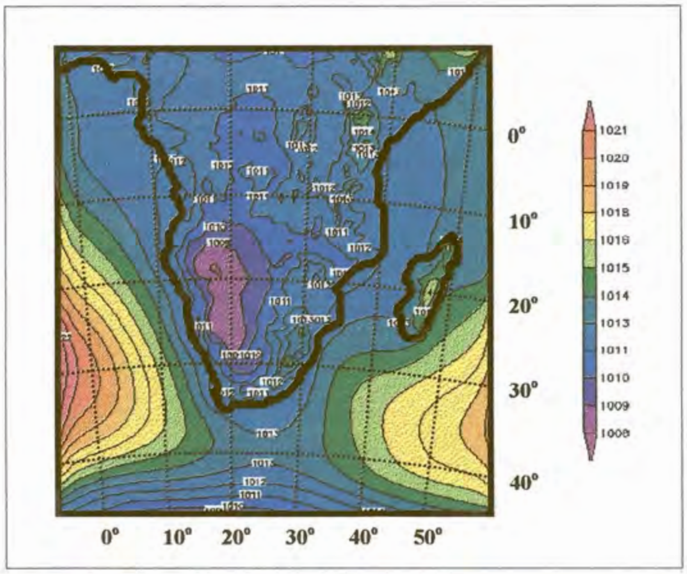

Figure 5.3e Mean sea-level pressure (MSLP) measured in hPa for January as simulated by DARLAM. The pressure contour interval is 1 hPa.

July MSLP simulations by DARLAM (figure 5.3f) indicate an underestimation of the intensity of the Indian Ocean high-pressure system similar to that of the forcing AGCM. Over tropical regions DARLAM generally simulates lower MSLPs (that are in close correspondence with the observed pattern) than the AGCM. DARLAM severely underestimates the intensity of the subtropical high-pressure belt over the African continent (by as much as 6 hPa), as well as the intensity of the meridional pressure gradient to the south of Africa. In this respect DARLAM simulations are inferior to the associated CSIRO9 AGCM simulations.

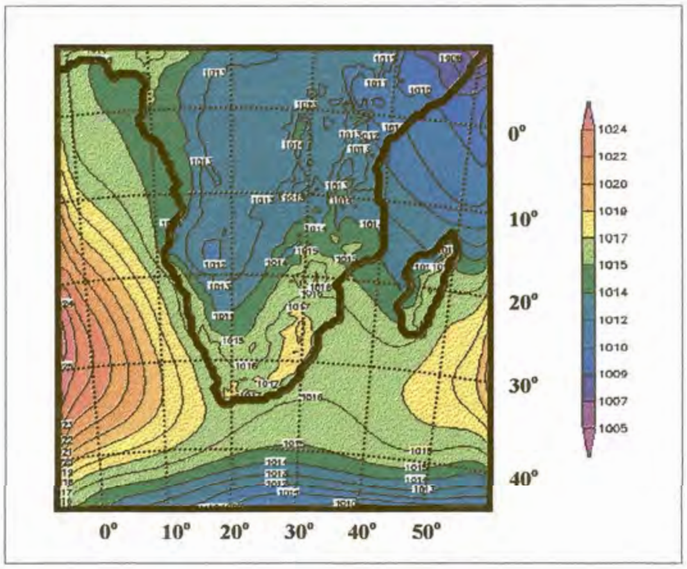

Figure 5.3f Mean sea-level pressure (MSLP) measured in hPa for July as simulated by DARLAM. The pressure contour interval is 1 hPa.

5.4.2 LOW-LEVEL WIND PATTERNS

The climatology of wind vectors from the NCEP reanalyses data at an altitude of 10 m is superimposed upon the MSLPs in figures 5.3a (January) and 5.3b (July). This is regarded as observed patterns. The associated model simulated streamlines on the lowest model levels ($\sigma = 0.98$) are illustrated in figures 5.4a and 5.4b (for the CSIRO9 AGCM) and 5.4c and 5.4d (for DARLAM).

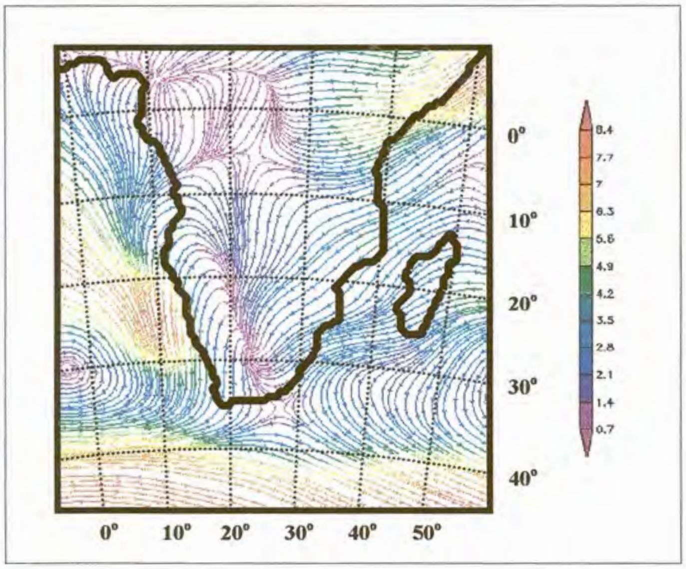

Figure 5.4a Mean streamlines at the lowest model level ($\sigma = 0.98$) measured in $m.s^{-1}$ for January as simulated by the CSIRO9 AGCM.

The CSIRO9 AGCM does not capture the observed low-level convergence in the Mozambique Channel that usually occurs during January in association with the low over the area (compare figures 5.3a and 5.4a). This flow deficiency may be attributed to the inadequate, smooth topography of Madagascar used in AGCM simulations (figure 5.2a). With a more detailed topography, it is anticipated that DARLAM will provide improved streamline simulations.

Both DARLAM and the CSIRO9 AGCM reproduce the zone of convergence over the western parts of southern Africa (figures 5.4a and 5.4c). The convergence is associated with the observed continental low that usually develops over Namibia and Botswana during the austral summer. However, over the central and eastern interior of South Africa, the CSIRO9 AGCM produces north-easterly flow (figure 5.4a) whilst DARLAM simulates a pronounced northerly flow (figure 5.4c). The NCEP reanalysis, or observed winds (figure 5.3a), are in favour of the DARLAM simulation of a dominant northerly component in the flow to the west of the eastern escarpment of South Africa. The northerly flow probably results from an interaction between the counter-clockwise circulation around the Indian high and continental low-pressure systems (continental troughs). In addition, DARLAM also successfully simulates the observed higher pressures over the eastern escarpment of South Africa (section 5.4.1), a feature that does not occur in the CSIRO9 AGCM simulation. In this respect it is also worthwhile noting that in reality the topography of Madagascar turns north-easterly flow, which prevails over the ocean to the east of the island, into easterly flow over the Mozambique Channel (figure 5.3a). DARLAM captures this phenomenon (figure 5.4c) but the CSIRO9 AGCM, with its smooth topography, persists with north-easterly flow over the Mozambique Channel and eventually also over the eastern parts of South Africa (figure 5.4a). In fact, south of 20ºS over the coast of Mozambique, south-easterly flow can be observed (figure 5.3a). DARLAM simulates easterly flow over this area (figure 5.4c) but the AGCM persists with north-easterly streamlines (figure 5.4a).

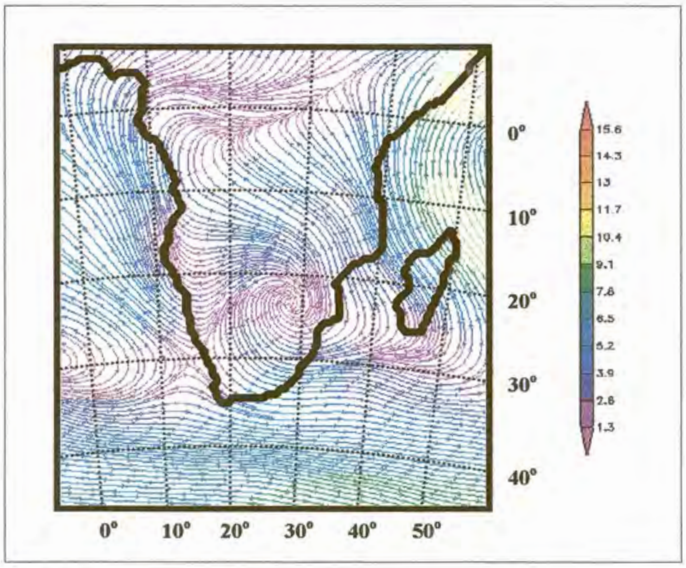

Figure 5.4b Mean streamlines at the lowest model level ($\sigma = 0.98$) measured in m.s^{-1} for July as simulated by the CSIRO9 AGCM.

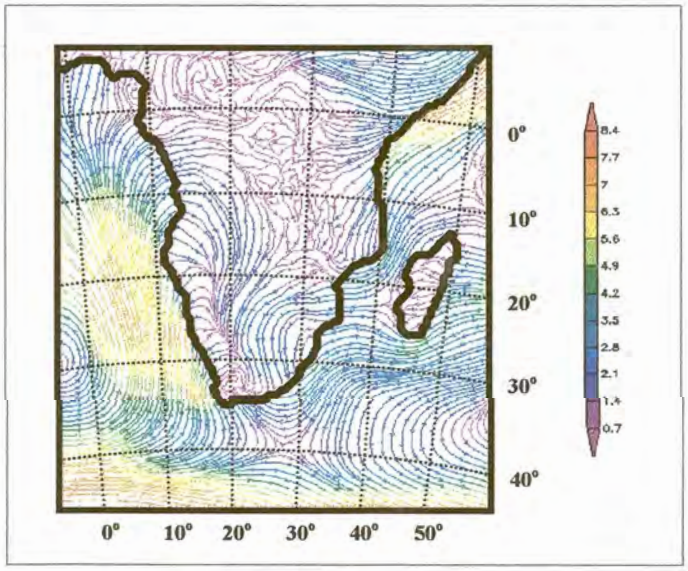

Figure 5.4c Mean streamlines at the lowest model level ($\sigma = 0.98$) measured in m.s^{-1} for January as simulated by DARLAM.

Compared to the CSIRO9 AGCM, DARLAM simulates weaker low-level westerly flow to the south of Africa in both the January and July climatologies (figures 5.4a, 5.4b, 5.4c and 5.4d). The observed flow is in general stronger than simulated by both DARLAM and the CSIRO9 AGCM. The weaker DARLAM flow is more obvious in the July simulation when DARLAM also underestimates the meridional pressure gradient to the south of South Africa, as well as the intensity of the subtropical high pressure belt over the interior of South Africa (figure 5.3f).

For July both the models reproduce the observed winter offshore flow over the eastern parts of South Africa (figures 5.3b, 5.4b and 5.4d). The offshore flow is a result of counter-clockwise rotation in the subtropical high-pressure zonal belt over the region (figure 5.3b, 5.3d and 5.3f). Once again DARLAM improves on the AGCM simulation by capturing the cyclonic flow around the trough that is situated over the western parts of Madagascar (figure 5.3b and 5.4d).

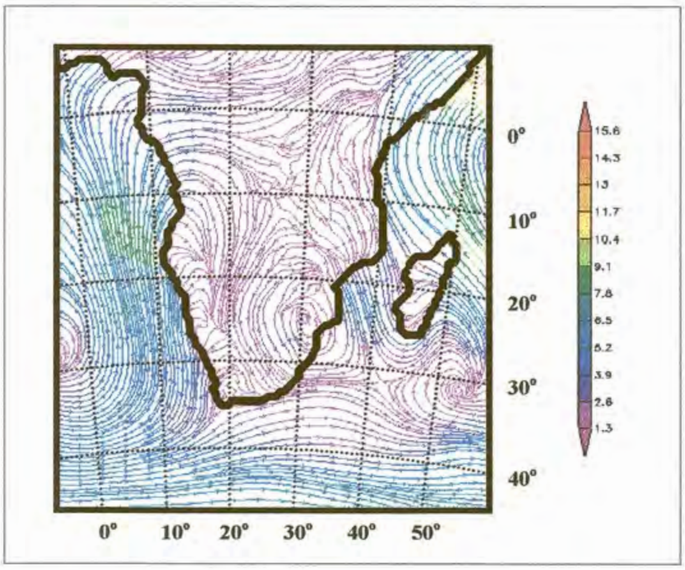

Figure 5.4d Mean streamlines at the lowest model level ($\sigma = 0.98$) measured in m.s^{-1} for July as simulated by DARLAM.

5.4.3 SURFACE TEMPERATURE

Figure 5.5a and 5.5b provide some detail concerning the observed features of near surface air temperature distribution over the SADC region and adjacent oceans. During January and July a well-defined meridional temperature gradient is present over the region. The gradient is obviously stronger during the austral winter (figure 5.5b). Temperatures are lower over the Atlantic Ocean (where the cold Benguela ocean current is associated with upwelling along the western coastline of southern Africa) than over the Indian Ocean. In the Mozambique Channel, where the warm Agulhus ocean current flows southward, warmer temperatures likewise intrude far to the south.

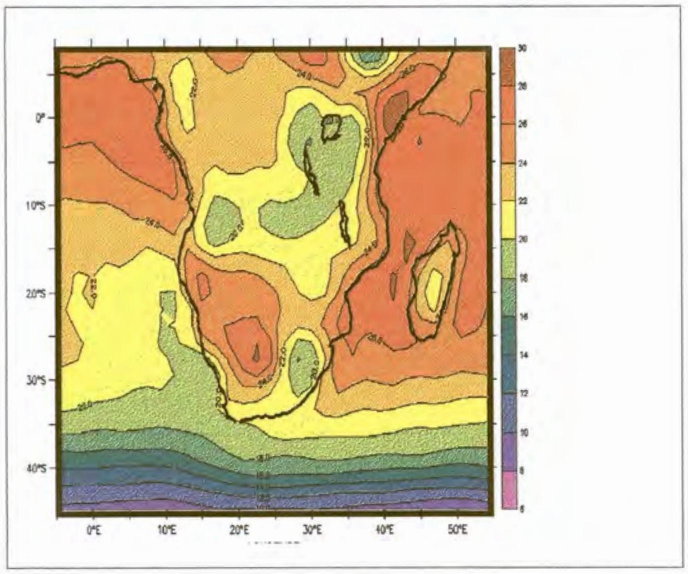

Figure 5.5a Observed 2m-temperature climate measured in °C for January as obtained from a 40-year (1958 to 1998) NCEP reanalysis climatology. The temperature contour interval is 2 °C.

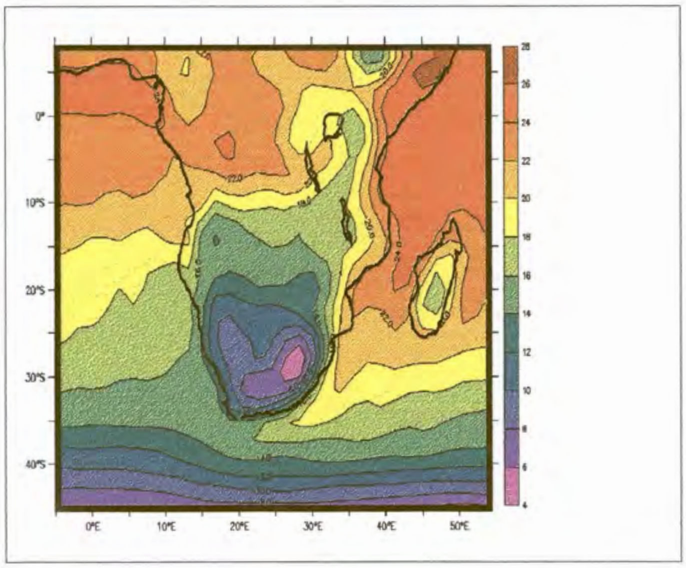

Figure 5.5b Observed 2m-temperature climate measured in °C for July as obtained from a 40-year (1958 to 1998) NCEP reanalysis climatology. The temperature contour interval is 2 °C.

During January temperature maximums in excess of 28°C are observed in Tropical East Africa, the western interior of South Africa, Botswana and in the Mozambique Channel (figure 5.5a). In both the January and July fields the influence of topography on near surface temperature over the south-eastern interior of South Africa is well illustrated. Colder isoterms from the south extend northward over this high altitude region. The steep escarpment along the south-eastern part of South Africa is also associated with steep temperature gradients, especially during the austral winter (figure 5.5b) when maximum insolation shifts northwards and topographic effects become more profound. The eastern Madagascar mountain range has a similar effect on temperature distribution over the island (figures 5.5a and 5.5b).

When comparing CSIRO9 AGCM and DARLAM simulated temperatures it is important to keep in mind that the AGCM simulations represent surface temperatures, whilst DARLAM and NCEP data are screen height (2m) air temperatures. This explains why the CSIRO9 AGCM temperatures are, on average, a degree or two higher than those of the other two fields. In general, simulations from the two models have specific similarities but there are also some major differences. DARLAM contains a more detailed representation of the land/ocean boundary. This is especially noticeable along the western coastline, where the change in near surface temperature is more abrupt in the LAM simulations (figures 5.5e and 5.5f) compared to those of the CSIRO9 AGCM (figures 5.5c and 5.5d). Both models capture the observed meridional temperature gradient, the northward intruding temperatures along the western coastline, as well as the southward extending warmer temperatures along the eastern coastline.

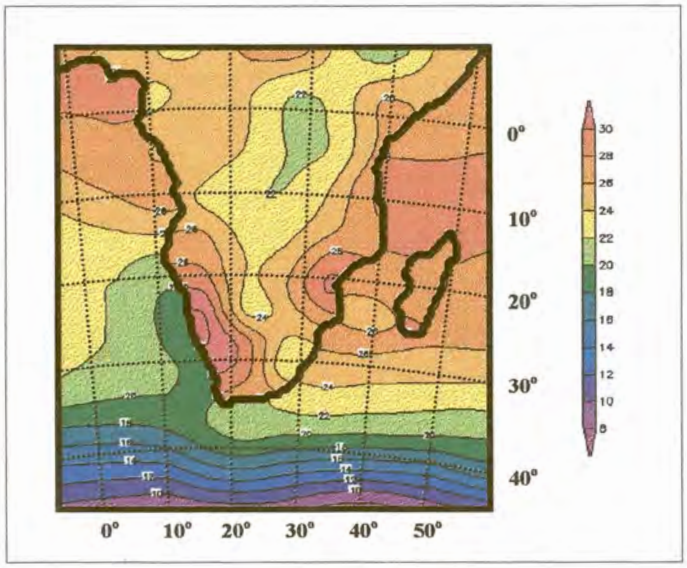

Figure 5.5c Surface temperature climate measured in °C for January as simulated by the CSIRO9 AGCM. The temperature contour interval is 2 °C.

Compared to the CSIRO9 AGCM simulations, DARLAM temperature patterns are in general closer to the associated observed patterns over the landmasses. DARLAM reproduces the observed January temperature maximums over the western interior of South Africa, Botswana, Tropical East Africa and the northern part of the Mozambique Channel (figure 5.5e). Note that DARLAM underestimates these temperature maximums by a degree or two. The CSIRO9 AGCM, however, spuriously simulates temperature maximums for January (figure 5.5c) in a broad band over Namibia at the lee side of the smoothed AGCM model plateau (figure 5.2a). The AGCM also fails to simulate the temperature maximum observed over Tropical East Africa during January. This might be attributed to the fact the low-altitude Great Eastern African Valley topography with the associated higher maximum temperatures is not embedded in the smoothed AGCM topography (figure 5.2a). The higher resolution DARLAM topography does resolve this feature (figure 5.2b) resulting in a significantly improved simulation of near surface temperature over the region (compare figures 5.5c and 5.5e to 5.5a). Both DARLAM and the CSIRO9 AGCM underestimate temperatures over the Mozambique Channel in January.

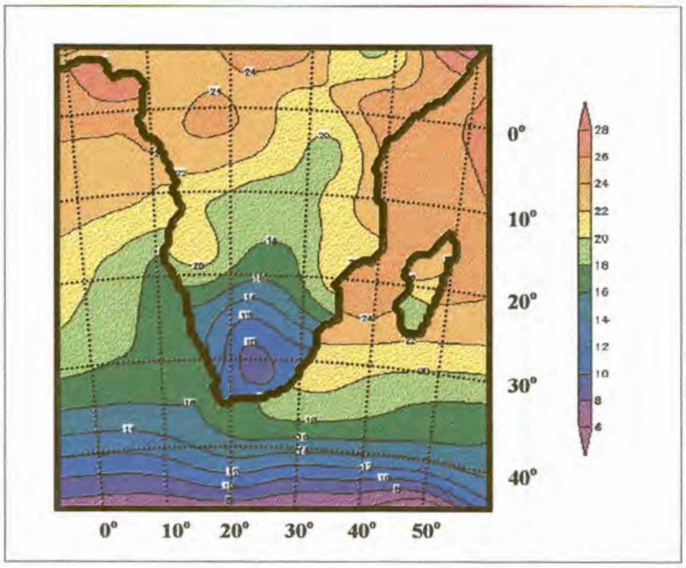

Figure 5.5d Surface temperature climate measured in °C for July as simulated by the CSIRO9 AGCM. The temperature contour interval is 2 °C.

Both models capture the observed intrusion of colder isoterms over the south-eastern interior of South Africa that usually occur during January and July. Over this region DARLAM July temperature simulations (figure 5.5f) compare well with observations (figure 5.5b). DARLAM however, severely overestimates the occurrence of colder temperatures over the south-eastern interior of South Africa in January. Analysis of DARLAM rainfall simulations (discussed in the next section) indicates that DARLAM severely overestimates rainfall totals over this region. The overestimation of rainfall may be responsible for the underestimation of screen temperature as a result of severe evaporative cooling at the model surface.

In both the January and July simulations DARLAM successfully captures the observed west-east temperature gradient over Madagascar (figures 5.5e and 5.5f), a feature that does not occur in the corresponding AGCM simulations (figures 5.5c and 5.5d). DARLAM simulates lower than observed temperatures over eastern Madagascar. As an air mass in the dominant easterly flow over Madagascar descends on the lee side of the mountain range, it will warm adiabatically to produce higher near surface temperatures over the western parts of Madagascar. It seems as if the adiabatic heating (bergwinds) is adequately reproduced in DARLAM simulations, while the CSIRO9 AGCM with its smoothed topography reduces the influence of surface elevation on the general circulation and temperature distribution.

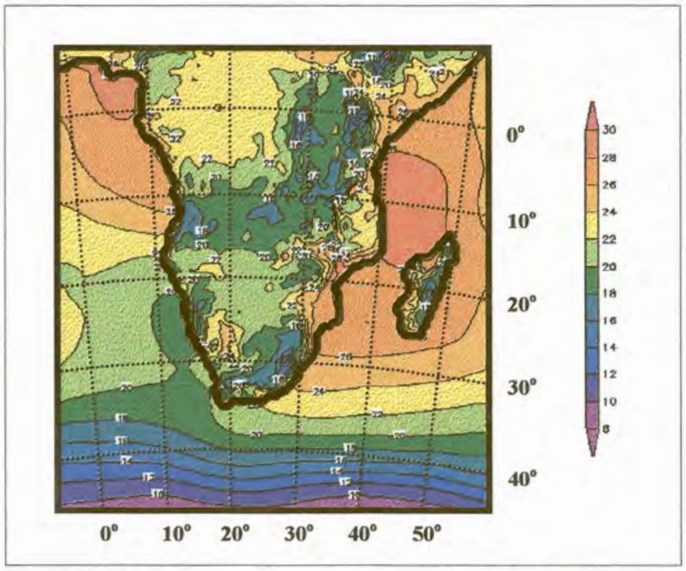

Figure 5.5e 2m-temperature climate measured in °C for January as simulated by DARLAM. The temperature contour interval is 2 °C.

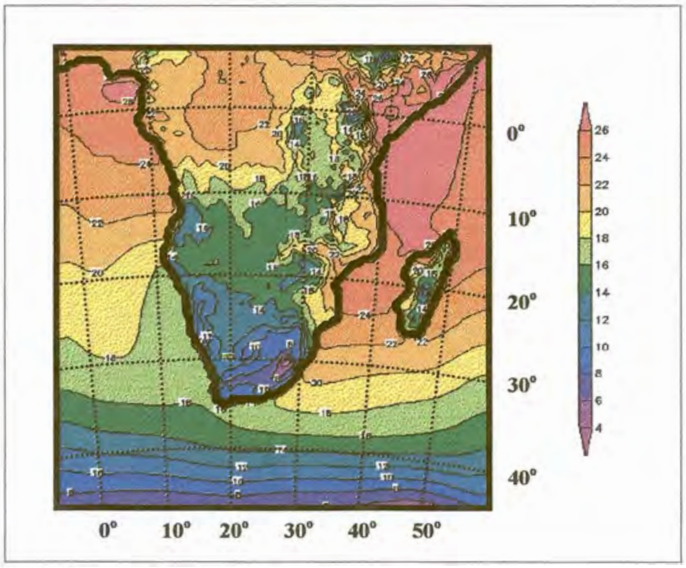

Figure 5.5f 2m-temperature climate measured in °C for July as simulated by DARLAM. The temperature contour interval is 2 °C.

5.4.4 RAINFALL

The climatology of rainfall from the NCEP reanalyses data provide some indication of the observed rainfall distribution over the SADC region during January (figure 5.6a) and July (figure 5.6b).

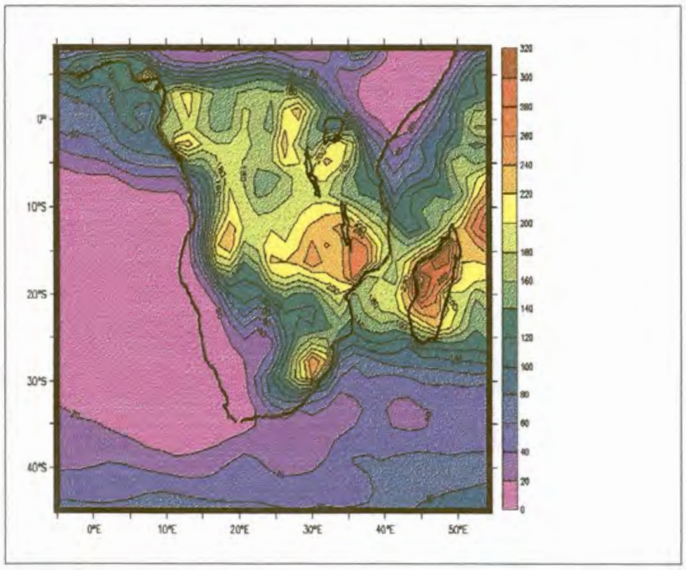

Figure 5.6a Observed rainfall total climate measured in mm for January as obtained from a 40-year (1958 to 1998) NCEP reanalysis climatology. The rainfall contour interval is 20 mm.

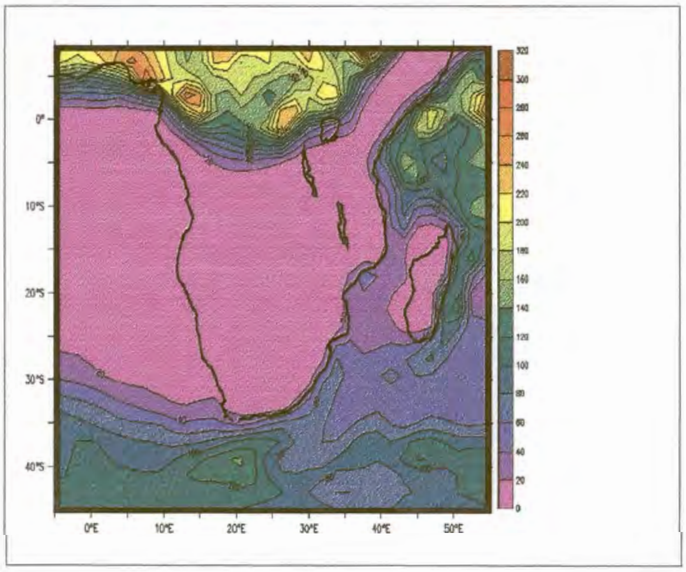

Figure 5.6b Observed rainfall total climate measured in mm for July as obtained from a 40-year (1958 to 1998) NCEP reanalysis climatology. The rainfall contour interval is 20 mm.

Highest rainfall figures for January occur in a north-west to south-east band located between 10ºS and 20ºS over Mozambique and Madagascar, with a second maximum located over the south-eastern escarpment of South Africa (figure 5.6a). Arid conditions (with monthly rainfall totals below 20 mm) have been recorded along the western coastline of South Africa, Namibia and even Angola. South of latitude 20ºS, the January rainfall distribution over southern Africa is characterised by a marked west-east gradient.

During July, when the subtropical high-pressure belt establishes itself over the African subcontinent (figure 5.3b) observed rainfall totals over southern Africa decrease significantly (figure 5.6b). The ITCZ shifts to the north, inducing higher rainfalls over tropical regions north of the equator. Both Kenia and Somalia record drier conditions than experienced during January. The southern coastline of South Africa and adjacent interior is influenced by cold fronts sweeping over the area from west to east causing increased winter rainfall (figure 5.6b).

Unlike the observational (NCEP reanalysis) data, the mean January rainfall distribution as simulated by the CSIRO9 AGCM is orientated in a north-west to south-east band across the African subcontinent, with the highest rainfall figures simulated over Zambia and southern Zaire (figure 5.6c). A second distinctive rainfall maximum is located over the eastern part of Zimbabwe and north-eastern South Africa. The CSIRO9 AGCM does not capture the north-east to south-west distribution of observed maximum rainfall between 10°S and 20ºS over Mozambique and Madagascar. As a result the model produces far less rainfall than observed over large parts of tropical and subtropical east Africa. The AGCM also simulates less than observed rainfall over southern Angola and northern Namibia. In contrast, the CSIRO9 AGCM simulates up to twice as much rainfall as observed over eastern Zimbabwe and north-eastern South Africa (figure 5.6c).

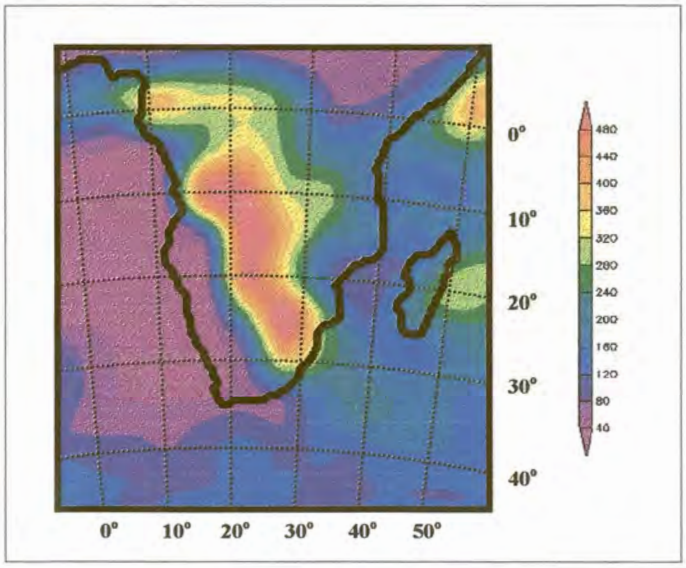

Figure 5.6c Rainfall total climate measured in mm for January as simulated by the CSIRO9 AGCM.

The July CSIRO9 AGCM simulation successfully captures the northward displacement of the ITCZ and subsequent drier conditions over Kenia and Somalia (figure 5.6d). The model adequately simulates the generally drier conditions that occur over the subcontinent during the austral winter. Rainfall totals increase over the south coast of South Africa, in harmony with the observed pattern (figure 5.6b).

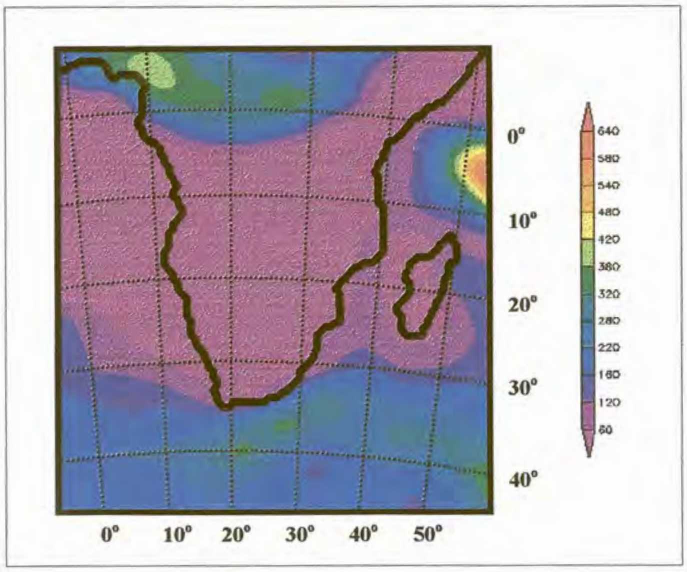

Figure 5.6d Rainfall total climate measured in mm for July as simulated by the CSIRO9 AGCM.

The mean January (figure 5.6e) rainfall distribution as simulated by DARLAM is orientated more from west-east than simulated by the CSIRO9 AGCM (figure 5.6c). This represents an improvement in the DARLAM simulated rainfall pattern. The difference between the two simulations is most notable over the eastern parts of South Africa and northern parts of Mozambique and Madagascar (compare figures 5.6c and 5.6e). Over both areas DARLAM simulates more rainfall than observed, compared to the less than observed rainfall simulated by the CSIRO9 AGCM. The pattern of rainfall maximums however, occurring between 10ºS and 20ºS over northern Mozambique and Madagascar with a second maximum located over south-eastern South Africa, is well captured in the DARLAM simulations.

In general, the DARLAM simulated rainfall pattern over tropical regions is superior to that of the CSIRO9 AGCM. In the DARLAM simulation there is some indication of the rainfall maximums observed over Gabon and Tanzania (compare figures 5.6a and 5.6e). There is no indication of the occurrence these maximums in the corresponding AGCM simulation (figure 5.6c). The DARLAM improvement in the simulated pattern of summer rainfall over the tropics (relative to the CSIRO9 AGCM) probably results from an improved representation of the southward extension of the ITCZ and low-level convergence. A comparison between the CSIRO9 AGCM simulated mean

January low-level streamlines (figure 5.4a) and the associated DARLAM simulations (figure 5.4c) reveals that DARLAM simulates more pronounced low-level convergence in tropical regions south of the equator during January.

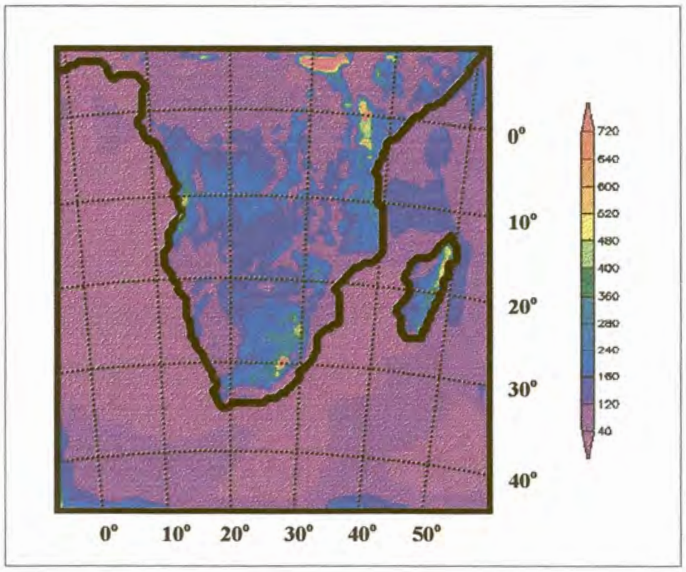

Figure 5.6e Rainfall total climate measured in mm for January as simulated by DARLAM.

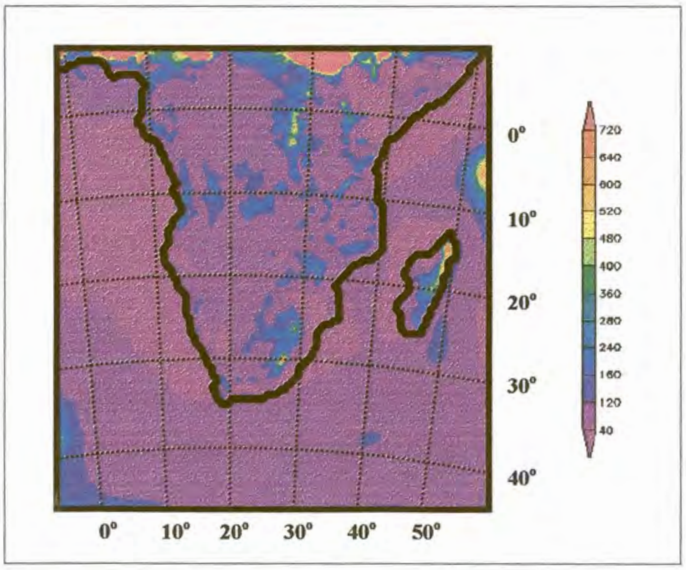

Figure 5.6f Rainfall total climate measured in mm for July as simulated by DARLAM.

The northward displacement of high rainfall totals in the DARLAM simulation for July (figure 5.6f) suggests that the northward displacement of the ITCZ in the AGCM simulation is adequately transferred to DARLAM through the lateral boundary forcing. Unfortunately DARLAM severely overestimates rainfall totals over the south-eastern escarpment of South Africa and the northern escarpment of Madagascar (figure 5.6f). The overestimation may be enhanced by the failure of DARLAM to capture the intensity of the subtropical high-pressure belt (and the associated subsidence) during the austral winter.

DARLAM and the CSIRO9 AGCM overestimate rainfall along the steep escarpment of south-eastern South Africa during January but the overestimation is far more severe in the DARLAM simulations. This is well illustrated in figure 5.7a, which represent differences in rainfall totals between DARLAM and the CSIRO9 AGCM for January. None the less, the DARLAM simulated pattern of a west-east distribution of rainfall over the south-eastern South Africa (figure 5.6a) is a good representation of observed fields (figure 5.6a). DARLAM simulations (figure 5.6e) incorporate far greater complexity in simulated rainfall patterns than is captured by the AGCM with its coarser resolution (figure 5.6c). Along the escarpment, close to the mountains of Lesotho and the southern Drakensberg, DARLAM rains are up to three times the observed values (figure 5.6e). During rainfall events over this area, the lower tropospheric flow up-slope (perpendicular to the topographic obstacle) and the penetrating surface moisture is advected from the east where it originates from a ridging anticyclone (Joubert et al., 1999). It has been motivated in section 5.4.1 that DARLAM produces improved simulations (relative to the CSIRO9 AGCM) of the ridging high-pressures (and the associated low-level mass convergence) along the south-eastern escarpment of South Africa during January. This may partially explain why rainfall totals in this region are higher in the DARLAM simulations (figure 5.7a).

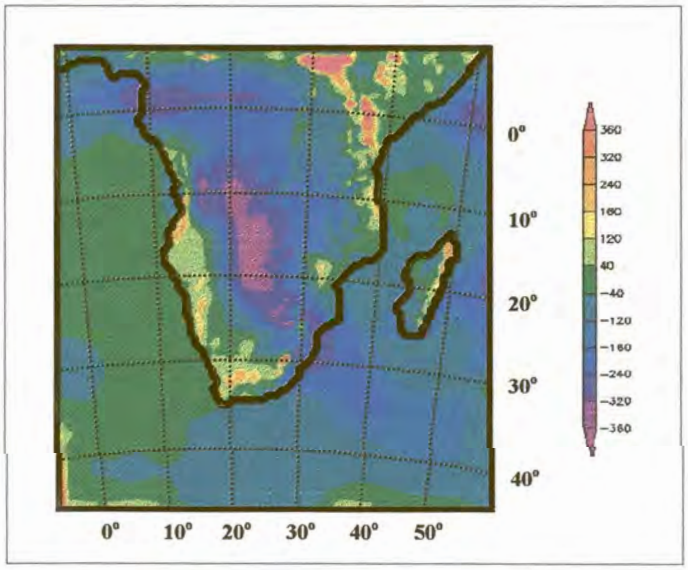

Figure 5.7a DARLAM minus CSIRO9 AGCM rainfall totals measured in mm for January.

The CSIRO9 AGCM also overestimates rainfall totals over the same region, although less than DARLAM. This might result from large quantities of moisture that are transported by the forcing AGCM simulations to the eastern part of South Africa. The mountain resonance effect, a phenomenon present in semi-Lagrangian model formulations, may also result in an overestimation of mean vertical velocities and increased rainfall over steep topographic gradients (see Chapter 3). Since the CFL criterion was satisfied in the present experiments, it is unlikely that the mountain resonance effect had a significant impact on the simulations. It is interesting to note however, that a vertical cross-section of topography and rainfall along approximately 30ºS (figure 5.8) does illustrate a strong correlation between DARLAM simulated rainfall maximums and elevation peaks.

The improved representation of the Madagascar topography in DARLAM results in higher model rainfall totals than simulated by the CSIRO9 AGCM (figures 5.7a and 5.7b). The CSIRO9 AGCM simulates less rainfall than observed over Madagascar, especially over the higher rainfall region in the northern part of the island. DARLAM overestimate rainfall totals, particularly over the eastern mountain range. The overestimation is most severe during July, when DARLAM simulates more than seven times the observed rainfall amounts over the northern parts of the island.

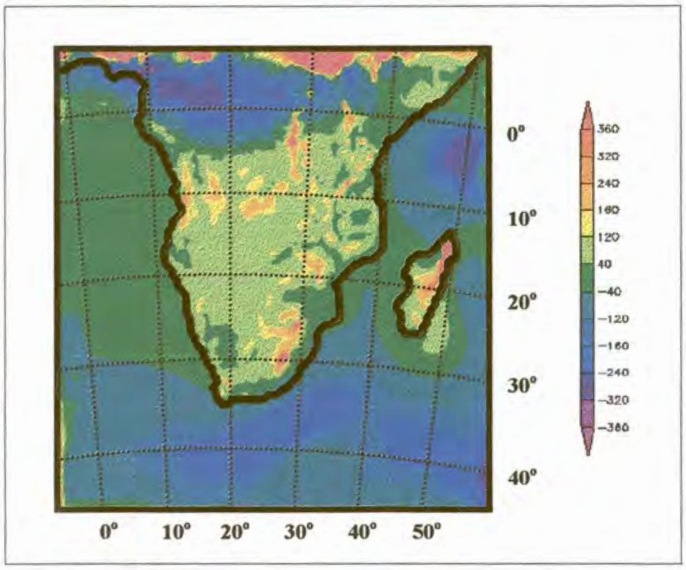

Figure 5.7b DARLAM minus CSIRO9 AGCM rainfall totals measured in mm for July.

Figure 5.8 depicts a vertical cross section of the DARLAM surface topography with the January rainfall climate along the 30ºS latitude as simulated by DARLAM , the CSIRO9 AGCM and observed rainfall. This graph summarises the various rainfall projections over an area with relative steep topography.

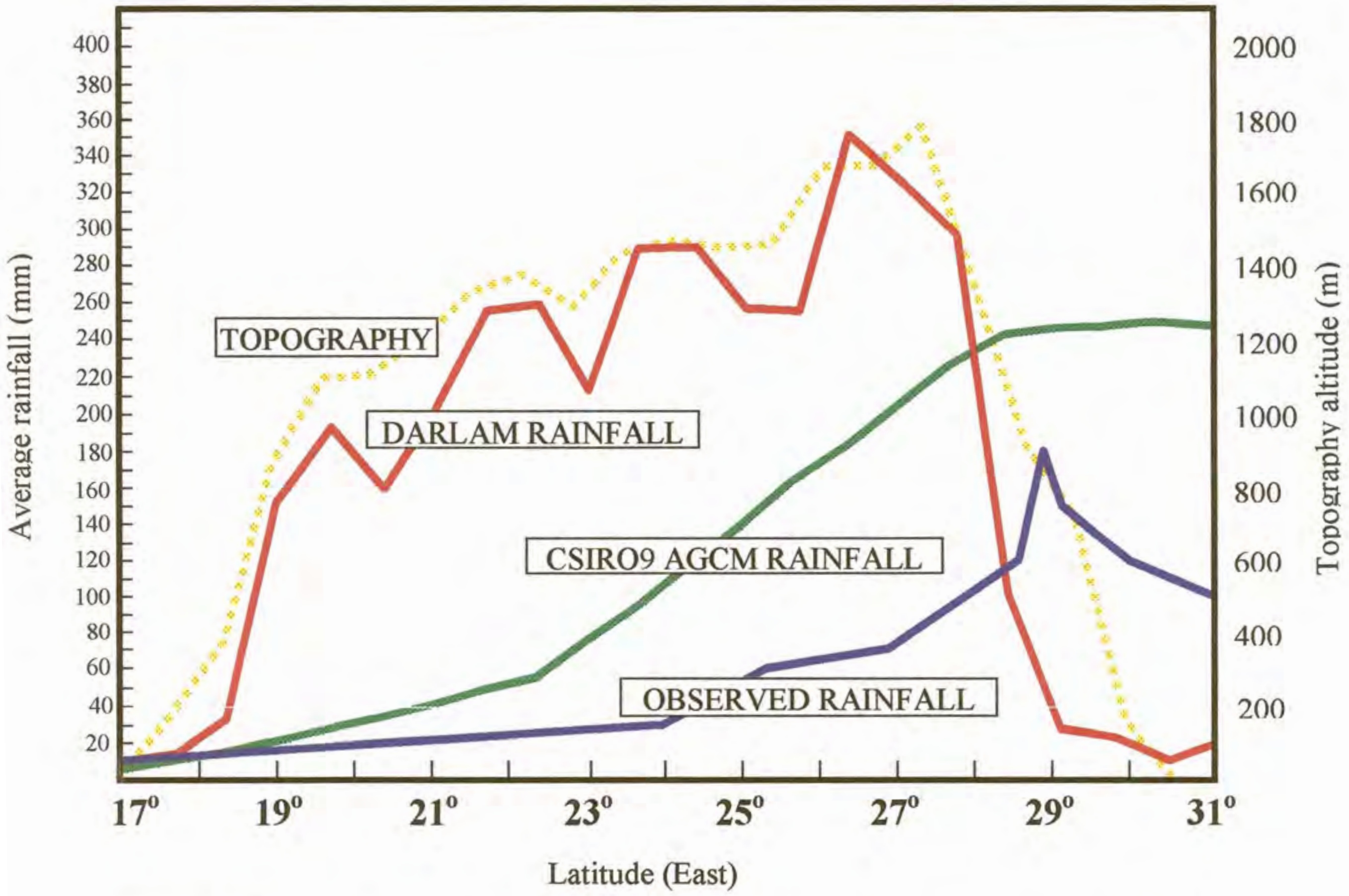

Figure 5.8 A vertical cross section of the DARLAM surface topography measured in meters (brown dotted line) with the January (summer) rainfall climate measured in mm along the 30ºS latitude as simulated by DARLAM (red line) and the CSIRO9 AGCM (green line). The associated observed rainfall graph is depicted in blue. Note the high rainfall totals along the eastern escarpment.

5.5 DISCUSSION

DARLAM generally provides a more accurate and detailed simulation of climate over the SADC region than the CSIRO9 AGCM. This may be attributed to the fact that topographical features, which have an influence on the climate of the region, are more clearly resolved at the 60 km resolution of the nested model than they are by the CSIRO9 AGCM. These features include the escarpment along the south-eastern part of South Africa and the Great East African Valley. The resulting climatological patterns (in particular rainfall and surface temperature) have more detail and are more complex in DARLAM simulations than in CSIRO9 AGCM simulations. The resulting DARLAM climatology exhibits several features that are also present in the forcing CSIRO9 AGCM. For example, the northward displacement of the ITCZ and the subtropical high-pressure belt during the austral winter is closely related in the AGCM and nested model simulations.

In contrast, DARLAM's January climatology over the central parts of the model domain differs from that of the AGCM and is a better representation of observations. This is particularly true of the low-pressure cells located over Namibia and Botswana. The DARLAM January rainfall distribution between 10°S and 20°S and over the south-eastern parts of South Africa provides a better representation of the observed west-east gradient of maximum rainfall than CSIRO9 AGCM. In the latter, the rainfall pattern is aligned north-east to south-west.

DARLAM underestimates the intensity of the observed winter (July) subtropical high-pressure region over the subcontinent. This contributes to a severe overestimation of July rainfall totals over the south-eastern parts of South-Africa. In this respect the DARLAM simulation is inferior to the CSIRO9 AGCM simulation that successfully captures the intensification of the subtropical high during winter.

DARLAM simulations produce more than twice the amount of rainfall observed over regions with steep topographic gradients, such as the South African eastern escarpment and Madagascar. This result has also been noted in other atmospheric models (Giorgi et al., 1994, McGregor and Walsh, 1994, Walsh and McGregor, 1995, Jenkins and Barron, 1997). The overestimation may be attributed to the fact that too much moisture is available in the model domain. Because DARLAM successfully captures events of low-level mass convergence along the eastern escarpments of South Africa and Madagascar, the excess of moisture may result in simulations with excessive rainfall. Another possible contributing factor to the overestimation of rainfall is the mountain resonance effect (Rivest and Staniforth, 1994; McGregor, 1997a) which may be present in DARLAM's semi-Lagrangian dynamical formulation. It should be noted that the solution advocated by Rivest and Staniforth (1994) to the mountain wave resonance problem is not incorporated in the DARLAM code used in the present study. The effectiveness of the proposed solution over the steep eastern escarpment of South Africa needs to be investigated in future experiments.

Despite the problems that occur when simulating observed rainfall magnitudes over regions of steep topography, DARLAM provides a more accurate simulation of observed rainfall distribution, particularly in regions where the AGCM's coarse resolution does not permit regional topographic features to be resolved. These preliminary simulations indicate that DARLAM is capable of simulating details on the regional scale with greater skill than the CSIRO9 AGCM.

CHAPTER 6

CONCLUSIONS AND RECOMMENDATIONS

The climate of the SADC region is fundamentally influenced by mesoscale circulation patterns that are not adequately simulated by AGCMs. The main reason for this is the coarse horizontal resolution of AGCMs. Computational requirements prevent AGCMs running at mesoscale resolutions of a few kilometres to about 100km. As a computationally feasible alternative, the technique of nested climate modelling utilises high-resolution LAMs to obtain climate simulations on the mesoscale. An appropriate range of synoptic situations is obtained by integrating an AGCM forward in time for an extended period. The lower resolution output of the AGCM is then used to force the lateral boundaries of the LAM. The LAM, with a horizontal resolution in the order of 100km, can simulate some of the mesoscale features which leads to a more accurate, detailed and realistic depiction of the region's climate.

A NCM domain over the SADC region should be sufficiently small to ensure that simulated circulation of the NCM does not depart from that of the driving AGCM on the synoptic scale. The domain however, has to be large enough to prevent the coarse scale lateral boundary conditions from dominating the solution over the area of interest. Full development by the NCM of features having a finer scale than those skilfully resolved by the AGCM should be possible. The horizontal resolution of the nested model should be fine enough to capture forcing and circulation on the mesoscale.

The model domain should encompass, to the extent feasible, all regions that include forcing and circulation that directly influence climate over the area of interest. For example, a domain over southern Africa should include the Agulhas retroflection region in the south and Madagascar in the east. Such a domain will also need to extend far enough over the Atlantic ocean to adequately capture the development and movement of mid-latitude cyclones and far enough northwards to capture tropical features like the semi-stationary tropical surface trough.

The nested model DARLAM has been developed for both mesoscale studies and for climate change experiments. The model is a two-time level, semi-implicit, hydrostatic primitive equations model. It uses an Arakawa C-grid and semi-Lagrangian horizontal advection with bicubic spatial interpolation. The model includes a full range of physical parameterisations. Many simulations have been performed (primarily over Australia) by one-way nesting DARLAM within the CSIRO9 AGCM or within observational analyses. Generally the finer resolution of the nested simulations provides significantly improved simulations near topographic features, in particular precipitation and near surface values.

The characteristic feature of the dynamical formulation of DARLAM is the semi-Lagrangian method used to solve the advective part of the primitive meteorological equations. The essential feature of semi-Lagrangian schemes is that the total or material derivatives in the equations of motion are treated directly by calculating the departure points of fluid parcels. The upstream values of the required fields are then usually evaluated by spatial interpolation. The main advantage of the semi-Lagrangian technique is that it allows for the relaxation of the CFL criterion. Theoretical analysis of the semi-Lagrangian scheme used in DARLAM reveals that this method offers unconditionally stable integrations with a high degree of advection accuracy. Numerical experiments involving a case of non-linear but uniform flow and a case of non-linear but strong deformational flow confirm that the semi-Lagrangian scheme used in DARLAM has excellent amplitude, phase and conservation properties. The scheme is shown to be superior to the well-known and widely used modified Lax-Wendrof finite difference scheme.

The nested climate model DARLAM has been nested within the output from the CSIRO9 AGCM to provide high-resolution simulations of present January and July climate over the SADC region. DARLAM provides a more accurate and detailed simulation of particularly January climate over southern Africa than is available from the AGCM. This is largely due to the fact that the regional topographical features which influence the climate of the SADC region, such as the steep escarpment of south-eastern South Africa and the Great East African Valley, are more clearly resolved at 60 km resolution of the NCM than they are by the CSIRO9 Mark II AGCM. Over regions of steep topographic gradients such as the South African escarpment and Madagascar, DARLAM simulates in excess of twice as much daily rainfall as observed. The nested model's mountain wave response possibly contributes to this over estimation.

Results from the first nested climate modelling simulations over the SADC region indicate that DARLAM is capable of simulating the details of regional climate with greater skill than the AGCM. The nested modelling approach to applications such as projecting the regional response to global climate change therefore holds significant promise.

There remain theoretical and scientific problems to be solved in the use of limited-area climate models. Tropical domains pose additional difficulties for the one-way nested modelling approach, relating to the weaker boundary forcing in such domains and the greater necessity for the physical parameterisation schemes of the LAM and AGCM to be compatible. This problem is of particular importance for the SADC region, which includes extensive regions north and south of the equator. Another aspect of nested climate modelling still needing improvement is the tendency for the occurrence of excessive precipitation in NCM simulations over regions of steep topography. The cause for these over estimations is not fully understood. In some NCMs the over estimation may be related to the model's mountain wave response, while in others the dynamical effects of the cumulus parameterisation scheme used may contribute to the over estimation. This unresolved issue needs to be investigated in future nested climate modelling experiments over the SADC region.

APPENDIX A

Visual basic code for Crowley's cone test: D3 scheme

```
********************
CLS
CLEAR

DIM u(35, 35), v(35, 35), c(35, 35), d(35, 35), dx(35, 35), dy(35, 35), xp(35,
&35), yp(35, 35)

h = 1
ll = 1
HA = 35
VA = 35
ta = 1 * 288
ww = 7.2722
s = (2 * 3.141593) / (ta * ww)

'*****************************************************
OPEN "c:/matlab/vogx.m" FOR OUTPUT AS #2

'*****************************************************
'**** Velocity field

FOR i = 1 TO 35
x = (i - 18) * h
FOR j = 1 TO 35
v(i, j) = -ww * x
NEXT j
NEXT i

FOR j = 1 TO 35
y = (j - 18) * ll
FOR i = 1 TO 35
u(i, j) = ww * y
NEXT i
NEXT j

'*****************************************************
'**** Initial cone distribution

FOR i = 1 TO 35
x = (i - 18) * h
FOR j = 1 TO 35
y = (j - 18) * ll
IF (x + 8) ^ 2 + y ^ 2 <= 16 THEN
c(i, j) = -(25) * SQR((x + 8) ^ 2 + y ^ 2) + 100
ELSE c(i, j) = 0
END IF
NEXT j
NEXT i

'*****************************************************
'**** Calculation of departure points

FOR i = 3 TO 33
x = (i - 18) * h
FOR j = 3 TO 33
```

```
y = (j - 18) * ll

ux = (u(i + 1, j) - u(i - 1, j)) / (2 * h)
uy = (u(i, j + 1) - u(i, j - 1)) / (2 * ll)
vx = (v(i + 1, j) - v(i - 1, j)) / (2 * h)
vy = (v(i, j + 1) - v(i, j - 1)) / (2 * ll)
uxx = (u(i + 2, j) - 2 * u(i, j) + u(i - 2, j)) / (4 * h ^ 2)
uyy = (u(i, j + 2) - 2 * u(i, j) + u(i, j - 2)) / (4 * ll ^ 2)
uxy = (u(i + 1, j + 1) - u(i - 1, j + 1) - u(i + 1, j - 1)
& + u(i - 1, j - 1)) /(4 * h * ll)
vxx = (v(i + 2, j) - 2 * v(i, j) + v(i - 2, j)) / (4 * h ^ 2)
vyy = (v(i, j + 2) - 2 * v(i, j) + v(i, j - 2)) / (4 * ll ^ 2)
vxy = (v(i + 1, j + 1) - v(i + 1, j - 1) - v(i - 1, j + 1)
& + v(i - 1, j - 1)) / &(4 * h * ll)

dx(i, j) = x - s * u(i, j) + ((s ^ 2) / 2) * (u(i, j) * ux + v(i, j) * uy)
& - ((s ^ 3) / 6) * ((u(i, j) ^ 2) * uxx + u(i, j) * (ux ^ 2) + 2 * u(i, j) *
& v(i, j) * uxy + u(i, j) * vx * uy + v(i, j) * uy * ux + (v(i, j) ^ 2) * (uyy)
& + v(i, j) * &vy * uy)
dy(i, j) = y - s * v(i, j) + ((s ^ 2) / 2) * (u(i, j) * vx + v(i, j) * vy)
& - ((s ^ 3) / 6) * ((u(i, j) ^ 2) * vxx + u(i, j) * ux * vx + 2 * u(i, j) *
& v(i, j) * vxy + u(i, j) * vx * vy + v(i, j) * uy * vx + (v(i, j) ^ 2) * (vyy)
& + & v(i, j) * &((vy) ^ 2))

FOR l = 1 TO 35
xt = (l - 18) * h
yt = (l - 18) * ll
IF dx(i, j) > xt THEN xp(i, j) = l + 1
IF dy(i, j) > yt THEN yp(i, j) = l + 1
NEXT l

NEXT j
NEXT i

'*************************************
'***** Bicubic interpolation

FOR t = 1 TO ta
PRINT t

FOR i = 3 TO 33
FOR j = 3 TO 33

d(i, j) = 0
w = 0
lp = 0
som = 0
som1 = 0

'***** Bilinear interpolation may be required

IF xp(i, j) = 34 OR yp(i, j) = 34 THEN lp = 1
IF xp(i, j) = 3 OR yp(i, j) = 3 THEN lp = 1

FOR k = lp + xp(i, j) - 2 TO xp(i, j) + 1 - lp
xk = (k - 18) * h
FOR l = lp + yp(i, j) - 2 TO yp(i, j) + 1 - lp
yl = (l - 18) * ll

somx = 1
```

```
FOR m = lp + xp(i, j) - 2 TO xp(i, j) + 1 - lp
xm = (m - 18) * h
IF m <> k THEN somx = ((dx(i, j) - xm) / (xk - xm)) * somx
NEXT m

somy = 1
FOR m = lp + yp(i, j) - 2 TO yp(i, j) + 1 - lp
ym = (m - 18) * ll
IF m <> l THEN somy = ((dy(i, j) - ym) / (yl - ym)) * somy
NEXT m

w = somx * somy
som = som + w * c(k, l)
soml = soml + w

NEXT l
NEXT k

d(i, j) = som

NEXT j
NEXT i


FOR i = 1 TO 35
FOR j = 1 TO 35
c(i, j) = d(i, j)
NEXT j
NEXT i

NEXT t

'**********************************
'**** Writing to Matlab

PRINT #2, "x=[";
FOR i = 1 TO HA - 1
x = (i - 18) * h
PRINT #2, x; ",";
NEXT i
i = HA
x = (i - 18) * h
PRINT #2, x; "];"
PRINT #2, " "

PRINT #2, "y=[";
FOR j = 1 TO VA - 1
y = (j - 18) * ll
PRINT #2, y; ",";
NEXT j
j = VA
y = (j - 18) * ll
PRINT #2, y; "];"
PRINT #2, " "
PRINT #2, "[X,Y]=meshgrid(x,y);"

PRINT #2, " "

PRINT #2, "Z=[";
FOR j = 1 TO VA - 1
FOR i = 1 TO HA
```

```
PRINT #2, c(i, j);
PRINT #2, " ";
NEXT i
PRINT #2, " "
NEXT j

j = VA

FOR i = 1 TO HA - 1
PRINT #2, c(i, j);
PRINT #2, " ";
NEXT i
i = HA
PRINT #2, c(i, j);
PRINT #2, "];"
PRINT #2, " "
PRINT #2, "surf(X,Y,Z)"
CLOSE 2

'****************************************************
END
'****************************************************
'****************************************************
```

APPENDIX B

Fortran code for Smolarkiewicz's deformational flow: D_3 scheme

```
      ********************
      program smolar

      integer A, L, CI, IER, t, lp, xp(101,101), yp(101,101),ta
      real tt,aa
      real pi, kk, tsi(101,101), c(101,101), ALEV(13),KEELY(10), TR(6)
      real u(101,101), v(101,101), s, dx(101,101), dy(101,101)
      real zt, d(101,101), som, soml, xk, yl, xm, ym, somx, somy, w
      real f(101,101),b(101,101)
      character*(4) LABEL

      A=8
      L=100
      pi=3.141592654
      kk=4*pi/L
      s=0.7

c****  Iterations correspond to the times in the paper of Staniforth et al. (1987)
c     ta=19
c     ta=38
c     ta=57
c     ta=75
c     ta=377
      ta=3768

c****  Calculate grid point values of.............
      do i = 1, 101
      x = (i-1)
      do j = 1, 101
      y = (j-1)
c**** Streamlines
      tsi(i,j) = A*(sin(kk*x))*(cos(kk*y))
c**** Velocity field
      u(i,j)  = A*(kk)*(sin(kk*x))*(sin(kk*y))
      v(i,j)  = A*(kk)*(cos(kk*x))*(cos(kk*y))
      enddo
      enddo

c**** Calculate the grid point values of initial cone distribution
      do i = 1, 101
      x = (i-1)
      do j = 1, 101
      y = (j-1)
      c(i,j)  = 0.0
      if ((x-50)**2 + (y-50)**2 .le. 225.0) c(i,j) =
     & (-1.0/15.0)*(((x-50)**2 + (y-50)**2)**(0.5)) +1
      b(i,j)=c(i,j)
      enddo
      enddo

c********************
c****  Determination of departure points

      do i=2,100
```

```
      x=i-1
      do j=2,100
      y=j-1

      ux = (u(i+1,j)-u(i-1,j))/2.
      uy = (u(i,j+1)-u(i,j-1))/2.
      vx = (v(i+1,j)-v(i-1,j))/2.
      vy = (v(i,j+1)-v(i,j-1))/2.
      uxx = (u(i+2,j)-2.*u(i,j)+u(i-2,j))/4.
      uyy = (u(i,j+2)-2.*u(i,j)+u(i,j-2))/4.
      uxy = (u(i+1,j+1)-u(i-1,j+1)-u(i+1,j-1)+u(i-1,j-1))/4.
      vxx = (v(i+2,j)-2.*v(i,j)+v(i-2,j))/4.
      vyy = (v(i,j+2)-2.*v(i,j)+v(i,j-2))/4.
      vxy = (v(i+1,j+1)-v(i+1,j-1)-v(i-1,j+1)+v(i-1,j-1))/4.

      dx(i,j)=x-s*u(i,j)+((s**2)/2.)*(u(i,j)*ux+
     &v(i,j)*uy)-((s**3)/6.)*((u(i,j)**2)*uxx+u(i,j)
     &*(ux**2.)+2.*u(i,j)*v(i,j)*uxy+u(i,j)*vx*uy+
     &v(i,j)*uy*ux+(v(i,j)**2)*(uyy)+v(i,j)*vy*uy)

      dy(i,j)=y-s*v(i,j)+((s**2)/2.)*(u(i,j)*vx+
     &v(i,j)*vy)-((s**3)/6.)*((u(i,j)**2)*vxx+u(i,j)
     &*ux*vx+2.*u(i,j)*v(i,j)*vxy+u(i,j)*vx*vy+
     &v(i,j)*uy*vx+(v(i,j)**2)*(vyy)+v(i,j)*((vy)**2))

      do l=1,101
      xt=(l-1)
      yt=(l-1)
      if (dx(i,j).gt.xt) xp(i,j)=l+1
      if (dy(i,j).gt.yt) yp(i,j)=l+1
      enddo

      enddo
      enddo

c*********************************************************
c*********************************************************
c****  Bicubic interpolation
      do t=1,ta

      do i=2,100
      do j=2,100

      d(i,j)=0
      w=0
      lp=0
      som=0
      som1=0

      if (xp(i,j).eq.101) lp=1
      if (yp(i,j).eq.101) lp=1
      if (xp(i,j).eq.2) lp=1
      if (yp(i,j).eq.2) lp=1

      do k=lp+xp(i,j)-2,xp(i,j)+1-lp
      xk=k-1
      do l=lp+yp(i,j)-2,yp(i,j)+1-lp
      yl=l-1

      somx=1
      do m=lp+xp(i,j)-2,xp(i,j)+1-lp
```

```
      xm=m-1
      if(m.ne.k) somx=((dx(i,j)-xm)/(xk-xm))*somx
      enddo

      somy=1
      do m=lp+yp(i,j)-2,yp(i,j)+1-lp
      ym=m-1
      if (m.ne.l) somy=((dy(i,j)-ym)/(yl-ym))*somy
      enddo

      w=somx*somy
      som=som+w*c(k,l)
      som1=som1+w

      enddo
      enddo

      d(i,j)=som

      enddo
      enddo

      do i=1,101
      do j=1,101
      c(i,j)=d(i,j)
      enddo
      enddo

      enddo
c*********************************************************
c**** Conservation properties
      con1=0
      con2=0
      con3=0
      cona=0
      conb=0
      conc=0

      do i=1,101
      do j=1,101
      con1=con1+c(i,j)
      con2=con2+(c(i,j))**2
      con3=con3+abs(c(i,j))
      cona=cona+b(i,j)
      conb=conb+(b(i,j))**2
      conc=conc+abs(b(i,j))
      enddo
      enddo

      con1=con1/cona
      con2=con2/conb
      con3=con3/conc
      print*, con1,con2,con3

c**********************************************************
c**********************************************************
c**** Writing out for MATLAB
      open(1,file='/frae/WEERLIG/MAT/matd36.m',form='formatted'
     &,recl=100000)
      write(1,20) c
 20   format (101f20.10)
```

```
c****  Writing statistics
      open(2,file='/frae/WEERLIG/STA/stad36')
      write(2,30) con1
      write(2,30) con2
      write(2,30) con3
 30   format (f20.10)
c*****************************************************
c****  Interactive display using PGPLOT

c****  Open plot
      IF (PGOPEN('?') .LT. 1) STOP

c****  Set contours  of streamlines to be plotted
      do i = 1,13
      ALEV(I) = -6 + (i-1)
      enddo

c****  Set contours of cone to be plotted
      KEELY(1)  = 0.02
      KEELY(2)  = 0.1
      KEELY(3)  = 0.2
      KEELY(4)  = 0.3
      KEELY(5)  = 0.4
      KEELY(6)  = 0.5
      KEELY(7)  = 0.6
      KEELY(8)  = 0.7
      KEELY(9)  = 0.8
      KEELY(10)  = 0.9

c****  Set axis
      CALL PGENV(0.,100.,0.,100.,1,1)
      TR(1)  = -1.0
      TR(2)  = 1.0
      TR(3)  = 0.0
      TR(4)  = -1.0
      TR(5)  = 0.0
      TR(6)  = 1.0

c****  Label axis, title
      CALL PGLAB('x', 'y', 'Smolarkiewicz`s Test  D3 scheme  t=T')

c****  Set colour and plot contours of streamlines
      CALL PGSCI(3)
      CALL PGCONT(tsi,101,101,1,101,1,101,ALEV,-7,TR)
      CALL PGSCI(4)
      CALL PGCONT(tsi,101,101,1,101,1,101,ALEV(8),-6,TR)

c****  Set colour and plot contours of cone
      CALL PGSCI(1)
      CALL PGCONT(b,101,101,1,101,1,101,KEELY,10,TR)

c****  Set colour and plot contours of solution
      CALL PGSCI(2)
      CALL PGCONT(c,101,101,1,101,1,101,KEELY,10,TR)

c**** CLOSE PLOT
      CALL PGCLOS

      end
```

REFERENCES

Anthes RA (1977) A cumulus parameterization scheme utilizing a one-dimensional cloud model. *Mon. Weather Rev.* **117** 1423-1438.

Anthes RA, Hsie EY and Kuo YH (1987) Description of the Penn State/NCAR Mesoscale Model Version 4 (MM4). Technical Note NCAR/TN-282+STR, National Centre for Atmospheric Research, Boulder, Colorado, 66 pp.

Anthes RA, Kuo YH, Hsie EY, Low-Nam SS and Bettge TW (1989) Estimation of episodic and climatological skill and uncertainty in regional numerical models. *Quart. J. Roy. Meteor.* **115** 770-792.

Arakawa A (1972) Design of the UCLA General Circulation Model. Numerical Simulation of Weather and Climate, Technical Report No. **7**. Department of Meteorology, University of California, Los Angeles.

Asnani GC (1993) *Tropical Meteorology* (Pune, India).

Bates JR and McDonald A (1982) Multiply-Upstream, Semi-Lagrangian Advective Schemes: Analysis and Application to a Multi-Level Primitive Equation Model. *Mon. Wea. Rev.* **110** 1831-1842.

Bates JR, Semazzi FHM, Higgins RW, Barros SRM (1990) Integration of the shallow water equations on the sphere using a vector semi-Lagrangian scheme with a multigrid solver. *Mon. Wea. Rev.* **118** 1615-1627.

Bermejo R and Staniforth A (1992) The conversion of semi-Lagrangian advection schemes to quasi-monotone schemes. *Mon. Wea. Rev.* **120** 2622-2632.

Bourke W (1974) A multi-level spectral model. I. Formulation and hemispheric integrations. *Mon. Wea. Rev.* **102** 687-701.

Carnahan B, Luther HA and Wilkes JO (1969) *Applied Numerical Methods.* Wiley, 604 pp.

Charnock H (1955) Wind stress on a water surface. *Quart. J. Roy. Meteor. Soc.* **81** 639-640.

Chouinard C, Beland M and McFarlane N (1986) A simple gravity wave drag parameterisation of use in medium-range weather forecast models. *Atmos. Ocean* **24** 91-110.

Coiffier J, Chapalet P and Marie N (1987) A study of various quasi-Lagrangian techniques for numerical models. *Proc. of ECMWF Workshop on Techniques for Horizontal Discreterization in Numerical Weather Prediction Models,* Shinfield Park, Reading, United Kingdom, European Centre for Medium-Range Weather Forecasts, 377 pp.

Corby GA, Gilchrist A and Newson RL (1972) A general circulation model of the atmosphere suitable for long period integration. *Quart. J. Roy. Meteor. Soc.* **98** 809-832.

Courtier P and Geleyn J-F (1988) A global numerical weather prediction with variable resolution: application to the shallow water equations. *Quart. J. Roy. Meteor. Soc.* **114** 1321-1346.

Crimp SJ, Lutjeharms JRE, Mason SJ (1998) Sensitivity of a tropical-temperate trough to sea-surface temperature anomalies in the Agulhas retroflection region. *Water SA.* **24** 93-100.

Crimp SJ and Mason SJ (2000) The extreme precipitation event of 11 to 16 February 1996 over South Africa. Submitted to *Meteorology and Atmospheric Physics.*

Crimp SJ, Joubert AM and Tennant W (2000) Air mass transport and associated moisture sources during cyclone Demoina, January 1984. Submitted to *Water SA.*

Crowley WP (1968) Numerical Advection Experiments. *Mon. Wea. Rev.* **96** 1-11.

Davies HC (1976) A lateral boundary formulation for multi-level prediction models. *Quart. J. Roy. Meteor. Soc.* **102** 405-418.

Deardorff JW (1977) A parameterisation of ground-surface moisture content for use in atmospheric prediction models. *J. Appl. Meteorol.* **16** 1181-1185.

Déqué M and Piedlievre J Ph (1995) High resolution climate simulations over Europe. *Climate Dyn* **11** 321-339.

Dickenson RE, Errico RM, Giorgi F and Bates GT (1989) A regional climate model for the western United States. *Clim. Change* **15** 383-422 1989.

Dorman JL and Sellers PJ (1989) A global climatology of albedo, roughness length and stomatal resistance for atmospheric general circulation models as represented by the simple biosphere model (SiB). *J. Appl. Meteorol.* **28** 833-855.

Ellis R and Gulick D (1994) *Calculus with Analytic Geometry.* Harcourt Brace College Publishers, United States of America, 1024 pp.

Engelbrecht FA and Rautenbach CJdeW (2000) Perspektief vir genestelde klimaatmodellering oor suidelike Afrika. *SA Tydskrif vir Wetenskap en Kuns* **19** 47-51.

Engelbrecht FA and Rautenbach CJdeW (2001) The contribution of extra-tropical sea-surface temperature anomalies to the 1996/97 model simulated rainfall and mean sea-level pressure over South Africa and adjacent oceans. Accepted conditionally by *Water SA*.

Errico R and Baumhefner D (1987) Predictability experiments using a high resolution limited-area model. *Mon.Wea.Rev.* **115** 408-418.

Fels SB and Schwarzkopf MD (1975) The simplified exchange approximation: a new method for radiative transfer. *J. Atmos. Sci.* **32** 1475-1488.

Fritsch JM and Chappell CF (1980) Numerical prediction of convectively driven mesoscale pressure systems, Convective parameterization. *J. Atmos. Sci.* **37** 1722-1733.

Gadd AJ (1978a) A split explicit integration scheme for numerical weather prediction. *Quart. J. Roy. Meteor. Soc.* **104** 569-582.

Gadd AJ (1978b) A numerical advection scheme with small phase speed errors. *Quart. J. Roy. Meteor. Soc.* **104** 583-594.

Garstang M, Kelbe BE, Emmitt GD and London WB (1987). Generation of convective storms over the escarpment of northeastern South Africa. *Mon. Wea. Rev.* **115** 429-443.

Giorgi F (1990) On the simulation of regional climate using a limited area model nested in a general circulation model. *J. Clim.* **3** 941-963.

Giorgi F (1991) Sensitivity of simulated summertime precipitation over the western United States to different physics parameterizations. *Mon. Wea. Rev.* **119** 2870-2888.

Giorgi F and Mearns LO (1991) Approaches to the simulation of regional climate change: A review. *Rev. Geophys.* **29** 191-216.

Giorgi F and Marinucci MR (1991) Validation of a regional atmospheric model over Europe: Sensitivity of wintertime and summertime simulation to selected physics parameterizations ans lower boundary conditions. *Quart. J. Roy. Meteor. Soc.* **117** 1171-1206.

Giorgi F, Bates GT and Nieman SJ (1993a) The multiyear surface climatology of a regional atmospheric model over the western United States. *J. Climate* **6** 75-95.

Giorgi F, Marinucci MR and Bates GT (1993b) Development of a second-generation regional climate model (RegCM2). Part I: Boundary-layer and radiative transfer processes. *Mon.Wea.Rev.* **121** 2794-2813.

Giorgi F, Marinucci MR, Bates GT and DeCanio G (1993c) Development of a second-generation regional climate model (RegCM2). Part II: Cumulus cloud and assimilation of lateral boundary conditions. *Mon.Wea.Rev.* **121** 2814-2832.

Giorgi F, Brodeur CS and Bates GT (1994) Regional climate change scenarios over the United States produced with a nested regional climate model. *J. Clim.* **7** 375-399.

Giorgi F (1995) Perspectives for regional earth system modelling. *Global and Planetary Change* **10** 23-42.

Giorgi F and Mearns LO (1999) Introduction to special section: Regional climate modeling revisited. *J. Geophys. Res.* **104** 6335-6352.

Gordon HB (1981) A flux formulation of the spectral atmospheric equations suitable for use in long-term climate modelling. *Mon. Wea. Rev.* **109** 56-64.

Gordon HB (1983) Synoptic cloud variations in a low resolution spectral atmospheric model. J. Geophys. Res. **88** 6563-6575.

Haltiner GJ and Williams RT (1980) *Numerical Prediction and Dynamic Meteorology.* 2nd ed. John Wiley & Sons, Inc., New York, 477pp.

Horel JD, Pechmann JB, Hahmann AN and Geisler JE (1994) Simulations of the Amazon Basin circulation with a regional model. *J. Climate* **7** 56-71.

Hoskins BJ and Simmons AJ (1975). A multi-layer spectral model and the semi-implicit method. *Quart. J. Roy. Meteor. Soc.* **101** 637-655.

Hostetler SW, Giorgi F, Bates GT and Bartlein PJ (1994) Lake-atmosphere feedbacks associated with paleolakes Bonneville and Lahontan. *Science* **263** 665-668.

Houghton JT, Jenkins GJ and Ephraums JJ (1990) Climate change: The IPCC Scientific Assessment. WMO/UNEP Report of Working Group I of the IPCC, Cambridge University Press 365 pp.

Jackson SP (1954) Sea breezes in South Africa. *S.A. Geogr. Jour.* **36** 13-23.

Jenkins GS and Barron EJ (1997) Global climate model and coupled regional climate model simulations over the eastern United States: GENESIS and RegCM2 simulations. *Global and Planetary Change* **15** 3-32.

Jones RG, Murphy JM and Noguer M (1995) Simulation of climate change over Europe using a nested regional climate model. I: Assessment of control climate, including sensitivity to location of lateral boundaries. *Quart. J. Roy. Meteor. Soc.* **121** 1413-1449.

Joubert AM (1997) Simulations by the Atmospheric Model Intercomparison Project of atmospheric circulation over southern Africa. *Int. J. Climatol.* **17** 1129-1154.

Joubert AM, Katzfey JJ, McGregor JL and Nguyen KC (1998) Simulating mid-summer climate over southern Africa using a nested regional climate model. Unpublished paper.

Joubert AM, Katzfey JJ, McGregor JL (1999) Daily rainfall simulations over South Africa using a nested regional climate model. Water Research Commission Report No **K5/805/0/1**, 1-86.

Juang H-M and Kanamitsu M (1994) The NMC nested regional spectral model. *Mon. Wea. Rev.* **122** 3-26.

Jury MR and Pathack B (1996) Drought over South Africa and Indian Ocean SST: Statistical and GCM results. *The Global Atmosphere and Ocean System* **4** 47-63.

Kaas E (1987) The construction of and tests with a multi-level, semi-Lagrangian and semi-implicit limited area model. Diploma thesis, Geophysics Institute, Copenhagen University 117pp.

Kalnay E and others (1996) The NCEP/NCAR 40-year reanalysis Project. *Bull Amer. Meteorol. Soc.* **77** 437-472.

Katzfey JJ (1995) Simulation of extreme New Zealand precipitation events. Part I. Sensitivity to orography and resolution. *Mon. Wea. Rev.* **123** 737-754.

Katzfey JJ (1995) Simulation of extreme New Zealand precipitation events. Part II. Mechanisms of precipitation development. *Mon. Wea. Rev.* **123** 755-775.

Keyser D and Uccellini LW (1987) Regional models: emerging research tools for synoptic meteorologists. *Bulletin of American Meteorological Society* **68** 306-320.

Kida H, Koide T, Sasaki H, and Chiba M (1991) A new approach for coupling a limited area model to a GCM for regional climate simulations. *J. Meteor. Soc. Japan* **69** 723-728

Kondo J, Saigusa N and Sato T (1990) A parameterisation of the evaporation from bare soil surfaces. *J. Appl. Meteorol.* **29** 385-389.

Kowalczyk EA, Garratt JR and Krummel PB (1994) Implementation of a soil-canopy scheme into the CSIRO GCM – regional aspects of the model response. Tech. Pap. **32** 59pp. Commonwealth Sci. and Ind. Res. Org., Melbourne.

Krishnamurti TN, Ramanathan Y, Pan H-L, Pasch RJ and Molinari J (1980) Cumulus parameterization and rainfall rates. *Mon.Wea.Rev.* **108** 465-472.

Kuo HL (1974) Further studies of the parameterization of the influence of cumulus convection on large-scale flow. *J. Atmos. Sci.* **31** 1232-1240.

Lax PD and Wendroff B (1960) Systems of conservation laws. *Comm. Pure Appl. Math* **13** 217-237.

Leonard BP, Lock AP and MacVean MK (1996) Conservative explicit unrestricted-time-step multidimensional constancy-preserving advection schemes. *Mon. Wea. Rev.* **124** 2588-2606.

Leslie LM, Mills GA, Logan LW, Kelly GAM, McGregor JL, Gauntlett DJ, Sardie JM and Manton MJ (1985) A high resolution primitive equations NWP model for operations and research. *Australian Meteorological Magazine* **33** 11-35.

Leung LR, Wigmosta MS, Ghan SJ, Epstein DJ and Vail LW (1996) Application of a subgrid orographic precipitation/surface hydrology scheme to a mountain watershed. *J. Geophys.* Res. **101** 12803-12817.

Louis JF (1979) A parametric model of vertical eddy fluxes in the atmosphere. *Bound.-Layer Meteor.*, **17** 187-202.

Lynch AH, Chapman WL, Walsh JE and Weller G (1995) Development of a regional model of the western Arctic. *J. Climate* **8** 1555-1570.

Marinucci MR, Giorgi F, Beniston M, Wild M, Tschuck P, Ohmura A and Bernasconi A (1995). High resolution simulations of January and July climate over the western Alpine region with a nested regional climate system. *Theor. Appl. Climatol.* **51** 119-138.

Mason SJ, Lindesay JA and Tyson PD (1994) Simulating drought in southern Africa using sea surface temperature variations. *Water SA* **20** 15-22.

McDonald A (1984) Accuracy of Multiply-Upstream, Semi-Lagrangian Advective Schemes. *Mon. Wea. Rev.* **112** 1267-1275.

McDonald A (1987) Accuracy of Multiply-Upstream, Semi-Lagrangian Advective Schemes II. *Mon. Wea. Rev.* **115** 1446-1450.

McDonald A and Bates JR (1987) Improving the estimate of departure position in a two time-level semi-Lagrangian semi-implicit model. *Mon.Wea.Rev.* **115** 737-739.

McDonald A and Bates JR (1989) Semi-Lagrangian integration of a gridpoint shallow water model on the sphere. *Mon. Wea. Rev.* **117** 130-137.

McGregor JL and Leslie LM (1977) On the selection of grids for semi-inplisit schemes. *Mon.Wea.Rev.* **105** 236-238.

McGregor JL, Leslie LM and Gauntlett DJ (1978) The ANMRC limited-area model: consolidated formulation and operational results. *Mon.Wea.Rev.* **106** 427-438.

McGregor JL (1987) Accuracy and initialization of a two-time-level split semi-Lagrangian model. In Short- and Medium-Range Numerical Weather Prediction, T. Matsunu (ed.). **Special Volume** of the *Journal of Meteorological Society of Japan*. 233-246.

McGregor JL and Walsh (1991) Summertime climate simulations for the Australian region using a nested model. Proc. Fifth Conf. on Climate Variations, Denmar, CO, Amer. Meteor. Soc., 515-518.

McGregor JL (1993) Economical determination of departure points for semi-Lagrangian models. *Mon.Wea.Rev.* **121** 221-230.

MCGREGOR JL and WALSH K (1993) Nested simulations of perpetual January climate over the Australian region. *J. Geophys. Res.* **98** 23283-23290.

McGregor JL, Gordon HB, Watterson IG, Dix MR and Rotstayn LD (1993a) *The CSIRO 9-level Atmospheric General Circulation Model.* CSIRO Division of Atmospheric Research Technical Paper No. **26**, Aspendale, Vic, Australia. 89pp.

McGregor JL, Walsh KJ and Katzfey JJ (1993b) Nested modelling for regional climate studies. In: Jakeman AJ Beck MB McAleer MJ (eds.) *Modelling Change in Environmental Systems.* Chichester: John Wiley, pp. 367-386.

McGregor JL and Walsh KJ (1994) Climate change simulations of Tasmanian precipitation using multiple nesting. *J. Geophys. Res.* **99** 20889-20905.

McGregor JL (1996) Semi-Lagrangian advection on conformal-cubic grids. *Mon. Wea. Rev.* **124** 1311-1322.

McGregor JL (1997a) Regional climate modelling. *Meteorol. Atmos. Phys.* **63** 105-117.

McGregor JL (1997b) Semi-Lagrangian advection on a cubic gnomic projection of the sphere. In *Numerical Methods in Atmospheric and Oceanic Modelling. The André J. Robert Memorial Volume.* C. Lin, R. Laprise and H. Ritchie, Eds. (companion volume to Atmos.-Ocean) 153-169.

McGregor JL (1999) Regional modelling at CAR: recent developments. BMRC Report No **75** 43-48.

Mesinger F and Arakawa A (1976) Numerical Methods used in Atmospheric Models. Volume 1. GARP Publications series No. 17 64 pp.

Miyakoda K, HembreeE GD, Srickler RF and Shulman I (1972) Cumulative results for extended forecast experiments. I. Model performance for winter cases. *Mon.Wea.Rev* **105** 236-238.

Morton (1971) Stability and convergence in fluid flow problems. Proc. R. Soc. **A323** 237-253.

Perkey DJ and Kreitzberg CW (1976) A time-dependant lateral boundary scheme for limited-area primitive equation models. *Mon.Wea.Rev.* **104** 744-755.

Podzun R, Cress A, Majewski D and Renner V (1995) Simulation of European Climate with a limited area model. Part II. AGCM boundary conditions. *Contrib. Atmos. Phys.* **68** 205-225.

Preston-Whyte RA (1969) Sea breeze studies in Natal. *S.A. Geogr. Jour.* **51** 38-48.

Purser RJ and Leslie LM (1988) A semi-implicsit, semi-Lagrangian finite-difference scheme using high-order spatial differencing on a non-staggered grid. *Mon.Wea.Rev* **116** 2069- 2080.

Qian J –H, Giorgil F and Fox-Rabinovitz M (1999) Regional stretched grid generation and its application to the NCAR RegCM. *J. Geophys. Res.* **104**.

Rash PJ, Boville BA and Brasseur GP (1995) A three-dimensional general circulation model with coupled chemistry for the middle atmosphere. *J. Geophys. Res.* **100** 9041-9071.

Rancic M, Purser RJ and Messinger F (1996) A global shallow-water model using an expanded spherical cube: Gnomic versus conformal coordinates. *Quart. J. Roy. Meteo. Soc.* **122** 959-982.

Rautenbach CJdeW (1999) Introduction of a hybrid vertical co-ordinate to an Atmospheric General Circulation Model. Ph.D.-thesis, University of Pretoria, 149 pp.

Rautenbach CJdeW and Engelbrecht FA (2001) Klimaatevaluasie van die CSIRO-9 Merk II (R21) globale atmosferiese algemene sirkulasie model. Accepted conditionally by *SA Tydskrif vir Wetenskap en Kuns.*

Renwick JA, Katzfey JJ, Nguyen KC and McGregor JL (1997) Regional model simulations of New Zealand climate. *J. Geophys. Res.* **103** 5973-5982.

Ritchie H (1991). Application of the semi-Lagrangian method to a multilevel spectral primitive-equations model. *Quart. J. Roy. Meteor. Soc.* **117** 91-106.

Rivest C and Staniforth A (1994) Spurious Resonant Response of Semi-Lagrangian Discreterizations to Orographic forcing: Diagnosis and Solution. *Mon. Wea. Rev.* **122** 366-376.

Robert A, Henderson J and Turnbull C (1972) An explisit time integration scheme for baroclinic models of the atmosphere. *Mon.Wea.Rev* **100** 329-335.

Robert A (1982) A semi-Lagrangian and semi-implicit numerical integration scheme for the primitive meteorological equations. *J. Meteor. Soc. Japan,* **60**, 319-325.

Rowlands IH (1998) *Climate change cooperation in Southern Africa.* Earthscan Publications Limited, London, UK 186 pp.

Sasaki H, Kida H, Koide T and Chiba M (1995) The performance of long term integrations of a limited area model with the spectral boundary coupling method. *J. Meteorol. Soc. Jpn.* **63** 165-181.

Schoenstadt AL (1980) A transfer function analysis of numerical schemes used to simulate geostophic adjustment. *Mon.Wea.Rev.* **108** 1248-1259.

Schwarzkopf MD and Fels SB (1991) The simplified exchange method revisited: an accurate, rapid method for computation of infrared cooling rates and fluxes. *J. Geophys. Res.* **96** 9075-9096.

Simmons AJ and Hoskins BJ (1978). Stability of the Semi-Implisit Method of Time Integration. *Mon. Wea. Rev.* **106** 405-412.

Smolarkiewicz PK (1982) The multidimensional Crowley advection scheme. *Mon. Wea. Rev.* **113** 1050-1065.

Staniforth A, Côté J and Pudykiewicz J (1987) Comments on Smolarkiewicz's Deformational flow. *Mon. Wea. Rev.* **115** 894-900.

Staniforth A and Côté J (1991) Semi-Lagrangian integration schemes for atmospheric models-A review. *Mon. Wea. Rev.* **106** 439-477.

Tanguay M, Yakimiw E, Ritchie H and Robert A (1992) Advantages of spatial averaging in semi-implisit semi-Lagrangian schemes. *Mon. Wea. Rev.* **120** 113-123.

Tatsumi Y (1986) A spectral limited-area model with time-dependant lateral boundary conditions and its application to a multi-level primitive equation model. *J. Meteor. Soc. Japan* **64** 637-664.

Temperton C and Staniforth A (1987) An efficient two-time-level semi-Lagrangian semi-implisit integration scheme. *Quart. J. Roy. Meteor. Soc.* **113** 1025-1039.

Thuburn J (1993) Use of a flux-limited scheme for vertical advection in a GCM. *Quart. J. Roy. Meteor. Soc.* **119** 469-487.

Tyson PD (1966) Examples of local air circulations over Cato Ridge during July 1965. *S.A. Geogr. Jour.* **48** 13.

Tyson PD (1968) Southeasterly winds over Natal. *Jour. for Geogr.* **111** 237-246.

Tyson PD (1986) Climatic Change and Variability over Southern Africa. Oxford University Press, Cape Town, 220 pp.

Van Heerden J, Rautenbach CJdeW and Truter MM (1995) Techniques for seasonal and longer term rainfall prediction in South Africa. Water Research Commission Report No **373/1/92,** 1-51.

Vinnikov K Ya and Yeserkepova IB (1991) Soil moisture: empirical data and model results. *J. Climate* **4** 66-79.

Vukicevic T and Paegle J (1989) The influence of one-way interacting lateral boundary conditions upon predictability of flow in bounded numerical models. *Mon. Wea. Rev.* **117** 340-350.

Walsh K and McGregor JL (1995) January and July Climate simulations over the Australian region using a limited area model. *J. Climate* **8** 2387-2403.

Walsh K and McGregor JL (1996) Simulations of Antartic Climate using a limited area model. *J. Geophys. Res.* **101** 19039-19108.

Walsh K and McGregor JL (1997) An assessment of simulations of climate variability over Australia with a limited area model. *Int. J. Climatol* **17** 201-223.

Welander P (1959) Studies of the general development of motion in a two-dimensional, ideal fluid. *Tellus* **7** 141-156.

Wiin-Nielsen A (1959) On the application of trajectory methods in numerical forecasting. *Tellus* **11** 180-196.